

# **Field Line Resonance in Two and a Half Dimensions**

**DRAFT VERSION CREATED ON APRIL 14, 2016**

1

© Charles A. McEachern 2016

2



3

The text of this work is licensed under a Creative Commons  
Attribution-ShareAlike 4.0 International license.

4

# <sup>5</sup> Acknowledgements

<sup>6</sup> TODO: ...

<sup>7</sup> Acknowledgement placeholder.

# <sup>8</sup> Dedication

<sup>9</sup> TODO: ...

## Abstract

11 Field line resonances — that is, Alfvén waves bouncing between the northern and south-  
12 ern foot points of a geomagnetic field line — serve to energize magnetospheric particles  
13 through drift-resonant interactions, carry energy from high to low altitude, induce cur-  
14 rents in the magnetosphere, and accelerate particles into the atmosphere. Wave struc-  
15 ture and polarization significantly impact the execution of each role. The present work  
16 showcases a new two and a half dimensional code, Tuna, ideally suited to model FLRs,  
17 with the ability to consider large-but-finite azimuthal modenumbers, coupling between  
18 the poloidal, toroidal, and compressional modes, and arbitrary harmonic structure. Us-  
19 ing Tuna, the interplay between Joule dissipation and poloidal-to-toroidal rotation is  
20 considered for both dayside and nightside conditions. An attempt is also made to de-  
21 mystify giant pulsations, a class of FLR known for its distinctive ground signatures.  
22 Numerical results are supplemented by a survey of  $\sim 800$  FLRs using data from the  
23 Van Allen Probes, the first such survey to characterize each event by both polariza-  
24 tion and harmonic. The combination of numerical and observational results suggests  
25 an explanation for the disparate distributions observed in poloidal and toroidal FLR  
26 events.

# **Contents**

<sup>27</sup>	<b>Acknowledgements</b>	i
<sup>29</sup>	<b>Dedication</b>	ii
<sup>30</sup>	<b>Abstract</b>	iii
<sup>31</sup>	<b>List of Tables</b>	vii
<sup>32</sup>	<b>List of Figures</b>	viii
<sup>33</sup>	<b>1 Introduction</b>	1
<sup>34</sup>	1.1 Structure of the Present Work . . . . .	2
<sup>35</sup>	<b>2 The Near-Earth Environment</b>	4
<sup>36</sup>	2.1 The Outer Magnetosphere . . . . .	5
<sup>37</sup>	2.2 The Inner Magnetosphere . . . . .	7
<sup>38</sup>	2.3 The Ionosphere . . . . .	8
<sup>39</sup>	2.4 Geomagnetic Storms and Substorms . . . . .	9
<sup>40</sup>	<b>3 Field Line Resonance</b>	12
<sup>41</sup>	3.1 Harmonic Structure . . . . .	16
<sup>42</sup>	3.2 Azimuthal Modenumber . . . . .	18
<sup>43</sup>	3.3 Poloidal and Toroidal Polarizations . . . . .	20
<sup>44</sup>	3.4 Giant Pulsations . . . . .	22
<sup>45</sup>	3.5 Motivations for the Present Work . . . . .	23

46	<b>4 Waves in Cold Resistive Plasma</b>	<b>25</b>
47	4.1 Guided Propagation . . . . .	27
48	4.2 Compressional Propagation . . . . .	28
49	4.3 High Altitude Limit . . . . .	30
50	4.4 Implications to the Present Work . . . . .	31
51	<b>5 “Tuna Half” Dimensional Model</b>	<b>33</b>
52	5.1 Coordinate System . . . . .	34
53	5.2 Physical Parameter Profiles . . . . .	38
54	5.3 Driving . . . . .	41
55	5.4 Maxwell’s Equations . . . . .	44
56	5.5 Boundary Conditions . . . . .	48
57	<b>6 Electron Inertial Effects</b>	<b>53</b>
58	6.1 The Boris Factor . . . . .	54
59	6.2 Parallel Currents and Electric Fields . . . . .	56
60	6.3 Inertial Length Scales . . . . .	61
61	6.4 Discussion . . . . .	63
62	<b>7 Numerical Results</b>	<b>65</b>
63	7.1 Modenumber and Compression . . . . .	65
64	7.2 Resonance and Rotation on the Dayside . . . . .	71
65	7.3 Resonance and Rotation on the Nightside . . . . .	78
66	7.4 Ground Signatures and Giant Pulsations . . . . .	83
67	7.5 Discussion . . . . .	87
68	<b>8 Van Allen Probe Observations</b>	<b>89</b>
69	8.1 Sampling Bias and Event Selection . . . . .	90
70	8.2 Events by Mode . . . . .	93
71	8.3 Events by Amplitude . . . . .	98
72	8.4 Events by Frequency . . . . .	101
73	8.5 Events by Phase . . . . .	105
74	8.6 Discussion . . . . .	110

75	<b>9 Conclusion</b>	<b>112</b>
76	9.1 Code Development . . . . .	112
77	9.2 Numerical Work . . . . .	112
78	9.3 Van Allen Probe Pc4 Survey . . . . .	112
79	<b>References</b>	<b>113</b>

# List of Tables

81	3.1 IAGA Magnetic Pulsation Frequency Bands . . . . .	14
82	5.1 Typical Parameters for the Tuna Density Profile . . . . .	39
83	5.2 Integrated Atmospheric Conductivity . . . . .	49

# <sup>84</sup> List of Figures

85	2.1	Reconnection in the Outer Magnetosphere . . . . .	5
86	2.2	Structures in the Inner Magnetosphere . . . . .	7
87	3.1	Alfvén Bounce Frequencies . . . . .	15
88	3.2	First and Second Harmonic Resonances . . . . .	17
89	3.3	Azimuthal Modenumbers Viewed from the Pole . . . . .	19
90	3.4	Poloidal Mode Structure . . . . .	21
91	3.5	Toroidal Mode Structure . . . . .	22
92	4.1	Compressional Alfvén Wave Cutoff Frequencies . . . . .	32
93	5.1	Nonorthogonal Dipole Grid . . . . .	38
94	5.2	Alfvén Speed Profiles . . . . .	40
95	5.3	Ionospheric Conductivity Profiles . . . . .	41
96	5.4	Decreasing Penetration with Increasing Modenumber . . . . .	43
97	5.5	Sym-H for June 2013 Storm . . . . .	44
98	6.1	Plasma Frequency Profile . . . . .	55
99	6.2	Electric Field Snapshots . . . . .	57
100	6.3	Current and Poynting Flux at 1000 km . . . . .	58
101	6.4	Current and Poynting Flux at 100 km . . . . .	60
102	6.5	Power Density at the Ionosphere . . . . .	61
103	6.6	Parallel Electric Fields by Perpendicular Grid Resolution . . . . .	62
104	7.1	Magnetic Field Snapshots from a Small- $m$ Run . . . . .	68
105	7.2	Magnetic Field Snapshots from a Large- $m$ Run . . . . .	69
106	7.3	Compressional Coupling to the Poloidal Mode . . . . .	70
107	7.4	Dayside Poloidal and Toroidal Energy . . . . .	75

108	7.5 Dayside Poloidal Energy Distribution . . . . .	76
109	7.6 Dayside Toroidal Energy Distribution . . . . .	77
110	7.7 Nightside Poloidal and Toroidal Energy . . . . .	80
111	7.8 Nightside Poloidal Energy Distribution . . . . .	81
112	7.9 Nightside Toroidal Energy Distribution . . . . .	82
113	7.10 Dayside Ground Magnetic Fields . . . . .	85
114	7.11 Nightside Ground Magnetic Fields . . . . .	86
115	8.1 Distribution of Usable Van Allen Probe Data . . . . .	91
116	8.2 Rate of Pc4 Events . . . . .	94
117	8.3 Rate of Pc4 Events by Mode . . . . .	95
118	8.4 Rate of Double Pc4 Events by Parity and Storm Index . . . . .	97
119	8.5 Amplitude Distribution of Pc4 Events by Mode . . . . .	99
120	8.6 Rate of Pc4 Events by Mode and Amplitude . . . . .	100
121	8.7 Rate of Pc4 Events by Mode and Frequency . . . . .	103
122	8.8 Frequency Distribution of Pc4 Events by Mode . . . . .	104
123	8.9 Waveforms and Spectra for a Pc4 Event . . . . .	107
124	8.10 Phase Distribution of Pc4 Events by Mode . . . . .	108
125	8.11 Rate of Pc4 Events by Mode and Phase . . . . .	109

<sup>126</sup> **Chapter 1**

<sup>127</sup> **Introduction**

<sup>128</sup> 1859 was a pivotal year in human history. The United States moved steadily toward  
<sup>129</sup> the American Civil War, which would abolish slavery and consolidate the power of  
<sup>130</sup> the federal government. A slew of conflicts in Southern Europe set the stage for the  
<sup>131</sup> unification of Italy. The Taiping Civil War — one of the bloodiest conflicts of all time  
<sup>132</sup> — is considered by many to mark the beginning of modern Chinese history. Origin of  
<sup>133</sup> Species was published. The first transatlantic telegraph cable was laid.

<sup>134</sup> Meanwhile, ambivalent to humanity, the Sun belched an intense burst of charged par-  
<sup>135</sup> ticles and magnetic energy directly toward Earth. The resulting geomagnetic storm<sup>1</sup>  
<sup>136</sup> caused telegraph systems to fail across the Western hemisphere, electrocuting operators  
<sup>137</sup> and starting fires[35, 94]. Displays of the northern lights were visible as far south as  
<sup>138</sup> Cuba.

<sup>139</sup> The Solar Storm of 1859 was perhaps the most powerful in recorded history, but by no  
<sup>140</sup> means was it a one-time event. The Sun discharges hundreds of coronal mass ejections  
<sup>141</sup> (CMEs) per year, of all sizes, in all directions. In fact, a comparably large CME narrowly  
<sup>142</sup> missed Earth in 2012[70]. Had it not, it's estimated it would have caused widespread,  
<sup>143</sup> long-term electrical outages, with a damage toll on the order of  $10^{12}$  dollars[66].

---

<sup>1</sup>The Solar Storm of 1859 is also called the Carrington Event, after English astronomer Richard Carrington. He drew a connection between the storm's geomagnetic activity and the sunspots he had observed the day before.

144 The Sun’s extreme — and temperamental — effect on Earth’s magnetic environment  
145 makes a compelling case for the ongoing study of space weather. Such research has  
146 evolved over the past century from sunspot counts and compass readings to multi-  
147 satellite missions and supercomputer simulations. Modern methods have dramatically  
148 increased humanity’s understanding of the relationship between the Sun and the Earth;  
149 however, significant uncertainty continues to surround geomagnetic storms, substorms,  
150 and the various energy transport mechanisms that make them up.

151 The present work focuses in particular on the phenomenon of field line resonance: Alfvén  
152 waves bouncing between the northern and southern hemispheres. Such waves play an  
153 important part in the energization of magnetospheric particles, the transport of energy  
154 from high to low altitude, the precipitation of particles into the atmosphere, and the  
155 driving of currents at the top of the atmosphere. It is these currents which give rise to  
156 potentially-catastrophic magnetic disturbances at Earth’s surface.

157 The study of resonance in the near-Earth environment is furthermore valuable as a proxy  
158 for other (less-accessible) plasma environments. Similar waves occur in astrophysical  
159 plasmas, observation of which is limited by distance. Field line resonance is also analo-  
160 gous to the so-called “fishbone instability” in fusion reactors. As a plasma laboratory,  
161 the magnetosphere is unique in that it is both close enough to measure directly, and  
162 also large enough that measurements can be performed without disrupting its behavior.

## 163 1.1 Structure of the Present Work

164 The present work is laid out as follows.

165 Chapter 2 surveys the near-Earth environment. Prominent features of the magneto-  
166 sphere are defined. The behavior of the magnetosphere during geomagnetic storms and  
167 substorms is summarized.

168 Chapter 3 introduces the field line resonance phenomenon, in terms of both the under-  
169 lying physics and notable work on the topic. Jargon is introduced to clarify important  
170 elements of wave structure. Several open questions about field line resonances (FLRs)  
171 are offered as motivations for the present work.

172 Chapter 4 lays the groundwork for a numerical model by exploring the fundamental  
173 equations of waves in a cold, resistive plasma — such as Earth’s magnetosphere. Char-  
174 acteristic scales are gleaned from the resulting dispersion relations.

175 Chapter 5 presents Tuna, a new two and a half dimensional simulation designed specif-  
176 ically for the realistic modeling of FLRs. Tuna’s non-orthogonal geometry, height-  
177 resolved ionosphere, novel driving mechanism, and coupling to the atmosphere are jus-  
178 tified and explained.

179 Chapter 6 considers the addition of electron inertial effects to Tuna, which are neglected  
180 in the core model presented in Chapter 5. These effects allow the computation of parallel  
181 currents and electric fields, which have not previously been included in global Alfvén  
182 models. The effects are shown to be instability-prone and computationally expensive,  
183 but some results are gleaned nonetheless.

184 Chapter 7 showcases the core numerical results of the present work, unifying several of  
185 the questions posed in Chapter 3. The interplay between compressional propagation,  
186 poloidal-to-toroidal rotation, and Joule dissipation is considered from several angles.

187 Chapter 8 puts the numerical results in context through the analysis of data from the  
188 Van Allen Probes mission. FLR occurrence rates are considered in terms of location,  
189 harmonic, and polarization, parameters which have been only partially addressed in  
190 past FLR surveys.

191 Chapter 9 briefly summarizes the results shown in the above chapters — code devel-  
192 opment, analysis of numerical results, and satellite observation — and suggests further  
193 directions.

<sup>194</sup> **Chapter 2**

<sup>195</sup> **The Near-Earth Environment**

<sup>196</sup> From Earth’s surface to a height of a hundred kilometers or so, the atmosphere is a  
<sup>197</sup> well-behaved fluid: a collisional ensemble of neutral atoms. Higher up, its behavior  
<sup>198</sup> changes dramatically. As altitude increases, solar ultraviolet radiation becomes more  
<sup>199</sup> intense, which ionizes atmospheric atoms and molecules. Density also decreases, slow-  
<sup>200</sup> ing collisional recombination. Whereas the neutral atmosphere is held against Earth’s  
<sup>201</sup> surface by gravity, the motion of charged particles is dominated by Earth’s geomagnetic  
<sup>202</sup> field, as well as the electromagnetic disturbances created as that field is hammered by  
<sup>203</sup> the solar wind.

<sup>204</sup> Before discussing specific interactions, it’s appropriate to introduce the so-called “frozen-  
<sup>205</sup> in condition.” In a collisionless plasma, magnetic field lines are equipotential contours.  
<sup>206</sup> Charged particles move freely along the contours, but cannot move across them. Com-  
<sup>207</sup> pression of the magnetic field is synonymous with compression of the ambient plasma,  
<sup>208</sup> as any magnetic field lines that thread a moving plasma are dragged along with it. This  
<sup>209</sup> assumption is valid throughout most of the magnetosphere — that is, the region of  
<sup>210</sup> space primarily governed by Earth’s magnetic field — and provides an invaluable tool  
<sup>211</sup> for understanding the large-scale motions of plasmas and fields.

## 2.1 The Outer Magnetosphere

Plasma behavior within Earth's magnetosphere is ultimately driven by the solar wind: a hot ( $\sim 100$  eV), fast-moving ( $\sim 100$  km/s) plasma threaded by the interplanetary magnetic field ( $\sim 10$  nT)<sup>1</sup>. The density of the solar wind is on the order of  $10^3$  /cm<sup>3</sup>; in a laboratory setting, this would constitute an ultra-high vacuum (atmospheric density at sea level is  $\sim 10^{19}$  /cm<sup>3</sup>), but compared to much of the magnetopause it's quite dense.

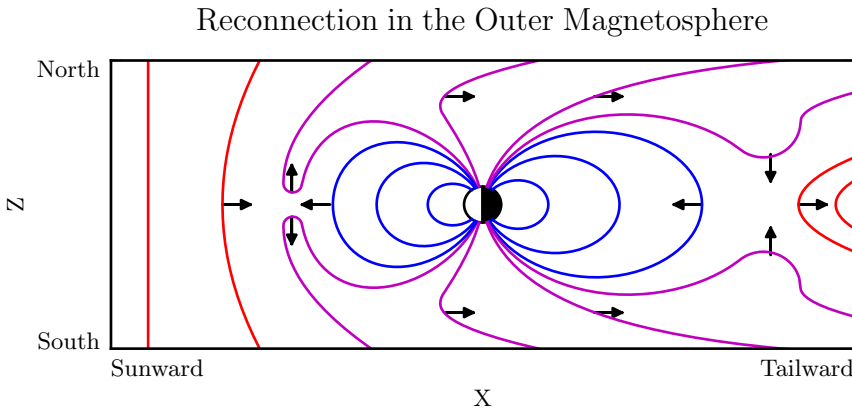


Figure 2.1: When the solar wind magnetic field (red) points southward, reconnection can occur between it and Earth's (northward) closed magnetic field lines (blue). The resulting open field lines (magenta) convect nightward over the poles, ultimately arriving in the magnetotail. There, the open field lines reconnect again. Newly closed field lines move Earthward, carrying flux across the flanks and back to the dayside. The rest are completely decoupled from Earth, and are lost to the solar wind.

The magnetosphere's outer boundary represents a balance between the solar wind dynamic pressure and the magnetic pressure of Earth's dipole field. On the dayside, the dipole is compressed, pushing this boundary to within about  $10 R_E$  of Earth<sup>2</sup>. The nightside magnetosphere is stretched into a long tail which may exceed  $50 R_E$  in width and  $100 R_E$  in length.

When the interplanetary magnetic field opposes the geomagnetic field at the nose of the magnetosphere, magnetic reconnection occurs. Closed magnetospheric field lines

<sup>1</sup>Listed values correspond to the solar wind at Earth's orbit.

<sup>2</sup>Distances in the magnetosphere are typically measured in units of Earth radii:  $1 R_E \equiv 6378$  km.

225 “break,” opening up to the interplanetary magnetic field<sup>3</sup>. They then move tailward  
226 across the poles, dragging their frozen-in plasma with them. Reconnection in the tail  
227 allows magnetic field lines to convect back to the day side, across the flanks. This  
228 process is called the Dungey cycle[21].

Viewed from the north, the Dungey cycle involves a clockwise flow of flux and plasma on  
the dusk side and a counterclockwise flow on the dawn side. The motion is accompanied  
by a convection electric field, per Ohm’s law in an ideal plasma:

$$\underline{E} + \underline{U} \times \underline{B} = 0 \quad (2.1)$$

229 Where  $\underline{B}$ ,  $\underline{E}$ , and  $\underline{U}$  are the magnetic field, electric field, and plasma velocity vectors  
230 respectively.

231 Consistent with Ampère’s law, the interplanetary magnetic field is separated from the  
232 magnetosphere by a current sheet: the magnetopause. On the dayside, the magne-  
233 topause current flows duskward; on the nightside, it flows downward around the mag-  
234 netotail.

235 Earth’s dipole is significantly deformed in the magnetotail; field lines in the northern  
236 lobe of the tail points more or less Earthward, and vice versa. Plasma within the lobes  
237 is cool ( $\sim 100$  eV) and rarefied ( $\sim 10^{-2}$  /cm<sup>3</sup>). The two lobes are divided by the plasma  
238 sheet, which is comparably hot ( $\sim 10^3$  eV) and dense ( $\sim 1$  /cm<sup>3</sup>). The plasma sheet  
239 carries a duskward current which connects to the magnetopause current.

---

<sup>3</sup>Closed field lines are more or less dipolar; one end connects to the north pole of Earth’s magnetic core, and the other end to the south pole. Open field lines are tethered to Earth at one end. In principle, the other end eventually doubles back to Earth, but for practical purposes it is lost to the solar wind. The distinction is important because charged particle motion is guided by magnetic field lines, as discussed in Chapter 3.

## 240 2.2 The Inner Magnetosphere

241 Within  $L \sim 8$  (where  $L$  is the McIlwain parameter<sup>4</sup>), the dipole magnetic field is not  
242 appreciably deformed by the solar wind. As a result, the structures in the inner mag-  
243 netosphere follow closely from the motion of charged particles in an ideal dipole field.

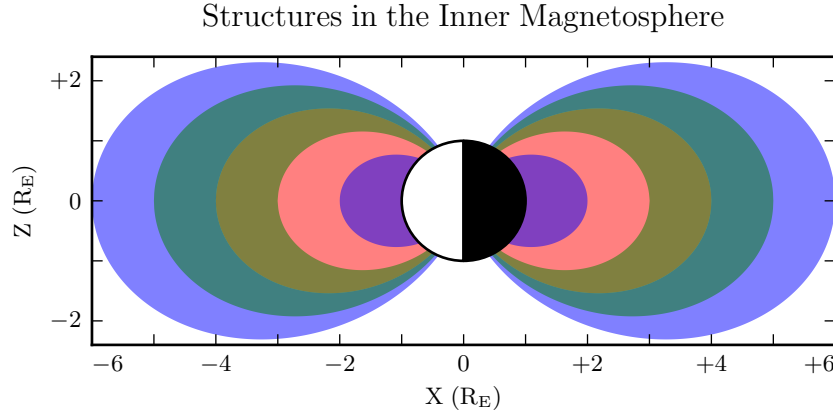


Figure 2.2: The above figure shows typical ranges in  $L$  for the plasmasphere (red,  $L < 4$ ), ring current (green,  $3 < L < 5$ ) and radiation belts (blue,  $L < 2$  and  $4 < L < 6$ ). These values, particularly the size of the plasmasphere, can vary significantly in response to geomagnetic activity.

244 The plasmasphere — a cold ( $\sim 1$  eV), dense ( $10^2 / \text{cm}^3$  to  $10^4 / \text{cm}^3$ ) torus of corotating  
245 plasma — is formed by the outward drift of atmospheric ions along magnetic closed  
246 field lines. Its outer boundary is thought to represent a balance between the corotation  
247 electric field (per the rotation of Earth's magnetic dipole) and the convection electric  
248 field (associated with the convection of magnetic flux during the Dungey cycle). Particle  
249 density drops sharply at the edge of the plasmasphere; the boundary is called the  
250 plasmapause. The plasmapause typically falls around  $L = 4$ , though during prolonged  
251 quiet times it can extend to  $L = 6$  or larger.

---

<sup>4</sup>The McIlwain parameter  $L$  is used to index field lines in Earth's dipole geometry:  $L \equiv \frac{r}{\sin^2 \theta}$  for colatitude  $\theta$  and radius  $r$  in Earth radii. For example, the  $L = 5$  field line passes through the equatorial plane at a geocentric radius of  $5 R_E$ , then meets the Earth at a colatitude of  $\arcsin \sqrt{\frac{1}{5}} \sim 27^\circ$  (equally, a latitude of  $\arccos \sqrt{\frac{1}{5}} \sim 63^\circ$ ).

252 Energetic particles trapped within the inner magnetosphere are divided into two popu-  
253 lations.

254 The Van Allen radiation belts are made up of particles with energy above  $10^5$  eV or  
255 so. The inner belt ( $L \lesssim 2$ ) is primarily composed of protons, the decay remnants of  
256 neutrons freed from the atmosphere by cosmic rays. The outer belt ( $L \gtrsim 4$ ) is primarily  
257 composed of high-energy electrons. The density of radiation belt particles is significantly  
258 affected by geomagnetic storms and substorms; a typical value is  $10 / \text{cm}^3$ .

259 Particles with energies of  $10^3$  eV to  $10^5$  eV make up the ring current, which extends  
260 from  $L \sim 3$  to  $L \sim 5$ . Gradient-curvature drift carries ions and electrons in opposite  
261 directions; the net result is a westward current. During quiet times, the ring current  
262 causes magnetic a southward magnetic field on the order of 1 nT at Earth's equator,  
263 while during geomagnetically active times (discussed in Section 2.4) the effect may be  
264 100 nT or more<sup>5</sup>.

## 265 2.3 The Ionosphere

266 Earth's neutral atmosphere is an excellent insulator. Collisions are so frequent that  
267 charged particles quickly thermalize and recombine. The breakdown of air molecules  
268 into a conductive plasma (as happens during a lightning strike, for example) requires  
269 electric fields on the order of  $10^9$  mV/m.

270 Cold particles in the magnetosphere are likewise not conducive to currents. In the  
271 absence of collisions, electrons and ions drift alongside one another in response to an  
272 electric field, creating no net current perpendicular to the magnetic field<sup>6</sup>. Magnetic  
273 field lines can typically be considered as equipotential contours, devoid of field-aligned  
274 potential structures.

275 The ionosphere is a sweet spot between the two regimes. Collisions are frequent enough  
276 to disrupt the drift of ions, but not frequent enough to immobilize the electrons. The

---

<sup>5</sup>For comparison, Earth's dipole field points north at the equator with a magnitude over  $10^4$  nT.

<sup>6</sup>The so-called  $E$ -cross- $B$  drift is associated with a velocity of  $\underline{U} = \frac{1}{B^2} \underline{E} \times \underline{B}$ , independent of a charged particle's mass or sign.

277 result is a finite-valued conductivity tensor. Pedersen currents (which scale with the  
278 Pedersen conductivity) flow in the direction of the perpendicular electric field. Hall  
279 currents (due to the Hall conductivity) flow in the  $\underline{B} \times \underline{E}$ . It is these currents — par-  
280 ticularly the Hall current — which give rise to magnetic fields at the ground. Collisions  
281 in the ionosphere also result in a finite parallel conductivity, allowing for the formation  
282 of potential structures along the magnetic field line.

283 The convection electric field (associated with the Dungey cycle, Section 2.1) drives  
284 Pedersen currents in the ionosphere. Pedersen currents flow downward on the flanks  
285 and duskward across the poles. The currents remain divergence-free by connecting  
286 to field-aligned currents at the edges of the polar cap. The field-aligned currents, in  
287 turn, connect to the magnetopause current, the cross-tail current, and the (partial) ring  
288 current.

289 When electron density is low, thermal velocities may be unable to carry enough current  
290 to satisfy  $\nabla \cdot \underline{J} = 0$ . This leads to the formation of potential structures along geomagnetic  
291 field lines in the ionosphere. Such structures accelerate particles along magnetic field  
292 lines, leading to the precipitation of energetic particles into the atmosphere. As the  
293 particles thermalize, they excite atmospheric atoms. The resulting spontaneous emission  
294 is often in the visible spectrum, giving rise to the aurora.

## 295 2.4 Geomagnetic Storms and Substorms

296 The quiet geomagnetic behavior described above is periodically disturbed by transient  
297 solar phenomena such as corotating interaction regions (CIRs) and coronal mass ejec-  
298 tions (CMEs). CMEs, such as the one that caused the Solar Storm of 1859 mentioned  
299 in Chapter 1, are bursts of unusually dense solar wind which are ejected from regions of  
300 high magnetic activity on the Sun; they are most common at the height of the eleven-  
301 year solar cycle. CIRs, on the other hand, occur when a relatively fast region of the  
302 solar wind catches up to an earlier and slower-moving pocket of solar wind, resulting in  
303 a pair of shockwaves.

304 During a storm, increased solar wind intensity results in enhanced magnetic reconnection  
305 on the dayside. As the newly-opened field lines are swept tailward, the convection  
306 electric field is strengthened. The plasmasphere — the outer boundary of which is set by  
307 a balance between the convection electric field and the (more or less constant) corotation  
308 electric field — sheds its outer layers[33]. A large number of energetic particles are also  
309 injected into the ring current[67].

310 The strength of the storm is gauged by the size of the magnetic perturbation created  
311 by the ring current<sup>7</sup>. A small storm has a magnitude of 50 nT to 100 nT. Large storms  
312 may reach 250 nT to 500 nT. The Carrington Event, mentioned in Chapter 1, is thought  
313 to have exceeded 1700 nT[94].

314 The main phase of a storm typically lasts for several hours. Storm recovery — the  
315 gradual return of the storm index to zero, and the refilling of the plasmasphere — lasts  
316 several days. Geomagnetic storms occur tens of times per year at the height of the solar  
317 cycle, and just a few times per year otherwise.

318 Whereas storms are prompted by large solar wind events on the dayside, geomagnetic  
319 substorms are primarily a nightside occurrence. As flux accumulates in the tail, mag-  
320 netic tension builds in the stretched field lines. A substorm is an impulsive release of  
321 that tension.

322 At substorm onset, a burst of reconnection occurs in the tail. A jet of plasma is launched  
323 Earthward from the reconnection site (and another is launched tailward, and lost to the  
324 solar wind). The Earthward plasma injection injects particles into the ring current.  
325 The outer radiation belt is depleted, then repopulated. Energetic particles precipitate  
326 into the atmosphere, giving rise to a distinctive sequence of auroral signatures over the  
327 course of about an hour.

328 Concurrent with substorm onset, impulsive Alfvén waves are observed with periods of  
329 a minute or two. The precise ordering of events — whether reconnection causes the  
330 waves, or vice versa, or if they share a common cause — remains controversial.

---

<sup>7</sup>The most commonly used storm index is DST, which is computed hourly using measurements from several ground magnetometers near the equator. The Sym-H index, used in Section 5.3, is computed once per minute.

- 331 Each substorm lasts several hours, including the time it takes for the ring current to  
332 return to pre-substorm levels. Several substorms may occur per day during quiet times.  
333 During a storm, substorms become far more frequent; by the time one has ended,  
334 another may have already begun.

<sup>335</sup> **Chapter 3**

<sup>336</sup> **Field Line Resonance**

<sup>337</sup> The motion of a charged particle in a dipole field can be described in terms of three  
<sup>338</sup> fundamental motions.

<sup>339</sup> The first is cyclotron motion. Given a uniform magnetic field line, a particle follows a  
<sup>340</sup> helical path. It moves in a circular path in a plane normal to the magnetic field line,  
<sup>341</sup> and keeps a constant velocity along the direction of the field. Close to Earth, where the  
<sup>342</sup> magnetic field is strongest, the proton (electron) cyclotron timescale is on the order of  
<sup>343</sup>  $10^{-3}$  s ( $10^{-6}$  s); at  $L \sim 5$ , a typical value is closer to 10 s ( $10^4$  s).

<sup>344</sup> The second fundamental motion is bounce motion. As it moves along the magnetic field  
<sup>345</sup> line like a bead on a wire, the particle experiences a change in magnetic field magnitude.

<sup>346</sup> In order to conserve its magnetic moment (also called the first adiabatic invariant), the  
<sup>347</sup> particle's perpendicular kinetic energy increases in proportion with the magnetic field.

<sup>348</sup> When the perpendicular kinetic energy can no longer increase — that is, when all of  
<sup>349</sup> the particle's kinetic energy is perpendicular — the particle bounces back. Particles  
<sup>350</sup> undergoing bounce motion continuously move back and forth between the northern and  
<sup>351</sup> southern hemispheres, with timescales of a few seconds to a few minutes.

<sup>352</sup> Particles with more parallel kinetic energy (compared to their perpendicular kinetic  
<sup>353</sup> energy) bounce at lower altitudes. If the particle's motion is sufficiently field-aligned, the

354 bounce altitude drops into the atmosphere, and the particle is collisionally thermalized.

355 This process is called precipitation.

356 The third fundamental motion is drift motion. Over the course of a particle's cyclotron  
357 motion, the Earthward half of the orbit experiences a slightly stronger magnetic field  
358 (and thus a slightly smaller orbit radius). The net effect, called the gradient-curvature  
359 drift, is an azimuthal motion around Earth on timescales of  $\sim 10^3$  s.

360 Wave-particle resonance arises when a particle's periodic motion matches with the fre-  
361 quency of a coincident electromagnetic wave[23, 63, 72, 83]. In the particle's rest frame,  
362 the wave then appears as a net electric field. This allows a net movement of energy  
363 between the wave and the particle. The interaction is analogous to a surfer moving  
364 along with — and being accelerated by — a wave in the ocean. Such resonance can  
365 arise for any of the three fundamental motions, or even for a combination of them.

366 In the present work, the waves under consideration are field line resonances (FLRs). An  
367 FLR is a standing harmonic on a geomagnetic field line. It can also be envisioned as  
368 a superposition of traveling waves, reflecting back and forth between its northern and  
369 southern foot points at the conducting ionosphere.

These waves travel at the Alfvén speed,  $v_A$ , defined per

$$v_A^2 \equiv \frac{B^2}{\mu_0 \rho} \quad \text{or, equally,} \quad v_A^2 \equiv \frac{1}{\mu_0 \epsilon_{\perp}} \quad (3.1)$$

370 Where  $B$  is the magnetic field magnitude,  $\rho$  is the mass density, and  $\mu_0$  is the magnetic  
371 constant. The perpendicular electric constant  $\epsilon_{\perp}$  is analogous to the electric constant  
372  $\epsilon_0$ , and arises in cases (such as the magnetosphere) where a dielectric medium exhibits  
373 a preferred direction. In the magnetosphere, mass density and magnetic field strength  
374 depend strongly on position. As a result, the Alfvén speed varies by several orders  
375 of magnitude over the length of a field line. The fundamental equations of field line  
376 resonance were presented by Dungey in 1954[20]. Since then, they have remained a  
377 topic of active study.

378 So-called ultra low frequency waves — of which FLRs are a subset — are categorized  
 379 by morphology. Continuous (long-lived) pulsations are termed Pc, while irregular pulsations  
 380 are called Pi. Within each are a number of frequency bands; see Table 3.1[44].  
 381 In practice, frequency demarcations are not strict, but rather serve as a heuristic for  
 382 grouping phenomenologically similar waves[41].

Table 3.1: IAGA Magnetic Pulsation Frequency Bands

	Pc1	Pc2	Pc3	Pc4	Pc5	Pi1	Pi2
Period (s)	0.2–5	5–10	10–45	45–150	150–600	1–40	40–150
Frequency (mHz)	200–5000	100–200	22–100	7–22	2–7	25–1000	7–25

383 FLRs fall into the Pc3, Pc4, and Pc5 ranges. The present work focuses specifically  
 384 on the Pc4 band: waves with periods of a minute or two. Frequencies in the Pc4  
 385 range typically coincide with Alfvén bounce times<sup>1</sup> near the plasmapause:  $L \sim 4$  to  
 386  $L \sim 6$ [2, 16, 24, 56]<sup>2</sup>. In fact, the large radial gradients in the Alfvén speed near the  
 387 plasmapause act as an effective potential well, trapping FLRs[15, 49, 53, 54, 62, 86].

388 In addition to being radially localized, FLRs in the Pc4 frequency band (also called Pc4  
 389 pulsations, or just Pc4s) are localized in magnetic local time (MLT<sup>3</sup>). They have also  
 390 been shown to occur preferentially on the dayside, during storms or storm recovery[2,  
 391 16, 24, 52, 56, 95].

392 In the inner magnetosphere, the Alfvén frequency — and thus the frequency of FLRs  
 393 — often coincides with integer or half-integer<sup>4</sup> multiples of particle drift frequencies[17].  
 394 The resulting wave-particle interactions can give rise to significant energization and ra-  
 395 dial diffusion of the particles. In some cases, the waves also include an electric field  
 396 parallel to the background magnetic field, breaking the assumption that magnetic field

<sup>1</sup>The Alfvén frequency is the inverse of the Alfvén bounce time:  $\frac{2\pi}{\omega_A} \equiv \oint \frac{dz}{v_A}$ .

<sup>2</sup>Not coincidentally, these are the same  $L$ -shells where the Van Allen Probes spend most of their time; see Chapter 8.

<sup>3</sup>Noon points toward the Sun and midnight away from it, with 06:00 and 18:00 at the respective dawn and dusk flanks.

<sup>4</sup>See Section 3.1.

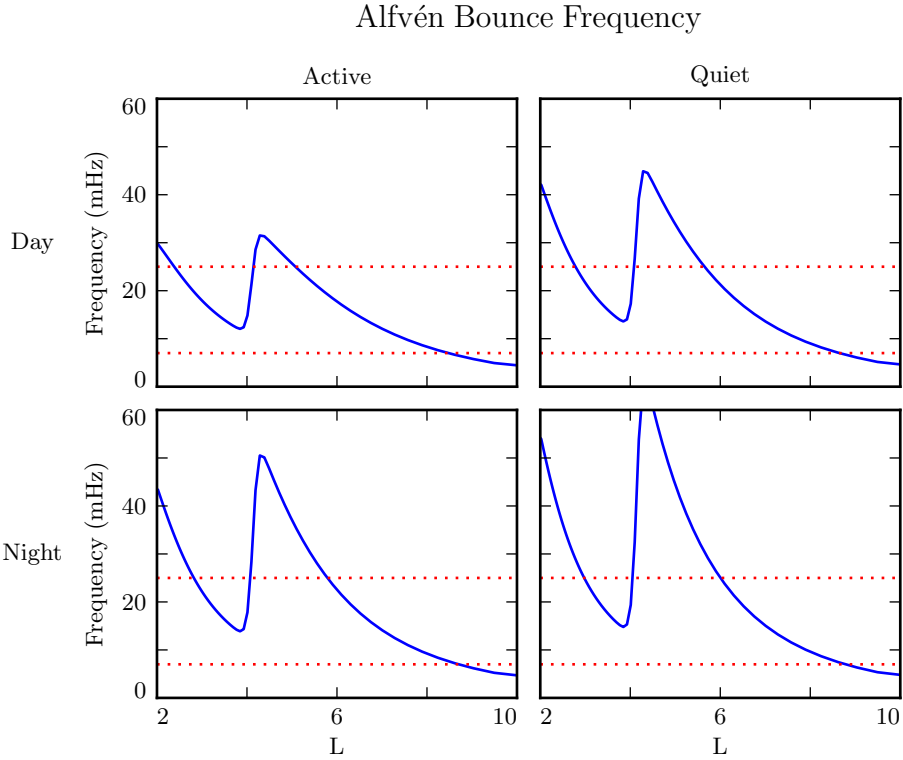


Figure 3.1: The above are bounce frequencies for an Alfvén wave moving back and forth along a geomagnetic field line. Alfvén speeds are computed based on profiles from Kelley[47], as discussed in Section 5.2. Notably, the bounce frequency depends significantly on the position of the plasmasphere, taken here to be at  $L = 4$ . Dotted lines indicate the P<sub>c4</sub> frequency range: 7 mHz to 25 mHz.

397 lines are equipotential contours, and contributing to the precipitation of energetic par-  
 398 ticles into the neutral atmosphere[31, 32, 92, 101].

399 The present chapter introduces the structural characteristics of FLRs, how those charac-  
 400 teristics affect wave behavior, and several unresolved questions related to that behavior.

401 **3.1 Harmonic Structure**

402 Wave structure along a geomagnetic field line is indicated by harmonic number. The  
403 first (or fundamental) harmonic has a wavelength twice as long as the field line. The  
404 electric field perturbation is zero at the ionospheric foot points of the field line, due to  
405 the conductivity of the ionosphere. For the first harmonic, this puts an electric field  
406 antinode at the equator, along with a node in the perpendicular<sup>5</sup> perturbation to the  
407 magnetic field. For the second harmonic, the electric field has a third node at the  
408 equator, in addition to the two at the ionospheric foot points, which is accompanied by  
409 an antinode in the perpendicular wave magnetic field. Figure 3.2 shows a qualitative  
410 sketch of the first and second harmonics: a series of snapshots in time, in the rest frame  
411 of the wave. Perpendicular electric and magnetic field perturbations are shown in blue  
412 and red respectively.

413 A first-harmonic FLR that is periodic or localized in the azimuthal direction is conducive  
414 to drift-resonant wave-particle interactions[17, 73]. The particle is like a child on a swing:  
415 whenever the path of the particle (or child) gets close to the wave (parent), it gets a  
416 push, and always in the same direction. The wave fields spend half its time pointing  
417 the other direction, just as the parent must shift their weight backward to get ready for  
418 the next push, but at that point the particle (child) is far away.

419 Second-harmonic FLRs interact with particles through the drift-bounce resonance, which  
420 is slightly more complicated. As the particle drifts azimuthally, it also zig-zags north-  
421 south. The combination of those two periodic motions must align with the phase of  
422 the wave electric field. An example path is shown by the purple line in Figure 3.2:  
423 the particle's drift and bounce motions together ensure that it experiences a rightward  
424 electric field throughout the wave's oscillation.

The drift and drift-bounce resonance conditions is written, respectively[87]:

$$\omega - m\omega_D = 0 \quad \text{and} \quad \omega - m\omega_D = \omega_B \quad (3.2)$$

---

<sup>5</sup>The parallel, or compressional, wave magnetic field exhibits the same nodes and antinodes as the perpendicular electric field[76].

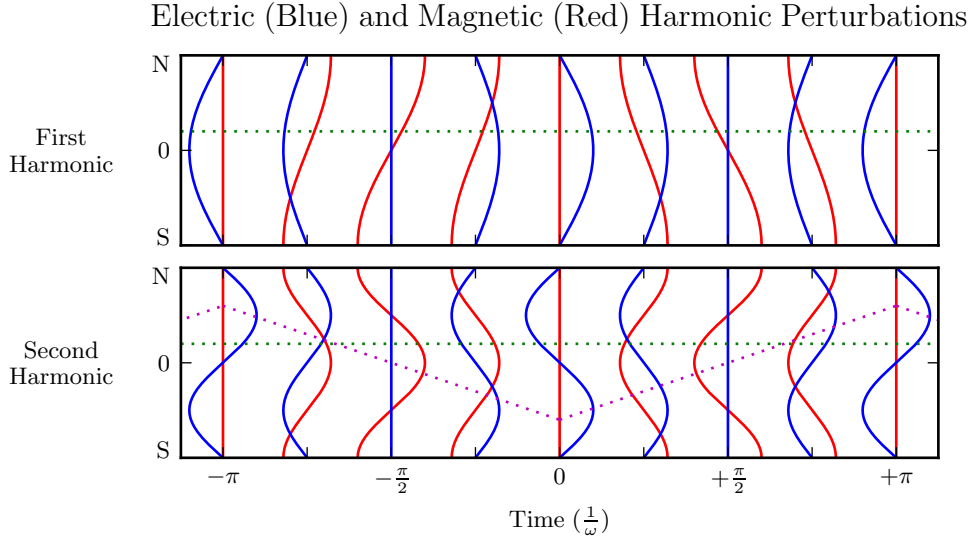


Figure 3.2: The first (or fundamental) harmonic has an antinode in its perpendicular electric field (blue) at the equator, along with a node in its perpendicular magnetic field perturbation (red). A single satellite can identify the first harmonic by the relative phase of the electric and magnetic field perturbations: an observer north of the equator (green) will see the magnetic field perturbation lead the electric field by  $\pm 90^\circ$ . The second harmonic is the opposite: it has an electric field node at the equator, and an observer north of the equator will see the magnetic field perturbation lag the electric field by  $\mp 90^\circ$ . Top and bottom signs correspond to the poloidal (shown) and toroidal polarizations respectively. The purple line sketches the path of a particle in drift-bounce resonance; in the particle’s rest frame, the electric field is always to the right.

- 425    Where  $\omega$  is the frequency of the wave,  $\omega_D$  and  $\omega_B$  are the particle’s drift and bounce
- 426    frequencies respectively, and  $m$  is the wave’s azimuthal modenumber, as discussed in
- 427    Section 3.2.
- 428    In principle, the first and second harmonics can be distinguished by their frequencies,
- 429    even from a single-point observation[2, 14, 34]. In practice, however, this is not a reliable
- 430    approach[88]. Significant uncertainties surround the mass density profile — and thus
- 431    the Alfvén speed profile — along a geomagnetic field line.
- 432    Harmonic structure can also be deduced by noting the phase offset between the wave
- 433    magnetic field and its electric field (or the plasma velocity)[16, 91]. In Figure 3.2, the
- 434    green line indicates an observer just north of the magnetic equator. For a wave polarized

435 in the poloidal direction (see Section 3.3), the observer sees the electric field waveform  
436 offset from the magnetic field by a phase of  $\pm 90^\circ$ , where the top sign is for odd modes  
437 and the bottom sign is for even modes. The signs are flipped for toroidally-polarized  
438 waves, and again for waves observed south of the equator.

439 In addition to a wave’s parity, the phase indicates how energy is divided between stand-  
440 ing and traveling waves. Standing waves (phase of  $\pm 90^\circ$ ) have a purely imaginary  
441 Poynting flux. Traveling waves (phase of  $0^\circ$  or  $180^\circ$ ), on the other hand, have real  
442 Poynting flux, indicating a net movement of energy. Wave lifetimes can be estimated  
443 by comparing the energy density to the rate at which that energy is carried away by  
444 Poynting flux, as is done in Chapter 8.

445 Notably, the measurement of wave phase has only become viable with the advent of  
446 satellites carrying both electric and magnetic field instrumentation, such as THEMIS in  
447 2007[3] and the Van Allen Probes (formerly RBSP, for Radiation Belt Storm Probes)  
448 in 2012[84].

449 Strictly speaking, the the phase offset of the electric and magnetic fields does not provide  
450 the harmonic number — only its parity. It’s reasonably safe to assume that an even mode  
451 is the second harmonic; the second harmonic is by far the most commonly observed[43,  
452 81, 89], due in part to its excitement by the antisymmetric balloon instability[9, 11,  
453 12, 83]. However, the distinction between the first and third harmonics is not always  
454 clear[13, 34]; this issue is discussed further in Chapter 8. Higher harmonics than that  
455 are not expected in the Pc4 frequency band.

## 456 3.2 Azimuthal Modenumber

457 The wavelength of an FLR in the azimuthal direction is indicated by its azimuthal  
458 modenumber. A wave with modenumber  $m$  has an azimuthal wavelength that spans  $\frac{24}{m}$   
459 hours in MLT.

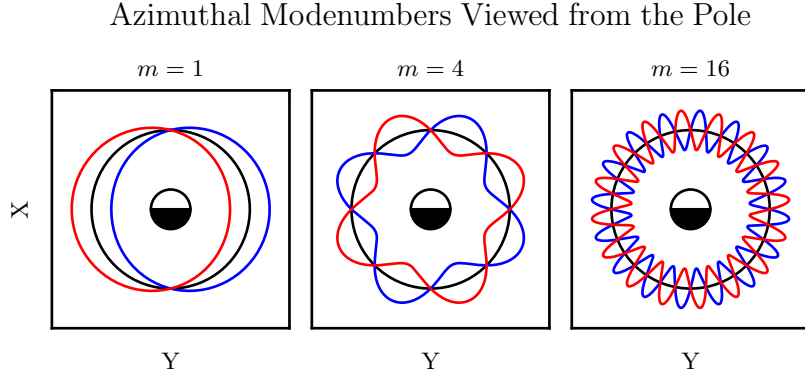


Figure 3.3: Above are qualitative sketches of waves with azimuthal modenumbers 1, 4, and 16, projected into the ecliptic plane. Black circles show unperturbed fields, while the blue and red curves show perturbations. At  $m = 1$ , the wave is more or less a uniform displacement, while at  $m = 16$  azimuthal variations take place on spatial scales small compared to Earth's radius.

- 460 Waves with small azimuthal modenumbers ( $0 < m < 10$ ) are typically driven by broad-
- 461 band energy sources at the magnetosphere's boundary, such as variations in the so-
- 462 lar wind pressure[18, 38, 48, 104, 105], sporadic magnetic reconnection[41], or Kelvin-
- 463 Helmholtz waves on the magnetopause[10, 57, 82]. In the low- $m$  regime, the shear and
- 464 compressional Alfvén waves are coupled, which allows energy to move across field lines
- 465 until the driving frequency lines up with the local Alfvén frequency[59]. Because of their
- 466 broadband energy source, low- $m$  FLRs often have a mishmash of frequencies present in
- 467 their spectra[16], though the spectra are coherent in terms of harmonic[25].
  
- 468 When the azimuthal modenumber is large (or, equally, when the azimuthal wavelength
- 469 is small), compressional propagation of Alfvén waves becomes evanescent, so the move-
- 470 ment of energy is guided by magnetic field lines[14, 76]<sup>6</sup>. As a result, FLRs must be
- 471 driven from within the magnetosphere. Proposed energy sources include phase space
- 472 gradients near the plasmapause[17], particularly as the plasmasphere refills after a storm
- 473 or substorm[24, 55].

---

<sup>6</sup>Equally, the strength of a wave's parallel component indicates its modenumber, a point which is revisited in Chapters 7 and 8.

474 The atmosphere is known to attenuate waves with small spatial extent in the perpendicular  
475 direction[42, 99, 103]. As a result, FLRs may create no signature on the ground if  
476 their azimuthal modenumber is large. For example, a recent paper by Takahashi shows  
477 a strong (2 nT at  $L \sim 10$ ), clear resonance with  $|m| \gtrsim 70$  and no corresponding ground  
478 signature[88].

Southwood[83] and Glassmeier[29] show that a low frequency wave passing through the ionosphere on its way to Earth will be attenuated per

$$\frac{B_E}{B_I} = \frac{\Sigma_H}{\Sigma_P} \exp\left(-m \frac{R_I - R_E}{R_E \sin \theta}\right) \quad (3.3)$$

479 Where  $B_E$  and  $B_I$  are the magnetic field strengths at  $R_E$  (Earth's surface, 6783 km  
480 geocentric) and  $R_I$  (the ionosphere,  $\sim$ 6900 km geocentric) respectively. The integrated  
481 ionospheric Pedersen and Hall conductivities,  $\Sigma_P$  and  $\Sigma_H$ , are typically within a factor  
482 of two of one another. Field lines near the plasmapause can be traced to Earth at  
483  $\sin \theta \sim 0.4$ . That is, by the time it reaches the ground, the magnetic field from an FLR  
484 with  $m = 10$  is weaker by a factor of two; at  $m = 100$ , the factor is closer to 100.

### 485 3.3 Poloidal and Toroidal Polarizations

486 Based on polarization, each FLR can be classified as either poloidal or toroidal. The  
487 poloidal mode is a field line displacement in the meridional plane, as shown in Figure 3.4,  
488 with an accompanying electric field in the azimuthal direction. The toroidal mode's  
489 magnetic displacement is azimuthal, per Figure 3.5; the associated electric field is in the  
490 meridional plane.

491 Both poloidal and toroidal waves are noted for their ability to contribute to the energiza-  
492 tion and radial diffusion of trapped particles. The poloidal mode interacts more strongly,  
493 since its electric field is aligned with the trapped particles' drift motion. Poloidally-  
494 polarized waves are also more prone to creating magnetic signatures on the ground, due  
495 to ducting in the ionosphere[27, 36].

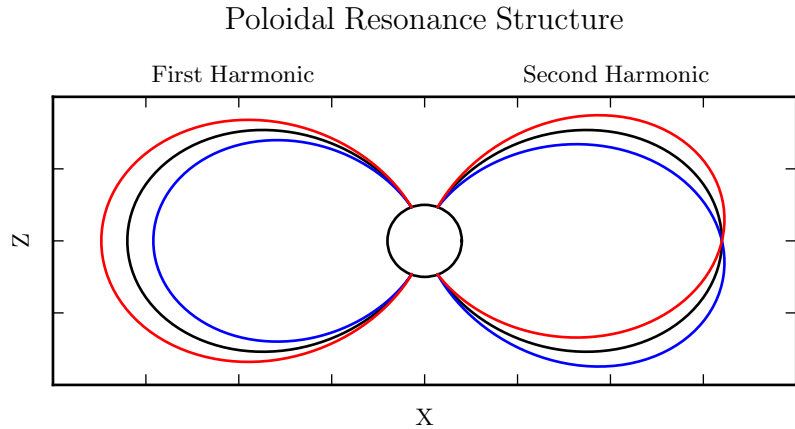


Figure 3.4: The poloidal resonance is a magnetic field in the meridional plane. The displacement is radial near the equator, and can be accompanied by enhancement in the parallel magnetic field near the ionosphere. The first harmonic is shown on the left, and the second harmonic on the right. Lines are colored red and blue only to contrast with the unperturbed black field line.

- 496 Toroidal modes have been shown to outnumber poloidal modes[2]. Perhaps not co-  
 497 incidentally, poloidally-polarized waves rotate asymptotically to the toroidal mode[64,  
 498 65, 76]. Poloidal waves with low azimuthal modenumber — such as those driven by  
 499 broadband sources at the magnetopause — rotate on timescales comparable to their  
 500 oscillation periods. The two modes are also coupled directly by the ionospheric Hall  
 501 conductivity[46].
- 502 The eigenfrequencies for poloidal and toroidal FLRs are similar, though not identical[34].  
 503 It has furthermore been noted that toroidally-polarized waves exhibit a strong relation-  
 504 ship between frequency and  $L$ -shell (or latitude), while poloidal waves at fixed frequency  
 505 are spread more broadly in  $L$ [25].

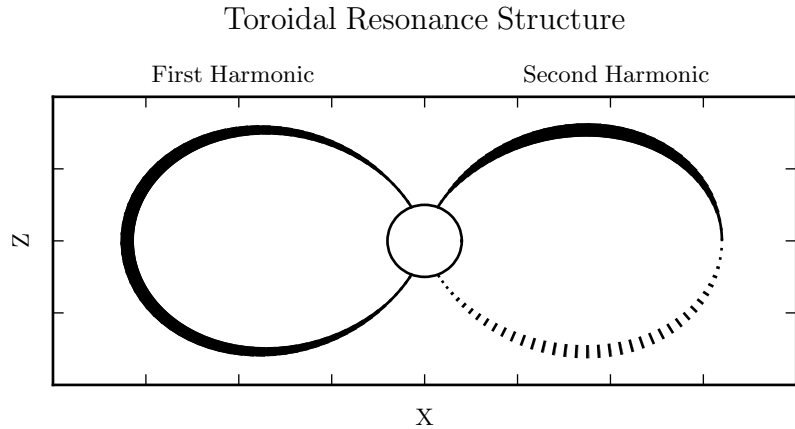


Figure 3.5: A toroidally-polarized FLR has a magnetic perturbation in the azimuthal direction, as shown. Bold lines are taken to be above the page, and dotted lines below the page, with the displacement indicated by the line’s width. The first harmonic — where the entire field line oscillates in and out of the page — is shown on the left. The second harmonic is on the right, with northern and southern halves perturbed in opposite directions.

### 506 3.4 Giant Pulsations

507 The study of geomagnetic pulsations long predates satellites, sounding rockets, or even  
508 the word “magnetohydrodynamics”<sup>7</sup>. Large, regular oscillations in the magnetic field  
509 were noted as early as 1901[5]. Eventually, the term “giant pulsation,” or Pg, arose to  
510 describe such pulsations.

511 On the ground, Pgs are notable for their strikingly sinusoidal waveforms, their eastward  
512 drifts, and their specific occurrence pattern: Pgs are typically seen pre-dawn, at latitudes  
513 of 60° to 70°. Pgs generally fall into the Pc4 frequency band<sup>8</sup>. Their harmonic structure  
514 was a source of controversy for decades, but recent multisatellite observations seem to be  
515 in agreement that they are odd harmonics, probably fundamental[30, 40, 51, 52, 87, 91].  
516 They are poloidally polarized, with modenumbers  $10 \lesssim m \lesssim 40$ [28, 40, 73, 79, 91].

---

<sup>7</sup>The term was first used by Alfvén in the 1940s[1].

<sup>8</sup>The Pc4 range is periods of 45 s to 140 s, while Pgs range from 60 s to 200 s[7].

517 Whereas FLRs are waves in space which may produce ground signatures, “giant pulsation” refers to the ground signature specifically<sup>9</sup>. That is, Takahashi’s satellite observation of a sinusoidal, morningside, high- $m$ , fundamental poloidal resonance was not  
518  
519  
520 classified as a Pg because it did not produce a signal on the ground[88].

521 Due to their remarkably clear waveforms, Pgs are typically found by “visual inspection  
522 of magnetometer data”[68]. Over the course of the past century, a number of multi-year  
523 (sometimes multi-decade[7]) surveys have totaled nearly one thousand Pg events. On  
524 average, a ground magnetometer near 66° magnetic latitude observes  $\sim$ 10 Pg events per  
525 year[7, 39, 78, 85]. Observations are not distributed uniformly; rather, giant pulsations  
526 are most common near the equinox and during times of low solar activity.

527 Unlike Pc4 pulsations in general, Pgs show no particular correlation with storm phase[68].  
528 However, they do often occur as the magnetosphere recovers from a substom[68, 79].

### 529 3.5 Motivations for the Present Work

530 A great deal has been learned — and continues to be learned — through observations of  
531 field line resonance. However, the cost-to-benefit ratio is climbing. As summarized in the  
532 sections above, FLR behavior depends significantly on harmonic structure, azimuthal  
533 modenumber, and polarization — not to mention frequency, spectral width, and so  
534 on. With each degree of freedom comes the necessity for an additional simultaneous  
535 observation.

536 Similarly, as FLRs have been shown to depend on ever-more-specific magnetospheric  
537 conditions, analytical techniques have fallen out of favor. The height-resolved iono-  
538 sphere, multidimensional Alfvén speed profile, and inconvenient geometry combine to  
539 create a problem beyond the reasonable purview of pencil and paper.

540 That is, the topic of field line resonance is ripe for numerical modeling.

---

<sup>9</sup>Historically, the wave designations shown in Table 3.1 all referred to ground phenomena. Over time, they have come to describe satellite observations as well, including those without corresponding signatures on the ground.

541 Past models of the magnetosphere have been limited in their consideration of FLRs.  
542 Reasons include overly-simplified treatment of the ionospheric boundary, no consider-  
543 ation of the plasmapause, limited range in  $m$ , and the inability to compute ground  
544 signatures. Chapter 5 presents a model which addresses these issues, allowing the com-  
545 putation of field line resonance with unparalleled attention to realism.

546 The model allows a bird’s-eye view of the structure and evolution of FLRs. As such,  
547 not only can several open questions be addressed, but their answers serve to unify a  
548 number of seemingly-disparate properties described in the sections above.

549 The rotation of poloidally-polarized waves to the toroidal mode is investigated. Par-  
550 ticular attention is paid to the importance of azimuthal modenumber and ionospheric  
551 conductivity. The interplay between said rotation and the transport of energy across  
552 field lines — which also depends on azimuthal modenumber — is considered as well.

553 By their nature, drifting particles have the potential to spur wave-particle interactions  
554 at all MLT. However, Pc4 observations are strongly peaked on the dayside. In a 2015  
555 paper, Dai notes, “It is not clear why noncompressional [high- $m$ ] Pc4 poloidal waves,  
556 which are presumably driven by instability within the magnetosphere, preferentially  
557 occur on the dayside”[16]. Motoba, later that year, echoes, “It is unclear whether other  
558 generation mechanisms of fundamental standing waves ... can explain the localization  
559 of Pgs in local time”[68]. This, too, is considered numerically: to what degree is field  
560 line resonance affected by the (day-night asymmetric) conditions of the ionosphere?

561 An attempt is also made to demystify giant pulsations. It’s been shown that toroidal  
562 Pc4s outnumber poloidal ones, and that most poloidal Pc4s are even, so perhaps it  
563 should come as no surprise that (poloidal, odd) Pgs are rare. Is it truly the case that  
564 Pgs are only “a small subset of fundamental poloidal waves”[88], set apart from the rest  
565 by their distinctive properties? Or, said another way, to what degree do the properties  
566 associated with Pgs arise in fundamental poloidal waves overall?

<sup>567</sup> **Chapter 4**

<sup>568</sup> **Waves in Cold Resistive Plasma**

<sup>569</sup> Before delving into the implementation of the numerical model, it's instructive to consider the fundamental equations of waves in a cold, resistive plasma. Specifically, the present chapter is concerned with waves much slower than the electron cyclotron frequency. High-frequency waves such as the L and R modes are beyond the scope of the present work — and, in fact, beyond the limits of the model described in Chapter 5.

The evolution of electric and magnetic fields is governed by Ampère's law and Faraday's law. Notably, the present work takes the linearized versions of Maxwell's equations; the vectors  $\underline{E}$  and  $\underline{B}$  indicate perturbations above the zeroth-order magnetic field.

$$\underline{\epsilon} \cdot \frac{\partial}{\partial t} \underline{E} = \frac{1}{\mu_0} \nabla \times \underline{B} - \underline{J} \quad \frac{\partial}{\partial t} \underline{B} = -\nabla \times \underline{E} \quad (4.1)$$

Current follows Ohm's law. For currents perpendicular to the background magnetic field, Kirchhoff's formulation is sufficient. Conductivity is much higher along the magnetic field lines<sup>1</sup>, so it's appropriate to also include the electron inertial term<sup>2</sup>.

$$0 = \underline{\sigma}_{\perp} \cdot \underline{E}_{\perp} - \underline{J}_{\perp} \quad \frac{1}{\nu} \frac{\partial}{\partial t} J_z = \sigma_0 E_z - J_z \quad (4.2)$$

---

<sup>1</sup>The dipole coordinate system is defined rigorously in Section 5.1; at present, it's sufficient to take  $\hat{z}$  parallel to the zeroth-order magnetic field, and  $\hat{x}$  and  $\hat{y}$  perpendicular to  $\hat{z}$  (and to each other).

<sup>2</sup>Electron inertial effects are not included in the model described in Chapter 5, or in the results in Chapter 7; however, their implementation and impact are explored in Chapter 6.

Derivatives in Equations (4.1) and (4.2) can be evaluated by performing a Fourier transform. They can then be combined, eliminating the magnetic field and current terms.

$$\begin{aligned} 0 &= \underline{\underline{E}}_{\perp} + \frac{v_A^2}{\omega^2} (\underline{k} \times \underline{k} \times \underline{E})_{\perp} + \frac{i}{\epsilon_{\perp}\omega} \underline{\sigma}_{\perp} \cdot \underline{\underline{E}}_{\perp} \\ 0 &= E_z + \frac{c^2}{\omega^2} (\underline{k} \times \underline{k} \times \underline{E})_z + \frac{i\omega_P^2}{\omega(\nu - i\omega)} E_z \end{aligned} \quad (4.3)$$

The speed of light, Alfvén speed (including the displacement current correction), plasma frequency, and parallel conductivity are defined in the usual way:

$$c^2 \equiv \frac{1}{\mu_0\epsilon_0} \quad v_A^2 \equiv \frac{1}{\mu_0\epsilon_{\perp}} \quad \omega_P^2 \equiv \frac{ne^2}{m_e\epsilon_0} \quad \sigma_0 \equiv \frac{ne^2}{m_e\nu} \quad (4.4)$$

Where the perpendicular dielectric constant  $\epsilon_{\perp}$  is analogous to the electric constant  $\epsilon_0$ , but for electric fields which are perpendicular to the preferred direction of the dielectric medium. As noted in Equation (3.1),  $\epsilon_{\perp} \equiv \frac{\rho}{B^2}$  where  $\rho$  is the mass density and  $B$  is the magnitude of the (zeroth-order) magnetic field.

Using the vector identity  $\underline{k} \times \underline{k} \times \underline{E} = \underline{k} \underline{k} \cdot \underline{E} - k^2 \underline{E}$ , Equation (4.3) can be reassembled into a single expression,

$$0 = \left( \underline{\underline{\mathbb{I}}} + \frac{1}{\omega^2} \underline{\underline{V}}^2 \cdot \underline{k} \underline{k} - \frac{k^2}{\omega^2} \underline{\underline{V}}^2 + \frac{i}{\omega} \underline{\underline{\Omega}} \right) \cdot \underline{E} \quad (4.5)$$

Where  $\underline{\underline{\mathbb{I}}}$  is the identity tensor and in  $x$ - $y$ - $z$  coordinates,

$$\underline{\underline{V}}^2 \equiv \begin{bmatrix} v_A^2 & 0 & 0 \\ 0 & v_A^2 & 0 \\ 0 & 0 & c^2 \end{bmatrix} \quad \text{and} \quad \underline{\underline{\Omega}} \equiv \begin{bmatrix} \frac{\sigma_P}{\epsilon_{\perp}} & \frac{-\sigma_H}{\epsilon_{\perp}} & 0 \\ \frac{\sigma_H}{\epsilon_{\perp}} & \frac{\sigma_P}{\epsilon_{\perp}} & 0 \\ 0 & 0 & \frac{\omega_P^2}{(\nu - i\omega)} \end{bmatrix} \quad (4.6)$$

The parenthetical expression in Equation (4.5) is the dispersion tensor. Nontrivial solutions exist only when its determinant is zero. This gives rise to a seventh-order polynomial in  $\omega$ , so rather than a direct solution it's necessary to consider limits of specific interest.

582 In these limits, as explored in the sections below, the wave vector  $\underline{k}$  is taken — without  
 583 loss of generality — to lie in the  $x$ - $z$  plane (that is,  $k_y$  is taken to be zero). The distinction  
 584 between the two perpendicular components ( $k_x$  and  $k_y$ ) is discussed in Section 4.4.

585 **4.1 Guided Propagation**

586 The wave vector of a field line resonance aligns closely to the background magnetic  
 587 field. By supposing that the two align exactly (that is, taking  $k_x = 0$ ), the parallel and  
 588 perpendicular components of the dispersion relation are decoupled.

The parallel-polarized component ( $E_x = E_y = 0$ ) is quadratic, and thus can be solved directly.

$$0 = \omega^2 + i\nu\omega - \omega_P^2 \quad \text{so} \quad \omega = -\frac{i\nu}{2} \pm \sqrt{\omega_P^2 - \frac{\nu^2}{4}} \quad (4.7)$$

It bears noting that the plasma frequency is large — not just compared to Pc4 frequencies, but even compared to the collision frequencies in the ionosphere<sup>3</sup>. Expanding Equation (4.7) with respect to large  $\omega_P$ , the dispersion relation becomes

$$\omega^2 = \omega_P^2 \pm i\nu\omega_P + \dots \quad (4.8)$$

589 Equation (4.8) can hardly be called a wave, as it does not depend on the wave vector  
 590  $\underline{k}$ . Rather, it is the plasma oscillation<sup>4</sup>: electrons vibrating in response to a charge  
 591 separation along the background magnetic field.

592 The plasma oscillation is not specifically relevant to the study of field line resonance.  
 593 The two phenomena are separated by six orders of magnitude in frequency. The topic  
 594 is revisited in Chapter 6 insomuch as it is inseparable from the electron inertial effects  
 595 in Ohm’s law, but it is otherwise not relevant to the work at hand.

---

<sup>3</sup>The collision frequency may match or exceed the plasma frequency for a thin slice at the bottom of the ionosphere, where the density of neutral atoms is large; however, it falls off quickly. Above an altitude of 200 km, conservatively[71], the plasma frequency exceeds the collision frequency by an order of magnitude or more.

<sup>4</sup>The plasma oscillation is also called the Langmuir wave.

The perpendicular ( $E_z = 0$ ) components of the dispersion relation give an expression quartic in  $\omega$ .

$$0 = \omega^4 + 2i\frac{\sigma_P}{\epsilon_\perp}\omega^3 - \left(2k_z^2v_A^2 + \frac{\sigma_P^2 + \sigma_H^2}{\epsilon_\perp^2}\right)\omega^2 - 2ik_z^2v_A^2\frac{\sigma_P}{\epsilon_\perp}\omega + k_z^4v_A^4 \quad (4.9)$$

Like the parallel-polarized component above, Equation (4.9) can be solved directly. Noting that  $\pm$  and  $\oplus$  are independent,

$$\omega = \left(\frac{\pm\sigma_H - i\sigma_P}{2\epsilon_\perp}\right) \oplus \sqrt{k_z^2v_A^2 + \left(\frac{\pm\sigma_H - i\sigma_P}{2\epsilon_\perp}\right)^2} \quad (4.10)$$

Also like the parallel-polarized component, the exact solution is less useful than its Taylor expansion. The Pedersen and Hall conductivities are large near the ionospheric boundary, but fall off quickly; for the vast majority of the field line, the ratios  $\frac{\sigma_P}{\epsilon_\perp}$  and  $\frac{\sigma_H}{\epsilon_\perp}$  are small compared to field line resonance frequencies. Expanding with respect to small conductivity gives

$$\omega^2 = k_z^2v_A^2 \oplus k_zv_A\frac{\sigma_H \pm i\sigma_P}{\epsilon_\perp} + \dots \quad (4.11)$$

596 This is the shear Alfvén wave, with a shift in its frequency proportional to the character-  
 597 istic conductivity of the ionosphere<sup>5</sup>. The wave travels along the background magnetic  
 598 field like a bead on a string, with electric and magnetic field perturbations perpendicular  
 599 to the magnetic field line (and to one another).

## 600 4.2 Compressional Propagation

601 The partner to guided motion is compressional motion; in order for energy to move  
 602 across field lines, the wave vector must have a component perpendicular to  $\hat{z}$ . If the

---

<sup>5</sup>Admittedly, it's difficult to say what constitutes a characteristic conductivity. The Pedersen and Hall conductivities vary by several orders of magnitude within the ionosphere, then drop essentially to zero at large radial distance.

603 wave vector is completely perpendicular to the magnetic field line ( $k_z = 0$ ), the parallel  
 604 and perpendicular components of the dispersion relation decouple, as in Section 4.1.

The parallel-polarized ( $E_x = E_y = 0$ ) component of the dispersion relation is

$$0 = \omega^3 + i\nu\omega^2 - (k_x^2 c^2 + \omega_P^2) \omega - ik_x^2 c^2 \nu \quad (4.12)$$

Equation (4.12) can be solved directly, though its solution (as a cubic) is far too long to be useful. Expanding with respect to the large plasma frequency, gives

$$\omega^2 = k^2 c^2 + \omega_P^2 - i\nu\omega_P + \dots \quad (4.13)$$

605 This is the O mode, a compressional wave with an electric field perturbation along  
 606 the background magnetic field. Like the plasma oscillation discussed in Section 4.1, its  
 607 frequency is very large compared to that of a field line resonance, putting it beyond the  
 608 concern of the present work.

The perpendicular-polarized ( $E_z = 0$ ) component of the compressional dispersion relation is also cubic.

$$0 = \omega^3 + 2i\frac{\sigma_P}{\epsilon_\perp}\omega^2 - \left(2k_x^2 v_A^2 + \frac{\sigma_P^2 + \sigma_H^2}{\epsilon_\perp^2}\right) \omega - ik_x^2 v_A^2 \frac{\sigma_P}{\epsilon_\perp} \quad (4.14)$$

A wave moving across magnetic field lines near the ionospheric boundary will encounter large  $\frac{\sigma_P}{\epsilon_\perp}$  and  $\frac{\sigma_H}{\epsilon_\perp}$ , while at moderate to high altitudes those ratios will be small. Solving Equation (4.14) in those two limits respectively gives:

$$\omega^2 = k_x^2 v_A^2 \pm ik_x v_A \frac{\sigma_P}{\epsilon_\perp} + \dots \quad \text{and} \quad \omega^2 = k_x^2 v_A^2 + \left(\frac{\sigma_H \pm i\sigma_P}{\epsilon_\perp}\right)^2 + \dots \quad (4.15)$$

609 At first glance, both limits of Equation (4.15) appear to describe compressional Alfvén  
 610 waves. The magnetic perturbation is along the background magnetic field — indicating  
 611 compression of the frozen-in plasma — while the electric field perturbation is perpen-  
 612 dicular to both the magnetic field and the wave vector.

613 However, in the high-conductivity limit, the parenthetical term actually dominates the  
 614 Alfvén term, taking values as large as  $\sim 10^6$  Hz. Waves at such frequencies are beyond  
 615 the scope of the present work. As a matter of interest, however, it bears noting that —  
 616 as long as  $\nu \ll 10^6$  Hz —  $\frac{\sigma_H}{\epsilon_{\perp}}$  reduces to the electron cyclotron frequency,  $\frac{eB}{m_e}$ .

### 617 4.3 High Altitude Limit

618 In the limit of large radial distance, it's reasonable to take the collision frequency to  
 619 zero; doing so also neglects the Pedersen and Hall conductivities.

Whereas in Sections 4.1 and 4.2 it was the parallel-polarized component of the dispersion relation that factored out from the other two, the high altitude limit decouples the component polarized out of the  $x$ - $z$  plane. The  $y$ -polarized ( $E_x = E_z = 0$ ) dispersion relation is simply:

$$\omega^2 = k^2 v_A^2 \quad (4.16)$$

620 Equation (4.16) describes an Alfvén wave with an arbitrary angle of propagation. De-  
 621 pending on the angle between the wave vector and the background magnetic field, it  
 622 could be guided, compressional, or somewhere in between. Regardless of propagation  
 623 angle, the electric field perturbation is perpendicular to both the direction of propaga-  
 624 tion and the magnetic field perturbation.

The other two components (from  $E_y = 0$ ) of the high altitude dispersion tensor give an expression quadratic in  $\omega^2$ :

$$0 = \omega^4 - (k_x^2 c^2 + k_z^2 v_A^2 + \omega_P^2) \omega^2 + k_z^2 v_A^2 \omega_P^2 \quad (4.17)$$

Which can be solved for

$$\omega^2 = \frac{1}{2} (k_x^2 c^2 + k_z^2 v_A^2 + \omega_P^2) \pm \sqrt{\frac{1}{4} (k_x^2 c^2 + k_z^2 v_A^2 + \omega_P^2)^2 - k_z^2 v_A^2 \omega_P^2} \quad (4.18)$$

Noting again that  $\omega_P$  is very large, the two roots can be expanded to

$$\omega^2 = k_z^2 v_A^2 \left( 1 - \frac{k_x^2 c^2 + k_z^2 v_A^2}{\omega_P^2} \right) + \dots \quad \text{and} \quad \omega^2 = k_x^2 c^2 + k_z^2 v_A^2 + \omega_P^2 + \dots \quad (4.19)$$

- 625 The first solution of Equation (4.19) is a shear Alfvén wave, as in Equation (4.11).  
 626 Notably, this form arises only when the parenthetical quantity is close to unity — as it  
 627 is for FLRs. The inertial limit, where frequencies are close to the plasma frequency, is  
 628 beyond the scope of the present work. For that same reason, the second solution (which  
 629 describes an oscillation faster than the plasma frequency) is not further considered.

#### 630 4.4 Implications to the Present Work

- 631 The present section’s findings carry three implications of particular significance to the  
 632 present work.  
 633 First — with the exception of the plasma oscillation and similar modes, which are  
 634 revisited in Chapter 6 — waves propagate at the Alfvén speed. This, in combination  
 635 with the grid configuration, constrains the time step that can be used to model them  
 636 numerically. The time step must be sufficiently small that information traveling at the  
 637 Alfvén speed cannot “skip over” entire grid cells<sup>6</sup>.

Second, the results of the present section allow an estimate of the magnitude of parallel electric field that might be expected from a field line resonance compared to its perpendicular electric field. Between the full dispersion tensor form in Equation (4.5) and the Alfvén wave described by Equation (4.19),

$$\left| \frac{E_z}{E_x} \right| = \frac{k_x k_z c^2}{\omega^2 - k_x^2 c^2 - \omega_P^2} \sim \frac{k^2 c^2}{\omega_P^2} \quad (4.20)$$

- 638 In essence, the relative magnitudes of the parallel and perpendicular electric fields should  
 639 scale quadratically with the ratio of the electron inertial length ( $\frac{c}{\omega_P} \sim 1 \text{ km to } 100 \text{ km}$ )

---

<sup>6</sup>As is the convention, the time step is scaled down from the smallest Alfvén zone crossing time by a Courant factor, typically 0.1, meaning that it takes at least ten time steps to cross a grid cell.

and the FLR wavelength ( $\frac{1}{k} \sim 10^5$  km). That is, parallel electric fields should be smaller than perpendicular ones by at least six orders of magnitude.

Finally, the dispersion relations shown above indicate how the behavior of a field line resonance should behave as the azimuthal modenumber becomes large.

Whereas the shear Alfvén wave's dispersion relation depends only on the parallel component of the wave vector, the compressional Alfvén wave depends on its magnitude:  $\omega^2 = k^2 v_A^2$ . If the frequency is smaller than  $k v_A$ , the wave will become evanescent. The wave vector's magnitude can be no smaller than its smallest component, however, and the azimuthal component scales with the azimuthal modenumber:  $k_y \sim \frac{m}{2\pi r}$ .

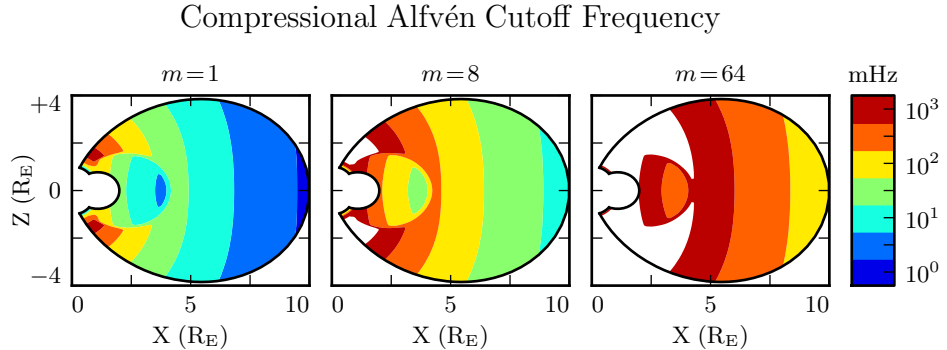


Figure 4.1: Taking  $k_y \sim \frac{m}{2\pi r}$  as a lower bound for the magnitude of the wave vector, the above figure demonstrates the lowest frequency at which compressional Alfvén waves may propagate as a function of position and  $m$ . Regions shown in white are off the color scale — they have a lower bound on the order of  $10^4$  mHz or more. The above Alfvén frequency profile is from Kelley[47], for quiet dayside conditions, as discussed in Section 5.2.

This imposes a frequency cutoff on compressional Alfvén waves which scales with the azimuthal modenumber, as shown in Figure 4.1. At small values of  $m$ , most of the magnetosphere is conducive to compressional Alfvén waves in the Pc4 frequency range. As  $m$  increases, and the wave vector with it, the inner magnetosphere becomes increasingly inaccessible to them.

654 **Chapter 5**

655 **“Tuna Half” Dimensional Model**

656 The present section describes the implementation of Tuna, a new two and a half dimensional  
657 Alfvén wave code based largely on work by Lysak[58, 61].

658 The half-integer dimensionality refers to the fact that Tuna’s spatial grid resolves a  
659 two-dimensional slice of the magnetosphere, but that electric and magnetic fields —  
660 as well as their curls — are three-dimensional vectors. This apparent contradiction is  
661 reconciled by the use of a fixed azimuthal modenumber,  $m$ . Electric and magnetic fields  
662 are taken to be complex-valued, varying azimuthally per  $\exp(im\phi)$ ; derivatives with  
663 respect to  $\phi$  are then replaced by a factor of  $im$ .

664 Unlike a fully three-dimensional code, Tuna cannot resolve the evolution of wave structures  
665 in the azimuthal direction. Furthermore, the model does not allow coupling between  
666 the dayside and nightside magnetospheres. What Tuna does offer is efficiency.  
667 The model’s economical geometry allows it to include a realistic Earthward boundary:  
668 grid spacing on the order of 10 km, a height-resolved ionospheric conductivity tensor,  
669 and even the computation of magnetic field signatures at the ground. Such features  
670 would pose a prohibitive computational expense in a large global code.

671 Tuna was developed with field line resonance in mind. As discussed in Chapter 3,  
672 such waves are azimuthally localized, minimizing the importance of Tuna’s missing half  
673 dimension. Moreover, because field line resonances are known to be affected by both

674 the ionosphere and the plasmasphere, a faithful treatment of the inner magnetosphere  
675 is a crucial part of studying them numerically.

676 Perhaps the most exciting feature of Tuna is its novel driving mechanism: ring current  
677 perturbation. Codes similar to Tuna have traditionally been driven using compressional  
678 pulses at the outer boundary[58, 61, 97, 98]. This has precluded the investigation of  
679 waves with large azimuthal modenumber — such as giant pulsations — which are guided,  
680 and thus must be driven from within the magnetosphere.

681 Tuna’s source code, written in Fortran, is publicly available at <https://github.com/UMM-Space-Physics>. The repository also includes a pair of Python scripts: a test har-  
682 ness — which automates programming environment setup, compilation, and interfacing  
683 with the supercomputer queue — and a plotter.

684 **TODO:** Set up Git repo.

## 686 5.1 Coordinate System

Field line resonance has traditionally been modeled by straightening the field lines into a rectangular configuration[20, 64], by unrolling the azimuthal coordinate into a cylindrical coordinate system[76], or through the use of dipole coordinates[75]<sup>1</sup>:

$$x \equiv -\frac{\sin^2 \theta}{r} \quad y \equiv \phi \quad z \equiv \frac{\cos \theta}{r^2} \quad (5.1)$$

687 Where  $r$ ,  $\theta$ , and  $\phi$  take on their usual spherical meanings of radial distance, colatitude,  
688 and azimuthal angle respectively.

689 The dipole coordinate  $x$  is constant over each  $L$ -shell<sup>2</sup>,  $y$  is azimuthal angle, and  $z$   
690 indexes each field line from south to north. The unit vectors  $\hat{x}$ ,  $\hat{y}$ , and  $\hat{z}$  point in  
691 the crosswise<sup>3</sup> (radially outward at the equator), azimuthal (eastward), and parallel  
692 (northward at the equator) directions respectively.

---

<sup>1</sup>The dipole coordinates  $x$ ,  $y$ , and  $z$  are sometimes named  $\mu$ ,  $\phi$ , and  $\nu$  respectively.

<sup>2</sup>In fact,  $x$  is inversely proportional to  $L$ .

<sup>3</sup>In the context of in situ measurements taken near the equatorial plane,  $\hat{x}$  is referred to as the radial direction; however, the present work extends the dipole grid to low altitudes, where  $\hat{x}$  is often more

Notably, the dipole coordinates in Equation (5.1) are normal to one another. While mathematically convenient, they do not readily accommodate a fixed-altitude boundary at the ionosphere, nor do they allow the dipole magnetic field to intersect the boundary at an oblique angle, as Earth's field does. As a solution, a nonorthogonal set of dipole coordinates was developed numerically by Proehl[74], then formalized analytically by Lysak[58] in terms of their contravariant components:

$$u^1 = -\frac{R_I}{r} \sin^2 \theta \quad u^2 = \phi \quad u^3 = \frac{R_I^2}{r^2} \frac{\cos \theta}{\cos \theta_0} \quad (5.2)$$

693 Above,  $R_I$  is the position of the ionosphere relative to Earth's center; it's typically taken  
694 to be  $1 R_E + 100 \text{ km}$ .

695 Like the dipole coordinates  $x$ ,  $y$ , and  $z$ , Lysak's coordinates  $u^1$ ,  $u^2$ , and  $u^3$  correspond to  
696  $L$ -shell, azimuthal angle, and position along a field line respectively. However, compared  
697 to  $z$ ,  $u^3$  has been renormalized using the invariant colatitude<sup>4</sup>  $\theta_0$ . As a result,  $u^3$  takes  
698 the value  $+1$  at the northern ionospheric boundary and  $-1$  at the southern ionospheric  
699 boundary for all field lines.

Because Lysak's coordinate system is not orthogonal — that is, because curves of constant  $u^1$  and curves of constant  $u^3$  can intersect at non-right angles — it's necessary to consider covariant and contravariant basis vectors separately.

$$\hat{e}_i \equiv \frac{\partial}{\partial u^i} \underline{x} \quad \hat{e}^i \equiv \frac{\partial}{\partial \underline{x}} u^i \quad (5.3)$$

Covariant basis vectors  $\hat{e}_i$  are normal to the curve defined by constant  $u^i$ , while contravariant basis vectors  $\hat{e}^i$  are tangent to the coordinate curve (equivalently,  $\hat{e}^i$  is normal to the plane defined by constant  $u^j$  for all  $j \neq i$ ). These vectors are reciprocal to one

---

horizontal than vertical. The term “crosswise” is meant to indicate that  $\hat{x}$  is defined by the cross product of  $\hat{y}$  and  $\hat{z}$ .

<sup>4</sup>The invariant colatitude is the colatitude  $\theta$  at which a field line intersects the ionosphere. It is related to the McIlwain parameter by  $\cos \theta_0 \equiv \sqrt{1 - \frac{R_I}{L}}$ .

another, and can be combined to give components of the metric tensor  $\underline{\underline{g}}$ [19].

$$\hat{e}^i \cdot \hat{e}_j = \delta_j^i \quad g_{ij} \equiv \hat{e}_i \cdot \hat{e}_j \quad g^{ij} \equiv \hat{e}^i \cdot \hat{e}^j \quad (5.4)$$

700 The symbol  $\delta_j^i$  is the Kronecker delta; the present work also makes use of the Levi-Civita  
701 symbol  $\varepsilon^{ijk}$  and Einstein's convention of implied summation over repeated indeces[22].

The metric tensor allows rotation between covariant and contravariant representations of vectors.

$$A_i = g_{ij} A^j \quad \text{and} \quad A^i = g^{ij} A_j \quad \text{where} \quad A_i \equiv \underline{A} \cdot \hat{e}_i \quad \text{and} \quad A^i \equiv \underline{A} \cdot \hat{e}^i \quad (5.5)$$

In addition, the determinant of the metric tensor is used to define cross products and curls<sup>5</sup>.

$$(\underline{A} \times \underline{B})^i = \frac{\varepsilon^{ijk}}{\sqrt{g}} A_j B_k \quad \text{and} \quad (\nabla \times \underline{A})^i = \frac{\varepsilon^{ijk}}{\sqrt{g}} \frac{\partial}{\partial u^j} A_k \quad \text{where} \quad g \equiv \det \underline{\underline{g}} \quad (5.6)$$

Explicit forms of the basis vectors and metric tensor can be found in the appendix of Lysak's 2004 paper[58]. At present, it's sufficient to note the mapping between Lysak's basis vectors and the usual dipole unit vectors.

$$\hat{x} = \frac{1}{\sqrt{g^{11}}} \hat{e}^1 \quad \hat{y} = \frac{1}{\sqrt{g^{22}}} \hat{e}^2 \quad \hat{z} = \frac{1}{\sqrt{g^{33}}} \hat{e}_3 \quad (5.7)$$

The basis vectors can also be mapped to the spherical unit vectors, though Equation (5.8) is valid only at the ionospheric boundary.

$$\hat{\theta} = \frac{1}{\sqrt{g_{11}}} \hat{e}_1 \quad \hat{\phi} = \frac{1}{\sqrt{g_{22}}} \hat{e}_2 \quad \hat{r} = \frac{1}{\sqrt{g_{33}}} \hat{e}^3 \quad (5.8)$$

702 The coordinates converge at the equatorial ionosphere, so an inner boundary is necessary  
703 to maintain finite grid spacing. It's typically placed at  $L = 2$ . The outer boundary is

---

<sup>5</sup>The square root of the determinant of the metric tensor is called the Jacobian. It's sometimes denoted using the letter  $J$ , which is reserved for current in the present work.

704 at  $L = 10$ . The dipole approximation of Earth’s magnetic field is tenuous at the outer  
705 boundary; however, in practice, wave activity is localized inside  $L \sim 7$ . The grid is  
706 spaced uniformly in  $u^1$ , which gives finer resolution close to Earth and coarser resolution  
707 at large distances.

708 Spacing in  $u^3$  is set by placing grid points along the outermost field line. The points are  
709 closest together at the ionosphere, and grow towards the equator. The spacing increases  
710 in a geometric fashion, typically by 3%.

711 Typically, Tuna uses a grid 150 points in  $u^1$  by 350 points in  $u^3$ . The result is a resolution  
712 on the order of 10 km at the ionosphere, which increases to the order of  $10^3$  km at the  
713 midpoint of the outermost field line.

714 There are no grid points in  $u^2$  due to the two-and-a-half-dimensional nature of the  
715 model. Fields are assumed to vary as  $\exp(imu^2)$  — equally,  $\exp(im\phi)$  — so derivatives  
716 with respect to  $u^2$  are equivalent to a factor of  $im$ . In effect, the real component of  
717 each field is azimuthally in phase with the (purely real) driving, while imaginary values  
718 represent behavior that is azimuthally offset. Azimuthal modenumbers span the range  
719  $1 \lesssim m \lesssim 100$ , consistent with observations of Pc4 and Pg events[16, 17, 68, 88].

720 The simulation’s time step is set based on the grid spacing. As is the convention,  $\delta t$  is  
721 set to match the smallest Alfvén zone crossing time, scaled down by a Courant factor  
722 (typically 0.1). It bears noting that the smallest crossing time need not correspond to  
723 the smallest zone; the Alfvén speed peaks several thousand kilometers above Earth’s  
724 surface, in the ionospheric Alfvén resonator[61]. A typical time step is on the order of  
725  $10^{-5}$  s.

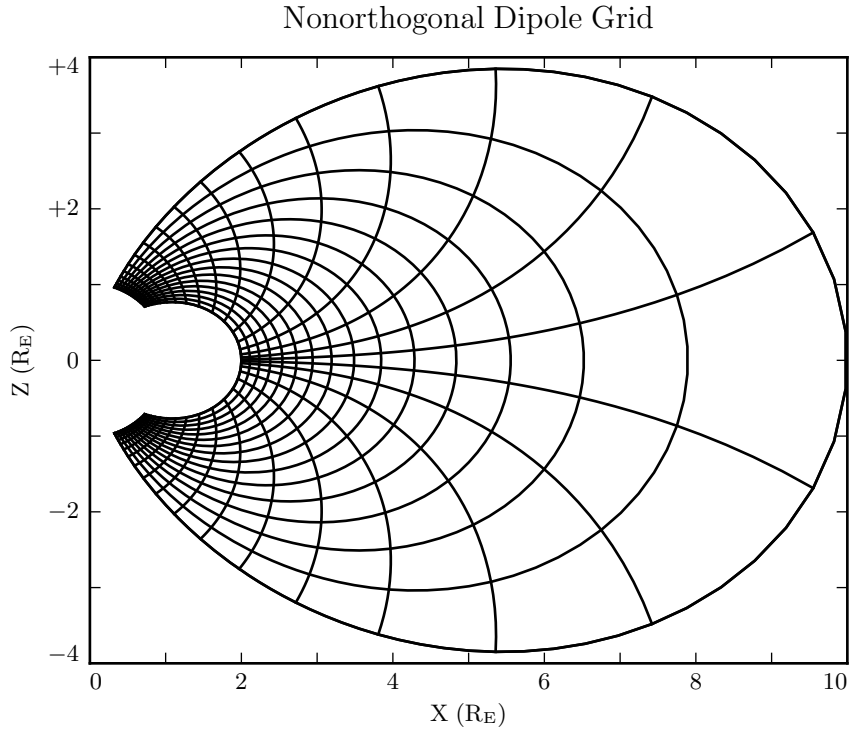


Figure 5.1: The model's nonorthogonal dipole grid. Every fifth point is shown in each direction. The high concentration of grid points near Earth's equator is a consequence of the coordinate system, which converges at the equatorial ionosphere. Earth (not shown) is centered at the origin with unit radius.

726 **5.2 Physical Parameter Profiles**

Tuna models Earth's magnetic field to be an ideal dipole, so the zeroth-order field strength is written in the usual form:

$$\underline{B}_0 = 3.1 \times 10^4 \text{ nT} \left( \frac{R_E}{r} \right)^3 \left( 2 \cos \theta \hat{r} - \sin \theta \hat{\theta} \right) \quad (5.9)$$

Number density is taken to be the sum of an inverse-radial-dependent auroral profile and a plasmaspheric profile dependent on the  $L$ -shell[61]:

$$n = n_{AZ} \frac{r_{AZ}}{r} + n_{PS} \exp\left(\frac{-L}{L_{PS}}\right) \left( \frac{1}{2} - \frac{1}{2} \tanh \frac{L - L_{PP}}{\delta L_{PP}} \right) \quad (5.10)$$

<sup>727</sup> Where typical values are shown in Table 5.1.

Table 5.1: Typical Parameters for the Tuna Density Profile

Variable	Value	Description
$L_{PS}$	1.1	Scale $L$ of the plasmasphere.
$L_{PP}$	4.0	Location of the plasmapause.
$\delta L_{PP}$	0.1	Thickness of the plasmapause.
$n_{AZ}$	$10 / \text{cm}^3$	Number density at the base of the auroral zone.
$n_{PS}$	$10^4 / \text{cm}^3$	Number density at the base of the plasmasphere.
$r_{AZ}$	$1 \text{ R}_E$	Scale height of the auroral density distribution.

The perpendicular component of the electric tensor,  $\epsilon_{\perp}$ , is computed based on Kelley's[47] tabulated low-density values,  $\epsilon_K$ , which are adjusted to take into account the effects of high density in the plasmapause.

$$\epsilon_{\perp} = \epsilon_K + \frac{Mn}{B_0^2} \quad (5.11)$$

<sup>728</sup> Where  $M$  is the mean molecular mass, which is large ( $\sim 28 \text{ u}$ ) at 100 km altitude, then  
<sup>729</sup> drops quickly (down to 1 u by  $\sim 1000 \text{ km}$ )[61].

<sup>730</sup> The Alfvén speed profile is computed from the perpendicular electric constant in the  
<sup>731</sup> usual way,  $v_A^2 \equiv \frac{1}{\mu_0 \epsilon_{\perp}}$ . This form takes into account the effect of the displacement  
<sup>732</sup> current, which becomes important in regions where the Alfvén speed approaches the  
<sup>733</sup> speed of light.

<sup>734</sup> While the density profile is held constant for all runs discussed in the present work,  
<sup>735</sup> the Alfvén speed profile is not. Four different profiles are used for the low-density

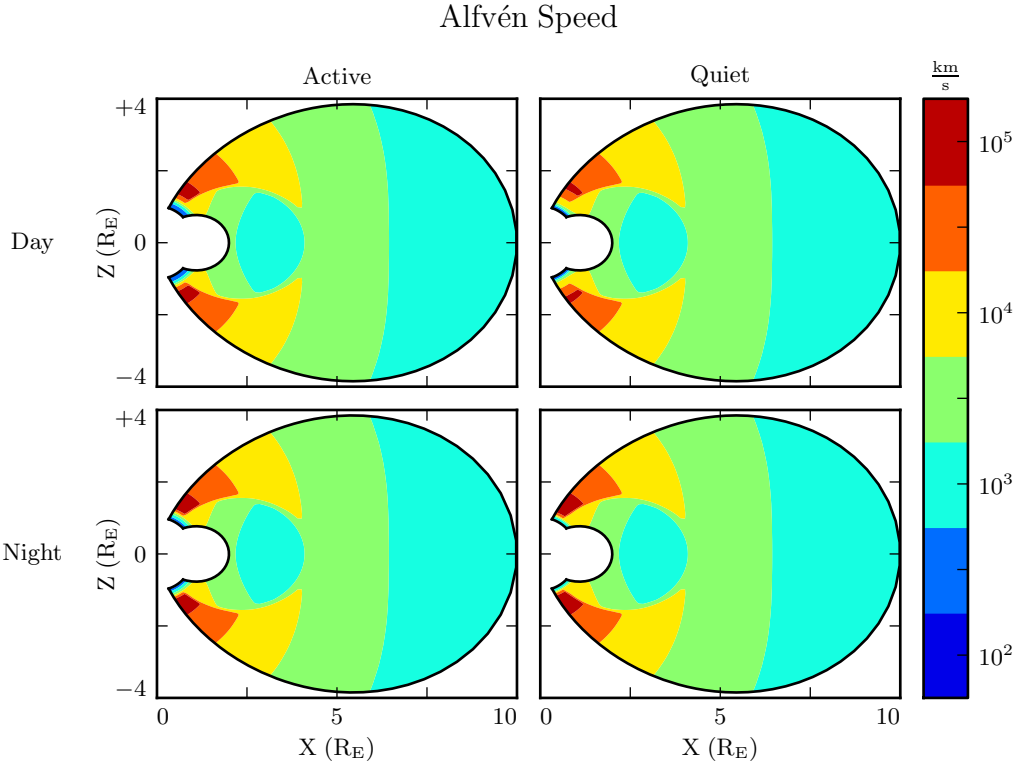


Figure 5.2: Alfvén speed profiles are based on low-density values tabulated by Kelley[47]. They are adjusted to take into account the density of the plasmapause and mass loading near the Earthward boundary.

736 perpendicular electric constant  $\epsilon_K$ , corresponding to the differing ionospheric conditions  
 737 between the dayside and the nightside, and between the high and low points in the  
 738 solar cycle. These differences are visible in Figure 5.2, particularly in the size of the  
 739 ionospheric Alfvén resonator (the peak in Alfvén speed in the high-latitude ionosphere).

740 Ionospheric conductivity profiles are also based on values tabulated by Kelley, adjusted  
 741 by Lysak[61] to take into account the abundance of heavy ions near the Earthward  
 742 boundary. Pedersen, Hall, and parallel conductivities are each resolved by altitude, as  
 743 shown in Figure 5.3.

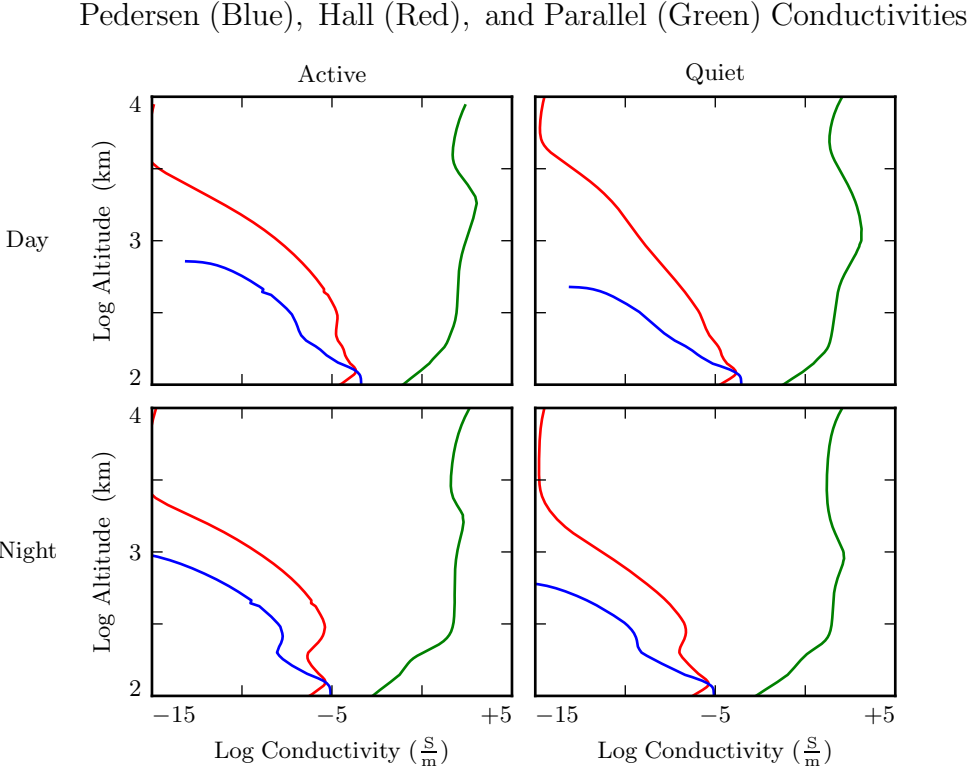


Figure 5.3: Ionospheric conductivity profiles are adapted by Lysak[61] from Kelley's tabulated values[47], in order to take into account the effects of heavy ions at low altitudes. These profiles allow Tuna to simulate magnetosphere-ionosphere coupling under a variety of conditions.

744 Tuna's physical parameter profiles are static over the course of each run. Even so-called  
 745 ultra low frequency waves like Pc4 pulsations are fast compared to convective timescales  
 746 in the magnetosphere.

747 **5.3 Driving**

748 Models similar to Tuna have traditionally been driven using compression at the outer  
 749 boundary[58, 61, 97, 98]. Such driving acts as a proxy for solar wind compression,  
 750 Kelvin-Helmholtz effects at the magnetopause, and so on. However, because of the

751 guided nature of high-modenumber Alfvén waves, simulations driven from the outer  
752 boundary are constrained to the consideration of waves with low azimuthal modenumber  
753 (equivalently, large azimuthal wavelength).

754 This issue is demonstrated in Figure 5.4. At low modenumber, energy delivered at  
755 the outer boundary propagates across field lines in order to stimulate resonances in  
756 the inner magnetosphere. However, as modenumber increases, Alfvén waves become  
757 increasingly guided, and the inner magnetosphere is unaffected by perturbations at the  
758 outer boundary.

759 In order to simulate high-modenumber Alfvén waves in the inner magnetosphere — such  
760 as giant pulsations — a new driving mechanism is necessary. Perturbation of the ring  
761 current is a natural choice, as Alfvén waves in the Pc4 range are known to interact with  
762 ring current particles through drift and drift-bounce resonances. The ring current is a  
763 dynamic region, particularly during and after geomagnetic storms and substorms; it's  
764 easy to imagine the formation of localized inhomogeneities.

765 In order to estimate an appropriate magnitude for perturbations of the ring current, the  
766 Sym-H storm index<sup>6</sup> is used. The index is measured once per minute, and so cannot  
767 directly detect ring current modulations in the Pc4 frequency range. Instead, the index  
768 is transformed into the frequency domain, allowing a fit of its pink noise<sup>7</sup>.

769 As shown in Figure 5.5, a Fourier transform of the Sym-H index (taken here from the  
770 June 2013 storm) suggests that magnetic field perturbations at Earth's surface due to  
771 ring current activity in the Pc4 frequency range could be up to the order of  $10^{-2}$  nT.  
772 Supposing that the ring current is centered around  $5 R_E$  geocentric, that corresponds to  
773 a current on the order of 0.1 MA. Tuna's driving is spread using a Gaussian profile in  
774  $u^1$  (typically centered at  $L = 5$ ) and  $u^3$  (typically centered just off the equator), with a  
775 characteristic area of  $1 R_E^2$ ; this gives a current density on the order of  $10^{-4} \mu\text{A}/\text{m}^2$ .

776 Admittedly, Sym-H is an imperfect tool for estimating the magnitude of localized per-  
777 turbations to the ring current, particularly those with high modenumber. As a global

---

<sup>6</sup>Sym-H is analogous to DST, and the two match each other closely[96]. The crucial difference in this case is that Sym-H is recorded at a higher frequency.

<sup>7</sup>Pink noise, also called  $\frac{1}{f}$  noise, refers to the power law decay present in the Fourier transforms of all manner of physical signals.

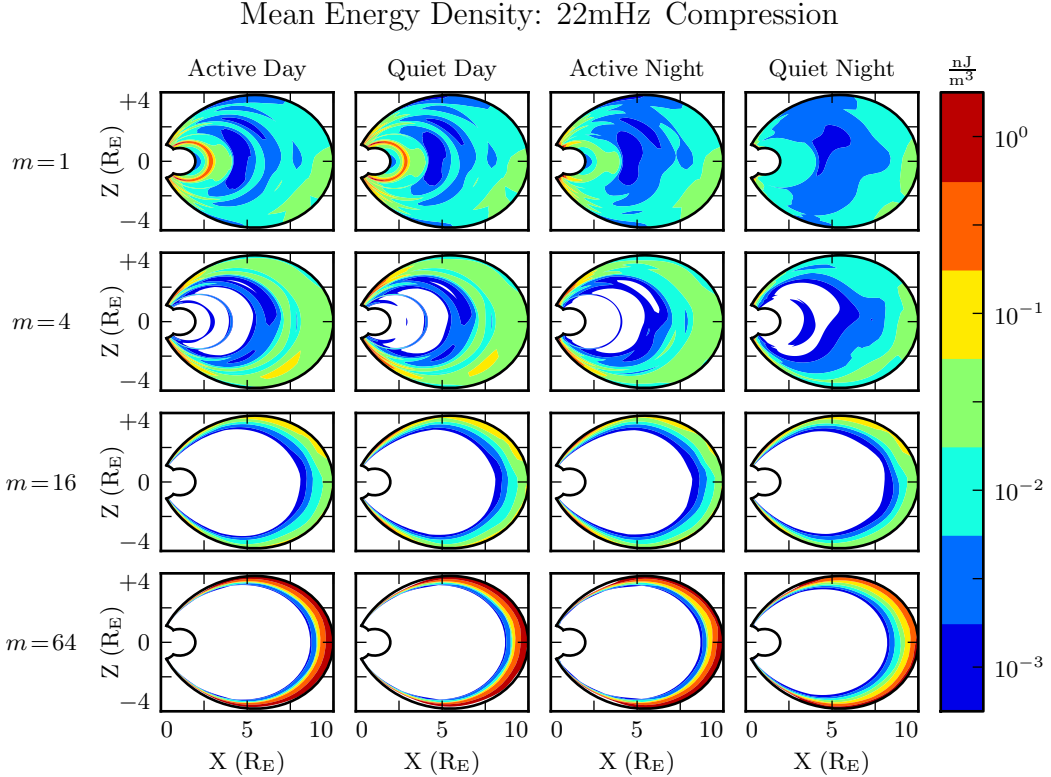


Figure 5.4: Each cell presents the mean energy density over the course of a 300 s run, as a function of position, due to compressional driving at the outer boundary. Azimuthal modenumber varies by row, and ionospheric conditions vary by column. For runs with small azimuthal modenumber, it's clear that energy is able to propagate across field lines and stimulate wave activity in the inner magnetosphere. When the modenumber is large, energy is unable to penetrate to the inner magnetosphere. Notably, the large values on the bottom row should be taken with a grain of salt; it's not clear that the model's results are reliable when waves are continuously forced against the boundary.

778 index, its values are effectively averaged around Earth. Unlike in situ measurements,  
 779 however, this method has the advantage of estimating total driving current (and thus  
 780 total energy input).

781 In the results shown in Chapters 6 and 7, the driving current is sinusoidal, and delivered  
 782 purely in the azimuthal direction (representing a perturbation to the magnitude of the

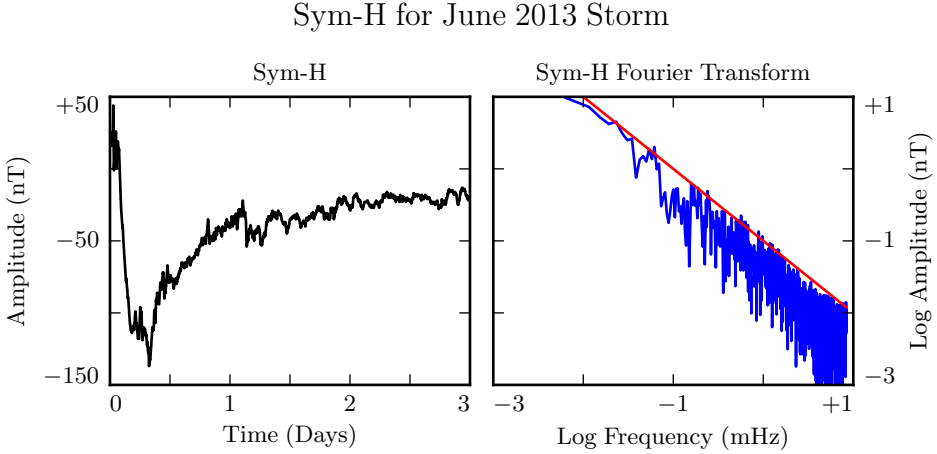


Figure 5.5: The Sym-H storm index[69] measures magnetic perturbations on Earth’s surface due to ring current activity. The amplitude of oscillations in the Pc4 range is estimated by fitting the pink noise in its Fourier transform.

783 ring current, but not to its direction). Tuna also allows several other driving waveforms,  
 784 and the direction of the current could be modified with trivial modifications to the code.

## 785 5.4 Maxwell’s Equations

786 Tuna simulates the evolution of electromagnetic waves in accordance with Ampère’s  
 787 law and Faraday’s law. Computation is carried out on a Yee grid[102]: electric fields  
 788 and magnetic fields are offset by half a time step, and each field component is defined  
 789 on either odd or even grid points in each dimension to ensure that curls are computed  
 790 using centered differences.

The Ohmic current in Ampère’s law is replaced with  $\underline{\sigma} \cdot \underline{E}$  per Kirchhoff’s formulation of Ohm’s law. Then, taking  $\underline{J}$  to represent the driving current discussed in Section 5.3, Maxwell’s equations are written

$$\frac{\partial}{\partial t} \underline{B} = -\nabla \times \underline{E} \quad \underline{\epsilon} \cdot \frac{\partial}{\partial t} \underline{E} = \frac{1}{\mu_0} \nabla \times \underline{B} - \underline{J} - \underline{\sigma} \cdot \underline{E} \quad (5.12)$$

It is convenient to introduce shorthand for the curl of each field:  $\underline{C} \equiv \nabla \times \underline{E}$  and  $\underline{F} \equiv \nabla \times \underline{B} - \mu_0 \underline{J}$ . Or, recalling Equation (5.6),

$$C^i = \frac{\varepsilon^{ijk}}{\sqrt{g}} \frac{\partial}{\partial u^j} E_k \quad F^i = \frac{\varepsilon^{ijk}}{\sqrt{g}} \frac{\partial}{\partial u^j} B_k - J^i \quad (5.13)$$

In these terms, Faraday's law can simply be written:

$$\frac{\partial}{\partial t} B^i = -C^i \quad (5.14)$$

Writing each component out explicitly, and using the metric tensor (per Equation (5.5)) to eliminate contravariant magnetic field components<sup>8</sup>, Equation (5.14) becomes:

$$\begin{aligned} B_1 &\leftarrow B_1 - g_{11} \delta t C^1 - g_{13} \delta t C^3 \\ B_2 &\leftarrow B_2 - g_{22} \delta t C^2 \\ B_3 &\leftarrow B_3 - g_{31} \delta t C^1 - g_{33} \delta t C^3 \end{aligned} \quad (5.15)$$

791 Note that the  $\leftarrow$  operator is used in Equation (5.15) to indicate assignment, rather than  
792 equality. Terms on the left are new, while those on the right are old.

Unlike Faraday's law, Ampère's law cannot be trivially solved. Not only does the time derivative of  $\underline{E}$  depend on its own future value, but the crosswise and azimuthal components of the equation are coupled by the Hall terms in the conductivity tensor. Fortunately, the electric tensor can be inverted, allowing a solution by integrating factors:

$$\underline{\underline{\epsilon}} \cdot \frac{\partial}{\partial t} \underline{E} = \frac{1}{\mu_0} \underline{F} - \underline{\underline{\sigma}} \cdot \underline{E} \quad \text{becomes} \quad \left( \underline{\underline{\Omega}} + \underline{\underline{\epsilon}} \frac{\partial}{\partial t} \right) \cdot \underline{E} = \underline{\underline{V}}^2 \cdot \underline{F} \quad (5.16)$$

---

<sup>8</sup>Fields are stored only in terms of their covariant components, and curls in terms of their contravariant components. This reduces Tuna's memory footprint (since each field need not be stored twice) as well as its computational cost (since time need not be spent rotating between bases). As a result, Tuna's solutions to Maxwell's equations are linear expressions whose coefficients are a mishmash of physical constants and geometric factors. To save time, each coefficient is computed once and stored, rather than being multiplied out from scratch with each time step.

Where  $\underline{\underline{\mathbb{I}}}$  is the identity tensor and in  $x$ - $y$ - $z$  coordinates<sup>9</sup>,

$$\underline{\underline{V}^2} \equiv \frac{1}{\mu_0} \underline{\underline{\epsilon}}^{-1} = \begin{bmatrix} v_A^2 & 0 & 0 \\ 0 & v_A^2 & 0 \\ 0 & 0 & c^2 \end{bmatrix} \quad \text{and} \quad \underline{\underline{\Omega}} \equiv \underline{\underline{\epsilon}}^{-1} \cdot \underline{\underline{\sigma}} = \begin{bmatrix} \frac{\sigma_P}{\epsilon_\perp} & \frac{-\sigma_H}{\epsilon_\perp} & 0 \\ \frac{\sigma_H}{\epsilon_\perp} & \frac{\sigma_P}{\epsilon_\perp} & 0 \\ 0 & 0 & \frac{\sigma_0}{\epsilon_0} \end{bmatrix} \quad (5.17)$$

Multiplying through by  $\exp(\underline{\underline{\Omega}} t)$  and applying the product rule, Equation (5.16) becomes<sup>10</sup>

$$\frac{\partial}{\partial t} \left( \exp(\underline{\underline{\Omega}} t) \cdot \underline{\underline{E}} \right) = \exp(\underline{\underline{\Omega}} t) \cdot \underline{\underline{V}^2} \cdot \underline{\underline{F}} \quad (5.18)$$

Equation (5.18) can then be integrated over a small time step  $\delta t$  and expressed in terms of the assignment operator introduced in Equation (5.15).

$$\underline{\underline{E}} \leftarrow \exp(-\underline{\underline{\Omega}} \delta t) \cdot \underline{\underline{E}} + \delta t \exp(-\underline{\underline{\Omega}} \frac{\delta t}{2}) \cdot \underline{\underline{V}^2} \cdot \underline{\underline{F}} \quad (5.19)$$

The tensor exponential is evaluated by splitting  $\underline{\underline{\Omega}}$  into the sum of its diagonal and Hall components<sup>11</sup>. The Hall exponential condenses into sines and cosines, giving a rotation around the magnetic field line:

$$\underline{\underline{E}} \leftarrow \exp(-\underline{\underline{\Omega}}' \delta t) \cdot \underline{\underline{R}}_z \left( \frac{-\sigma_H \delta t}{\epsilon_\perp} \right) \cdot \underline{\underline{E}} + \delta t \underline{\underline{V}^2} \cdot \exp(-\underline{\underline{\Omega}}' \frac{\delta t}{2}) \cdot \underline{\underline{R}}_z \left( \frac{-\sigma_H \delta t}{2\epsilon_\perp} \right) \cdot \underline{\underline{F}} \quad (5.20)$$

Where

$$\underline{\underline{R}}_z(\theta) = \begin{bmatrix} \cos \theta & -\sin \theta & 0 \\ \sin \theta & \cos \theta & 0 \\ 0 & 0 & 1 \end{bmatrix} \quad \text{and} \quad \underline{\underline{\Omega}}' \equiv \begin{bmatrix} \frac{\sigma_P}{\epsilon_\perp} & 0 & 0 \\ 0 & \frac{\sigma_P}{\epsilon_\perp} & 0 \\ 0 & 0 & \frac{\sigma_0}{\epsilon_0} \end{bmatrix} \quad (5.21)$$

---

<sup>9</sup>Note the parallel component of the present definition of  $\underline{\underline{\Omega}}$  differs slightly from that used in Chapter 4, due to the present chapter's neglect of inertial effects; see Chapter 6.

<sup>10</sup>Tensor exponentiation is analogous to scalar exponentiation[37]:  $\exp(\underline{\underline{T}}) \equiv \sum_n \frac{1}{n!} \underline{\underline{T}}^n$ .

<sup>11</sup>For tensors,  $\exp(\underline{\underline{S}} + \underline{\underline{T}}) = \exp(\underline{\underline{S}}) \exp(\underline{\underline{T}})$  as long as  $\underline{\underline{S}} \cdot \underline{\underline{T}} = \underline{\underline{T}} \cdot \underline{\underline{S}}$ .

The parallel component of term of Equation (5.20) is simply

$$E_z \leftarrow E_z \exp\left(\frac{-\sigma_0 \delta t}{\epsilon_0}\right) + c^2 \delta t F_z \exp\left(\frac{-\sigma_0 \delta t}{2\epsilon_0}\right) \quad (5.22)$$

Or, using Equation (5.7) to map to the covariant basis,

$$E_3 \leftarrow E_3 \exp\left(\frac{-\sigma_0 \delta t}{\epsilon_0}\right) + c^2 \delta t (g_{31} F^1 + g_{33} F^3) \exp\left(\frac{-\sigma_0 \delta t}{2\epsilon_0}\right) \quad (5.23)$$

793 Tuna's conductivity profile gives a minimum value of  $\frac{\sigma_0 \delta t}{\epsilon_0}$  on the order of  $10^3$ , making  
 794  $\exp\left(\frac{-\sigma_0 \delta t}{\epsilon_0}\right)$  far too small to be stored in a double precision variable<sup>12</sup>. That is, this  
 795 model takes  $E_3$  (and, proportionally,  $E_z$ ) to be uniformly zero. This issue is revisited  
 796 in Chapter 6.

The perpendicular components of Equation (5.20) give the expressions:

$$\begin{aligned} E_1 + \frac{g^{13}}{g^{11}} E_3 &\leftarrow E_1 \cos\left(\frac{-\sigma_H \delta t}{\epsilon_\perp}\right) \exp\left(\frac{-\sigma_P \delta t}{\epsilon_\perp}\right) \\ &+ E_2 \sin\left(\frac{-\sigma_H \delta t}{\epsilon_\perp}\right) \exp\left(\frac{-\sigma_P \delta t}{\epsilon_\perp}\right) \sqrt{\frac{g^{22}}{g^{11}}} \\ &+ E_3 \cos\left(\frac{-\sigma_H \delta t}{\epsilon_\perp}\right) \exp\left(\frac{-\sigma_P \delta t}{\epsilon_\perp}\right) \frac{g^{13}}{g^{11}} \\ &+ F^1 \cos\left(\frac{-\sigma_H \delta t}{2\epsilon_\perp}\right) \exp\left(\frac{-\sigma_P \delta t}{2\epsilon_\perp}\right) \frac{v_A^2 \delta t}{g^{11}} \\ &+ F^2 \sin\left(\frac{-\sigma_H \delta t}{2\epsilon_\perp}\right) \exp\left(\frac{-\sigma_P \delta t}{2\epsilon_\perp}\right) \frac{v_A^2 \delta t}{\sqrt{g^{11} g^{22}}} \end{aligned} \quad (5.24)$$

---

<sup>12</sup>Not coincidentally,  $\frac{\sigma_0}{\epsilon_0}$  can also be written  $\frac{\omega_P^2}{\nu}$ . At the ionosphere, the collision frequency  $\nu$  is fast compared to field line resonance timescales, but it's still slow compared to the plasma frequency.

and

$$\begin{aligned}
E_2 \leftarrow & -E_1 \sin\left(\frac{-\sigma_H \delta t}{\epsilon_{\perp}}\right) \exp\left(\frac{-\sigma_P \delta t}{\epsilon_{\perp}}\right) \sqrt{\frac{g^{11}}{g^{22}}} \\
& + E_2 \cos\left(\frac{-\sigma_H \delta t}{\epsilon_{\perp}}\right) \exp\left(\frac{-\sigma_P \delta t}{\epsilon_{\perp}}\right) \\
& - E_3 \sin\left(\frac{-\sigma_H \delta t}{\epsilon_{\perp}}\right) \exp\left(\frac{-\sigma_P \delta t}{\epsilon_{\perp}}\right) \frac{g^{13}}{\sqrt{g^{11} g^{22}}} \\
& - F^1 \sin\left(\frac{-\sigma_H \delta t}{2\epsilon_{\perp}}\right) \exp\left(\frac{-\sigma_P \delta t}{2\epsilon_{\perp}}\right) \frac{v_A^2 \delta t}{\sqrt{g^{11} g^{22}}} \\
& + F^2 \cos\left(\frac{-\sigma_H \delta t}{2\epsilon_{\perp}}\right) \exp\left(\frac{-\sigma_P \delta t}{2\epsilon_{\perp}}\right) \frac{v_A^2 \delta t}{g^{22}}
\end{aligned} \tag{5.25}$$

797 The  $E_3$  terms in Equations (5.24) and (5.25) can be ignored at present. They are  
798 revisited in Chapter 6.

799 It bears recalling that the driving current is defined as part of  $\underline{F}$ , per Equation (5.13).  
800 When the driving current is purely azimuthal ( $J^1 = J^3 = 0$ ), the driving is in principle  
801 applied to both the poloidal and the toroidal electric fields through  $F^2$ . However,  
802 in practice, the driving applied to the toroidal electric field is vanishingly small. The  
803 driving current  $J^2$  is localized around  $5 R_E$  geocentric, and  $\exp\left(\frac{-\sigma_P \delta t}{2\epsilon_{\perp}}\right)$  drops off quickly  
804 with altitude.

## 805 5.5 Boundary Conditions

806 Dirichlet and Neumann boundary conditions are applied to the electric field components  
807 and magnetic field components respectively. That is, electric fields are zero at the inner  
808 and outer boundaries, and magnetic fields normal to the inner and outer boundaries are  
809 zero.

810 These boundary conditions can in principle cause nonphysical reflections at the bound-  
811 ary<sup>13</sup>. In practice, however (with a noted exception in Chapter 7), wave activity is  
812 concentrated well within the simulation domain. Simulation results are robust under

---

<sup>13</sup>See, for example, the bottom row of Figure 5.4.

813 an exchange of Dirichlet and Neumann boundary conditions, though a self-inconsistent  
 814 set of boundary conditions (such as applying Neumann conditions to  $B_1$  but Dirichlet  
 815 conditions to  $B_3$ ) quickly causes instability.

816 The Earthward boundary conditions are as follows.

Between the top of the neutral atmosphere and the bottom of the ionosphere, the model includes a thin, horizontal current sheet representing the ionosphere's  $E$  layer[58]. By integrating Ampère's law over the layer, it can be shown[27] that the horizontal electric field values at the edge of the grid are determined by the jump in the horizontal magnetic fields:

$$\underline{\underline{\Sigma}} \cdot \underline{E} = \frac{1}{\mu_0} \lim_{\delta r \rightarrow 0} \left[ \hat{r} \times \underline{B} \right]_{R_I - \delta r}^{R_I + \delta r} \quad (5.26)$$

The integrated conductivity tensor  $\underline{\underline{\Sigma}}$  is written in  $\theta$ - $\phi$  coordinates as[58]:

$$\underline{\underline{\Sigma}} \equiv \begin{bmatrix} \frac{\Sigma_0 \Sigma_P}{\Sigma_0 \cos^2 \alpha + \Sigma_P \sin^2 \alpha} & \frac{-\Sigma_0 \Sigma_H}{\Sigma_0 \cos^2 \alpha + \Sigma_P \sin^2 \alpha} \\ \frac{\Sigma_0 \Sigma_H}{\Sigma_0 \cos^2 \alpha + \Sigma_P \sin^2 \alpha} & \Sigma_P + \frac{\Sigma_H^2 \sin^2 \alpha}{\Sigma_0 \cos^2 \alpha + \Sigma_P \sin^2 \alpha} \end{bmatrix} \quad (5.27)$$

817 Where  $\alpha$  is the angle between the magnetic field and the vertical direction, given by  
 818  $\cos \alpha \equiv \frac{-2 \cos \theta}{\sqrt{1+3 \cos^2 \theta}}$ , and  $\Sigma_P$ ,  $\Sigma_H$ , and  $\Sigma_0$  are the height-integrated Pedersen, Hall,  
 819 and parallel conductivities respectively. Their values are determined by integrating  
 820 Kelley's[47] conductivity profiles from Earth's surface to the ionospheric boundary; val-  
 821 ues are shown in Table 5.2.

Table 5.2: Integrated Atmospheric Conductivity (S)

	$\Sigma_0$	$\Sigma_P$	$\Sigma_H$
Active Day	424	0.65	6.03
Quiet Day	284	0.44	4.02
Active Night	9	0.01	0.12
Quiet Night	9	0.01	0.12

822 The atmospheric conductivities of the two nightside profiles are the same, though the  
 823 profiles differ significantly at higher altitudes, as shown in Section 5.2.

An expression for the horizontal electric fields at the boundary is obtained by inverting Equation (5.26). After mapping to covariant coordinates per Equation (5.8), and taking  $\Sigma \equiv \det \underline{\underline{\Sigma}}$ ,

$$\begin{aligned} E_1 &\leftarrow \frac{1}{\mu_0 \Sigma} \lim_{\delta r \rightarrow 0} \left[ -\Sigma_{\theta\phi} B_1 - \sqrt{\frac{g_{11}}{g_{22}}} \Sigma_{\phi\phi} B_2 \right]_{R_I-\delta r}^{R_I+\delta r} \\ E_2 &\leftarrow \frac{1}{\mu_0 \Sigma} \lim_{\delta r \rightarrow 0} \left[ \sqrt{\frac{g_{22}}{g_{11}}} \Sigma_{\theta\theta} B_1 + \Sigma_{\phi\theta} B_2 \right]_{R_I-\delta r}^{R_I+\delta r} \end{aligned} \quad (5.28)$$

824 The atmospheric field is computed in terms of a scalar magnetic potential,  $\Psi$ , such  
 825 that  $\underline{B} = \nabla \Psi$ . The neutral atmosphere is considered to be a perfect insulator, giving  
 826  $\nabla \times \underline{B} = 0$ . Combined with  $\nabla \cdot \underline{B} = 0$  (per Maxwell's equations), this ensures that  $\Psi$   
 827 satisfies Laplace's equation,  $\nabla^2 \Psi = 0$ , and thus can be written as a sum of harmonics.

Laplace's equation can be solved analytically; however, a numerical solution is preferable to ensure orthonormality on a discrete and incomplete<sup>14</sup> grid. After separating out the radial and azimuthal dependence in the usual way, the latitudinal component of Laplace's equation is written in terms of  $s \equiv -\sin^2 \theta$ :

$$(4s^2 + 4s) \frac{d^2}{ds^2} Y_\ell + (4 + 6s) \frac{d}{ds} Y_\ell - \frac{m^2}{s} Y_\ell = \ell (\ell + 1) Y_\ell \quad (5.29)$$

Using centered differences to linearize the derivatives, Equation (5.29) becomes a system of coupled linear equations, one per field line. It is then solved numerically for eigenvalues  $\ell (\ell + 1)$  and eigenfunctions  $Y_\ell$ <sup>15</sup>. In terms of the harmonics  $Y_\ell$ , the magnetic potential between the Earth's surface and the top of the atmosphere is written using

---

<sup>14</sup>As discussed in Section 5.1, the grid is constrained to finite  $L$ , which excludes the equator as well as the poles.

<sup>15</sup>Solving Laplace's equation analytically results in spherical harmonics indexed by both  $\ell$  and  $m$ , the separation constants for  $\theta$  and  $\phi$  respectively. In two and a half dimensions,  $\phi$  is not explicitly resolved, so  $m$  is set manually.

coefficients  $a_\ell$  and  $b_\ell$ :

$$\Psi = \sum_\ell \left( a_\ell r^\ell + b_\ell r^{-\ell-1} \right) Y_\ell \quad (5.30)$$

As a boundary condition for  $\Psi$ , Earth is assumed to be a perfect conductor. This forces the magnetic field at Earth's surface to be horizontal; that is,  $B_r = \frac{\partial}{\partial r} \Psi = 0$ . Noting that solutions to Laplace's equation are orthonormal, each element of the sum in Equation (5.30) must be independently zero at  $R_E$ . This allows the coefficients  $a_\ell$  and  $b_\ell$  to be expressed in terms of one another.

$$b_\ell = \frac{\ell}{\ell+1} R_E^{2\ell+1} a_\ell \quad (5.31)$$

The current sheet at the top of the atmosphere is assumed to be horizontal, so the radial component of the magnetic field must be the same just above and just below it. Taking the radial derivative of Equation (5.30) at the top of the atmosphere, and eliminating  $b_\ell$  with Equation (5.31), gives

$$B_r = \sum_\ell \ell a_\ell R_I^{\ell-1} \left( 1 - \lambda^{2\ell+1} \right) Y_\ell \quad \text{where} \quad \lambda \equiv \frac{R_E}{R_I} \sim 0.975 \quad (5.32)$$

The summation is collapsed by “integrating” over a harmonic<sup>16</sup>. Inverse harmonics are obtained by inverting the eigenvector matrix. Then  $Y_\ell \cdot Y_{\ell'}^{-1} = \delta_{\ell\ell'}$  by construction.

$$a_\ell = \frac{1}{\ell R_I^{\ell-1}} \frac{B_r \cdot Y_\ell^{-1}}{1 - \lambda^{2\ell+1}} \quad (5.33)$$

Combining Equations (5.30), (5.31), and (5.33) allows the expression of  $\Psi$  at the top and bottom of the atmosphere as a linear combination of radial magnetic field components

---

<sup>16</sup>Because the functions are defined on a discrete grid, their inner product is not an integral, but a sum:  $B_r \cdot Y_\ell^{-1} \equiv \sum_i B_r[i] Y_\ell^{-1}[i]$ .

at the bottom of the ionosphere.

$$\begin{aligned}\Psi_E &= \sum_{\ell} Y_{\ell} \frac{R_I}{\ell (\ell - 1)} \frac{(2\ell - 1) \lambda^{\ell}}{1 - \lambda^{2\ell+1}} B_r \cdot Y_{\ell}^{-1} \\ \Psi_I &= \sum_{\ell} Y_{\ell} \frac{R_I}{\ell (\ell - 1)} \frac{(\ell - 1) + \ell \lambda^{2\ell+1}}{1 - \lambda^{2\ell+1}} B_r \cdot Y_{\ell}^{-1}\end{aligned}\tag{5.34}$$

Horizontal magnetic fields are obtained by taking derivatives of  $\Psi$ .

$$B_1 = \frac{\partial}{\partial u^1} \Psi \quad B_2 = \frac{\partial}{\partial u^2} \Psi\tag{5.35}$$

- 828    Horizontal magnetic field values at the top of the atmosphere are used to impose bound-
- 829    ary conditions on the electric fields at the bottom of the ionosphere, per Equation (5.28).
- 830    Those at Earth's surface are valuable because they allow a direct comparison between
- 831    model output and ground magnetometer data, after being mapped to physical coordi-
- 832    nates per Equation (5.8).

<sup>833</sup> **Chapter 6**

<sup>834</sup> **Electron Inertial Effects**

<sup>835</sup> As laid out in Chapter 5, Tuna resolves neither currents nor electric fields parallel to  
<sup>836</sup> the background magnetic field. This is unfortunate; parallel electric fields generated by  
<sup>837</sup> kinetic and inertial Alfvén waves (including fundamental field line resonances[77, 93])  
<sup>838</sup> are a topic of particular interest in the study of auroral particle precipitation.

Parallel currents and electric fields can be added to Tuna through the consideration of electron inertial effects in Ohm's law:

$$0 = \sigma_0 E_z - J_z \quad \text{becomes} \quad \frac{1}{\nu} \frac{\partial}{\partial t} J_z = \sigma_0 E_z - J_z \quad (6.1)$$

With the addition of the electron inertial term, it is necessary to track the parallel current independent of the parallel electric field<sup>1</sup>. Solving by integrating factors<sup>2</sup> gives

$$J_3 \leftarrow J_3 \exp(-\nu \delta t) + \delta t \frac{ne^2}{m_e} E_3 \exp(-\nu \frac{\delta t}{2}) \quad (6.2)$$

---

<sup>1</sup>The parallel current  $J_z$  is defined on the same points of the Yee grid as  $E_z$ . It is offset in time by half of a time step.

<sup>2</sup>The integrating factors technique is laid out explicitly for Ampère's law in Section 5.4.

From there, the parallel electric field can be updated directly; Equation (5.23) is replaced by the following:

$$E_3 \leftarrow E_3 + c^2 \delta t (g_{31} F^1 + g_{33} F^3) - \frac{\delta t}{\epsilon_0} J_3 \quad (6.3)$$

839 The present section explores the complications that arise from the addition of the elec-  
 840 tron inertial term to Ohm's law, as well as a few results that may be gleaned despite  
 841 those complications. Notably — for reasons discussed in Section 6.3 — the results  
 842 presented in Chapter 7 do not make use of the effects of electron inertia.

843 Inertial effects have been considered in previous numerical work, such as by Lysak and  
 844 Song in 2001[60], but never at the global scale. That work considered waves in the  
 845 ionospheric Alfvén resonator, with frequencies of hundreds of mHz, and did not account  
 846 for the effects of the dipolar geometry. In fact, in that work, circular polarization  
 847 (essentially a superposition of poloidal and toroidal modes) was noted to be a promising  
 848 avenue for future work.

## 849 6.1 The Boris Factor

With the addition of the electron inertial term, a cyclical dependence appears between Ampère's law and Ohm's law:

$$\frac{\partial}{\partial t} E_z \sim -\frac{1}{\epsilon_0} J_z \quad \text{and} \quad \frac{\partial}{\partial t} J_z \sim \frac{ne^2}{m_e} E_z \quad \text{so} \quad \frac{\partial^2}{\partial t^2} E_z \sim -\omega_P^2 E_z \quad (6.4)$$

850 That is, electron inertial effects come hand in hand with the plasma oscillation.  
 851 As mentioned in Chapter 4 and shown in Figure 6.1, plasma oscillation is quite fast —  
 852 several orders of magnitude smaller than Tuna's time step as determined in Section 5.1  
 853 ( $\sim 10 \mu\text{s}$ ). This poses a conundrum. At Tuna's usual time step, the plasma oscillation  
 854 becomes unstable within seconds<sup>3</sup>. On the other hand, reducing the time step by three

---

<sup>3</sup>For stability,  $\omega_P \delta t < 1$  is necessary.

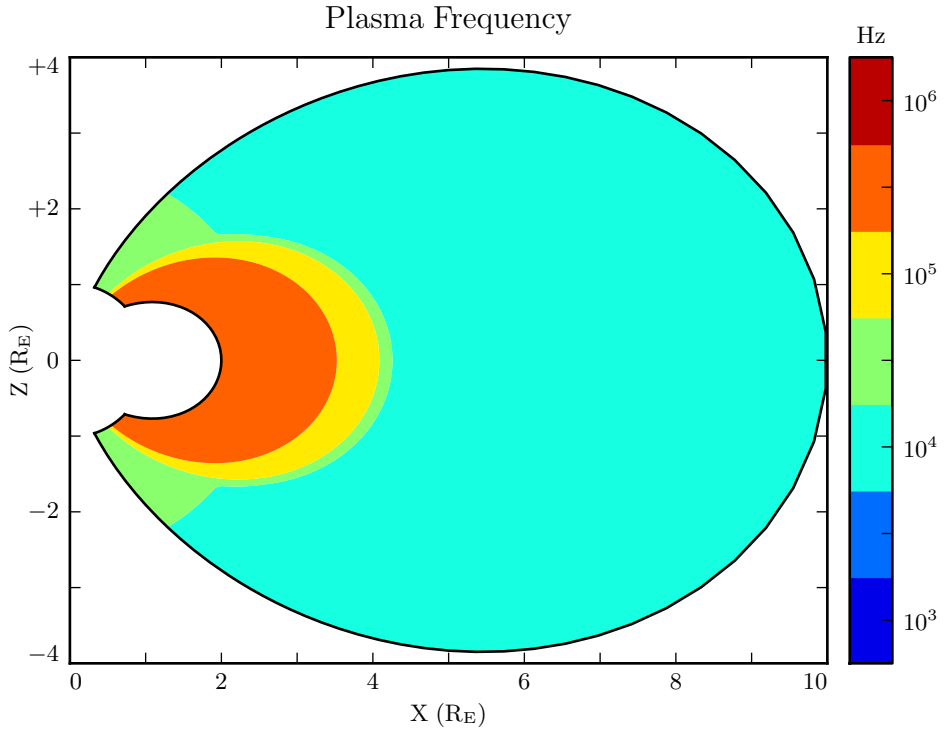


Figure 6.1: The plasma frequency reaches a peak value just under  $10^6$  Hz near the equator. Outside the plasmasphere, its value is closer to  $10^4$  Hz, which is still not well-resolved by Tuna's usual time step.

orders of magnitude to resolve the plasma oscillation is computationally infeasible; a run slated for an hour would require six weeks to complete.

As it happens, this problem can be solved by artificially increasing the parallel electric constant above its usual value of  $\epsilon_0$ . Doing so lowers both the speed of light and the plasma frequency within the simulation. This technique — and others like it — has been widespread in numerical modeling since it was presented by Boris in 1970[6]. The following paraphrases an argument by Lysak and Song[60], outlining its validity specifically in the case of electron inertial effects.

Supposing that the current and electric field are oscillating at frequency  $\omega$ , the parallel components of Ampère's law and Ohm's law can be written

$$-i\omega\epsilon_0 E_z = \frac{1}{\mu_0} (\nabla \times \underline{B})_z - J_z \quad -\frac{i\omega}{\nu} J_z = \sigma_0 E_z - J_z \quad (6.5)$$

Then, eliminating the current, the parallel electric field can be related to the curl of the magnetic field by<sup>4</sup>

$$\left(1 - \frac{\omega^2 - i\nu\omega}{\omega_P^2}\right) E_z = \frac{c^2}{\omega_P^2} (\nu - i\omega) (\nabla \times \underline{B})_z \quad (6.6)$$

- 863 In Equation (6.6),  $\frac{c}{\omega_P}$  is the electron inertial length. While the speed of light and the
- 864 plasma frequency each depend on  $\epsilon_0$ , their ratio does not. This allows an estimation of
- 865 how much the model should be affected by an artificially-large electric constant (and
- 866 thus an artificially-small plasma frequency). So long as  $\frac{\omega^2 - i\nu\omega}{\omega_P^2}$  remains small compared
- 867 to unity, the model should behave physically.
- 868 For waves with periods of a minute or so, even perhaps-implausibly large Boris factors
- 869 are allowed; for example, increasing  $\epsilon_0$  by a factor of  $10^6$  gives  $\left|\frac{\omega^2 + i\omega\nu}{\omega_P^2}\right| \lesssim 0.01$ .

## 870 6.2 Parallel Currents and Electric Fields

- 871 As discussed in Section 4.4, parallel electric fields in this regime are expected to be at
- 872 least six orders of magnitude smaller than the perpendicular electric fields. Numerical
- 873 results show general agreement: in Figure 6.2, the parallel electric field appears compa-
- 874 rable to its perpendicular counterparts only after its been scaled up by a factor of  $10^6$ .

875

- 876 As such, the inclusion of electron inertial effects does not appreciably impact the sim-
- 877 ulation's gross behavior. In Faraday's law,  $\nabla \times \underline{E}$  is unaffected, to the extent that
- 878 side-by-side magnetic field snapshots with and without electron inertial effects are not
- 879 visibly distinguishable (not shown). In a sense, this is reassuring. It ensures that the

---

<sup>4</sup>From Equation (4.4),  $c^2 \equiv \frac{1}{\mu_0\epsilon_0}$  and  $\sigma_0 \equiv \frac{ne^2}{m_e\nu}$  and  $\omega_P^2 \equiv \frac{ne^2}{m_e\epsilon_0}$ .

Electric Field Snapshots: Quiet Day, 16mHz Current,  $m = 16$

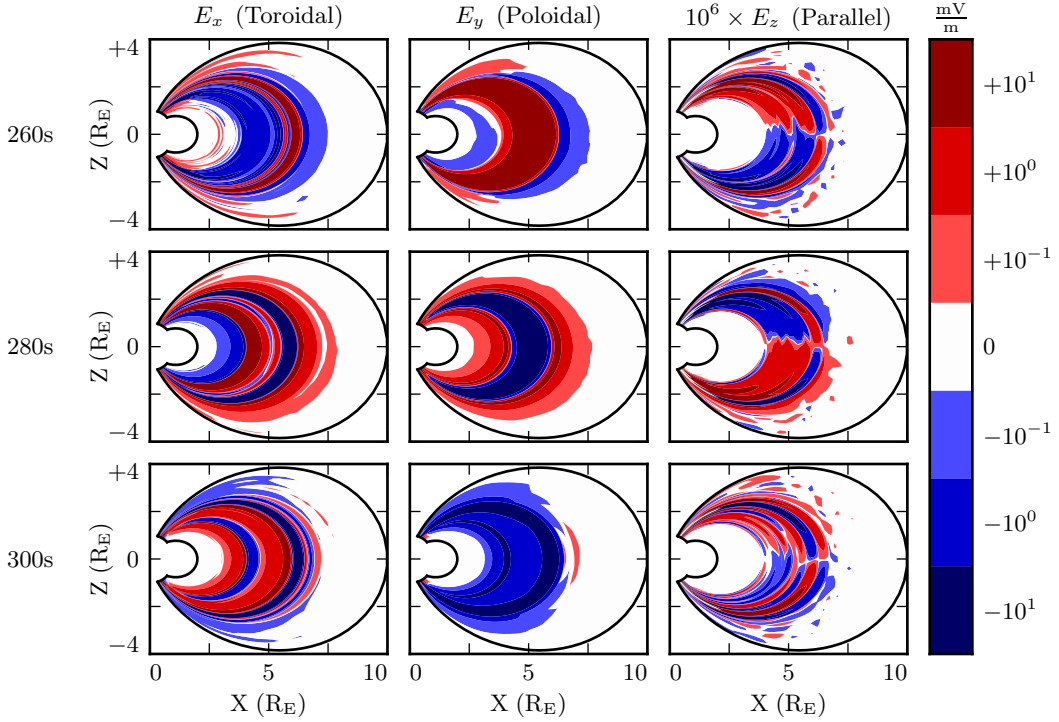


Figure 6.2: Parallel electric fields are smaller than perpendicular electric fields by about six orders of magnitude. As a result, parallel electric fields do not contribute significantly to  $\nabla \times \underline{E}$  in Faraday's law.

- 880 present section does not cast doubt on the results presented in Chapter 7, where electron  
 881 inertial effects are neglected.
- 882 Even if there is no significant feedback through Faraday's law, it's informative to con-  
 883 sider the structures that arise in parallel currents and electric fields driven by pertur-  
 884 bations in the ring current. For example, in Figure 6.2, the parallel electric field per-  
 885 turbation (with maxima near the ionosphere) exhibits the opposite harmonic structure  
 886 to the perpendicular electric field components (which peak near the equator).
- 887 Figure 6.3 shows how parallel currents lines up with the Poynting flux over time. Four  
 888 runs are shown, one per row. The horizontal axis is time, and the vertical axis is latitude.  
 889 The real and imaginary components of the parallel current are shown in the first and

890 third columns respectively, while the second and fourth columns show the poloidal and  
 891 toroidal Poynting flux. Values are taken at an altitude of 1000 km.

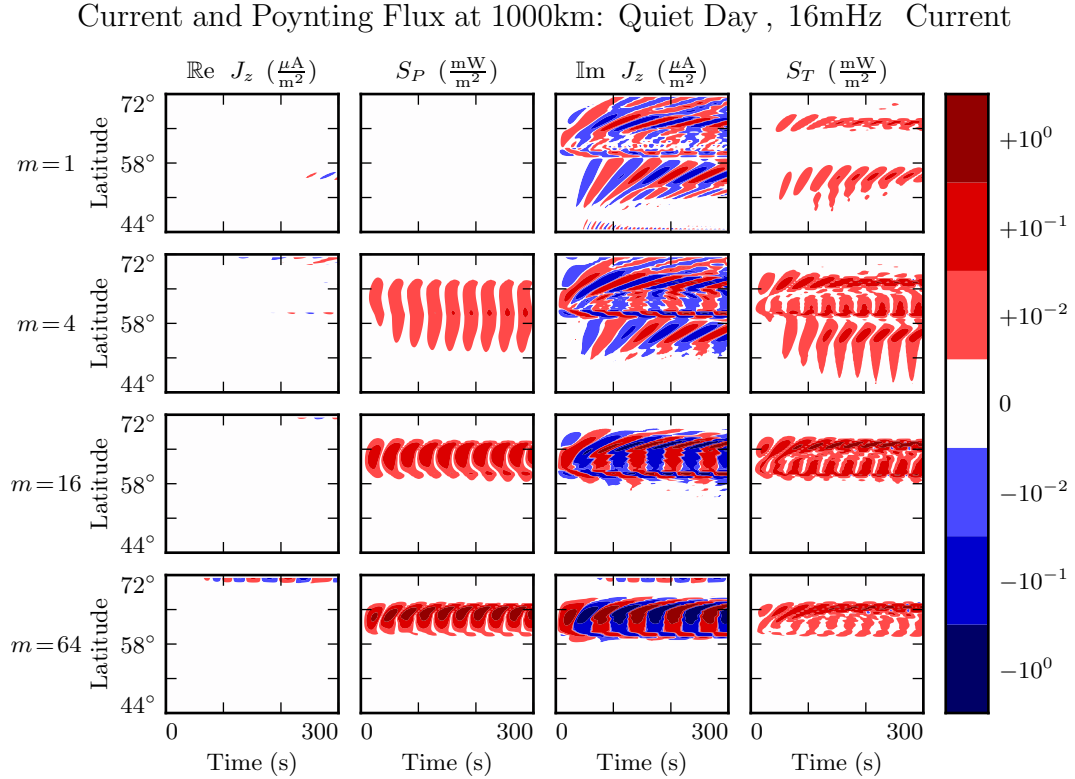


Figure 6.3: Parallel current and Poynting flux is shown for four runs, one per row, measured at an altitude of 1000 km. The parallel current is overwhelmingly imaginary, which implies a connection to the toroidal mode. Appropriately enough, the structure of the parallel current (particularly at low modenumber) seems to resemble the structure of the toroidal mode more than it does that of the poloidal mode. This is likely because the toroidal mode, with its sharp gradients across  $L$ -shells, dominates  $(\nabla \times \underline{B})_z$ .

892 Poloidal and toroidal fields are overwhelmingly real and imaginary respectively, because  
 893 they are separated from one another by an azimuthal derivative (which carries a factor  
 894 of  $i$ ). However, when a wave's polarization is rotated by the Hall conductivity, there  
 895 is no accompanying rotation in the complex plane — this gives rise to an imaginary  
 896 component of the poloidal wave and a real component of the toroidal wave.

897 In Figure 6.3, the ionospheric conductivity is small, so the imaginary component of the  
898 parallel current dominates. This implies a connection between the parallel current and  
899 the toroidal mode, and indeed, the two do exhibit qualitatively similarities. At  $m = 4$   
900 in particular, the poloidal and toroidal Poynting fluxes are similar in strength much of  
901 the time, yet the form of the parallel current strongly resembles that of the toroidal  
902 Poynting flux over the poloidal.

903 The toroidal mode's dominant effect on the parallel current at small  $m$  is not surprising.  
904 As shown in Figure 6.2, toroidal waves vary sharply in  $L^5$ . When the poloidal and  
905 toroidal magnetic fields are comparable in magnitude,  $\frac{\partial}{\partial x} B_y$  typically exceeds  $\frac{\partial}{\partial y} B_x$  (at  
906 least for  $m \lesssim 32$ ).

907 Whereas the imaginary component of the parallel current corresponds to that carried  
908 into the ionosphere by Alfvén waves, its real component comes from electric fields rotated  
909 by the Hall conductivity. Figure 6.4 shows the same four runs as Figure 6.3, but  
910 measured at 100 km, the Earthward boundary of the simulation. At that point, the real  
911 and imaginary components are similar in magnitude.

912 In Figure 6.4, as in Figure 6.3, the imaginary component of the parallel current prefer-  
913entially follows the toroidal Poynting flux. This is particularly apparent at  $m = 16$ ,  
914 where the poloidal Poynting flux is clearly stronger, yet the structure of the imaginary  
915 current resembles that of the toroidal Poynting flux. The real parallel current, on the  
916 other hand, appears to follow the poloidal Poynting flux.

917 Put another way, low- $m$  poloidal waves seem to primarily give rise to field-aligned  
918 currents only after being rotated to the toroidal mode by the Hall conductivity. At  
919 high modenumber, the two modes contribute comparably to the formation of parallel  
920 currents.

It's also possible to consider the effect of parallel currents and electric fields on the ionosphere's energy budget, per Poynting's theorem:

$$\frac{\partial}{\partial t} u = -\nabla \cdot \underline{E} - \underline{J} \cdot \underline{E} \quad (6.7)$$

---

<sup>5</sup>The sharp definition in  $L$  of the toroidal mode compared to the poloidal mode is also the topic of significant discussion in Chapter 7.

Current and Poynting Flux at 100km: Quiet Day , 16mHz Current

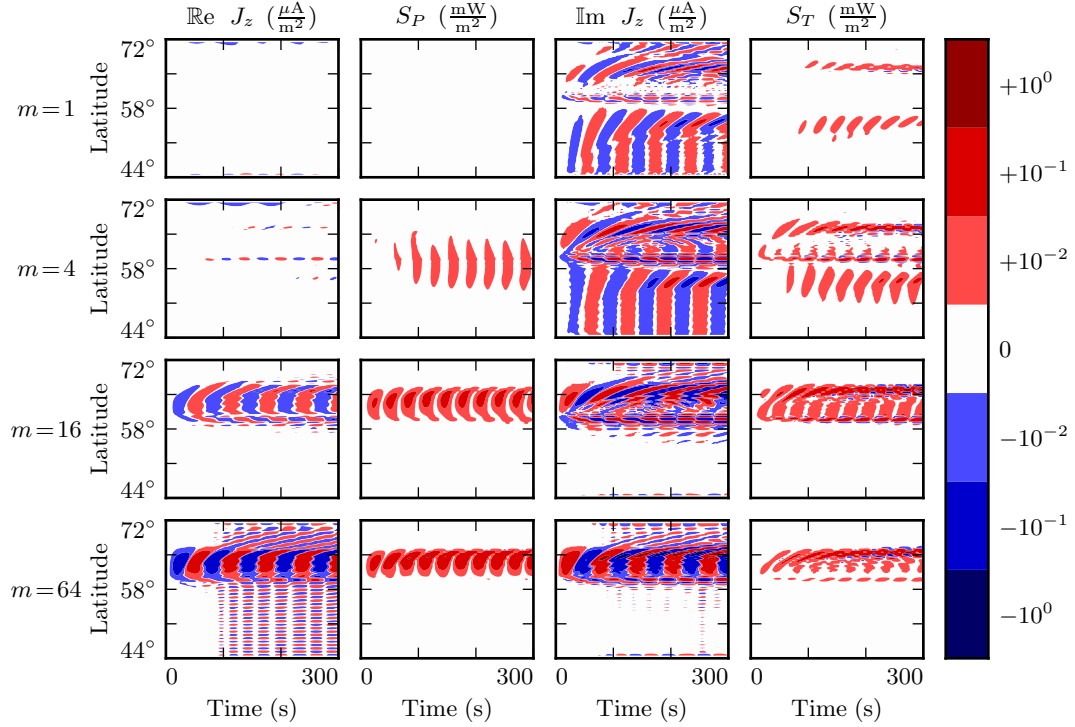


Figure 6.4: The above slices are taken from the same runs shown in Figure 6.3, but at an altitude of 100 km instead of 1000 km. The primary difference between the two altitudes is the strength of the ionospheric Hall conductivity, which directly couples the poloidal and toroidal modes. The Hall-rotated fields give rise to a real component of the parallel current, the structure of which follows the poloidal Poynting flux (as it rotates to the toroidal mode).

921 The magnitude of the parallel current tops out over  $1 \mu\text{A}/\text{m}^2$ , just shy of the up-to-tens  
 922 of  $\mu\text{A}/\text{m}^2$  inferred from ground observations and seen in situ[8, 45, 80]. However, this  
 923 current is not a significant contributor to ionospheric Joule dissipation. As shown in  
 924 Figure 6.5, the energy deposited in the ionosphere by the Poynting flux matches closely  
 925 with the energy lost to Joule dissipation — as it should, to conserve energy. But,  
 926 according to the model, Pedersen and Hall are dominant. The parallel component of  
 927  $\underline{J} \cdot \underline{E}$  is smaller by several orders of magnitude.

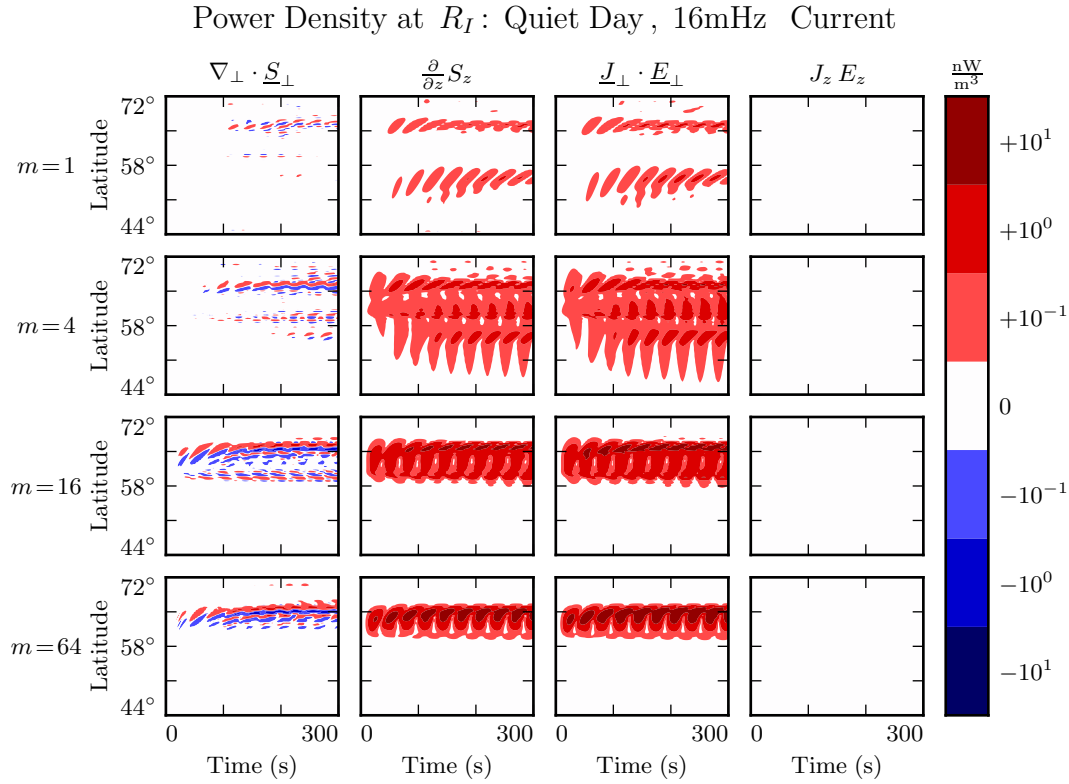


Figure 6.5: While field-aligned currents can be of significant size, they are not particularly good at depositing energy in the ionosphere. Energy deposited by the Poynting flux matches closely with Joule dissipation from the perpendicular currents, while  $J_z E_z$  is smaller by several orders of magnitude.

### 928 6.3 Inertial Length Scales

- 929 It's not quite fair to compare the parallel and perpendicular contributions to  $\nabla \times \underline{E}$  as  
 930 is done in Section 6.2. Perpendicular electric fields are on the order of 1 mV/m, with  
 931 wavelengths on the order of  $10^5$  km; they cause magnetic fields to change at a rate of  
 932 around 0.1 nT/s. Parallel electric fields, closer to  $10^{-6}$  mV/m, would need to vary over  
 933 length scales of 0.1 km to match with that.
- 934 Such scales are believable. The characteristic length scale of the plasma oscillation is the  
 935 electron inertial length,  $\frac{c}{\omega_P}$ , which is on the order of 1 km in the auroral ionosphere and

936 0.1 km in the low-altitude plasmasphere. However, Tuna’s grid out bottoms out closer  
 937 to 10 km. That is, with the inclusion of electron inertial effects, the grid is too coarse  
 938 to resolve all of the waves expected to be present. The model is prone to instability as  
 939 a result — for example, “wiggles” are visible in the bottom-left subplot of Figure 6.4.

940 Figure 6.6 shows a run with perpendicular resolution smaller than the electron inertial  
 941 length, side by side with an analogous run on the typical grid described in Chapter 5. In  
 942 order to carry out the inertial-scale run, several concessions were made to computational  
 943 cost. The run simulates only a duration of 100 s (other figures in the present chapter,  
 944 and those in Chapter 7, show 300 s), and the grid covers only the auroral latitudes from  
 945  $L = 5$  to  $L = 7$ .

Parallel Electric Fields: Quiet Day, 100s of 16mHz Current,  $m = 16$

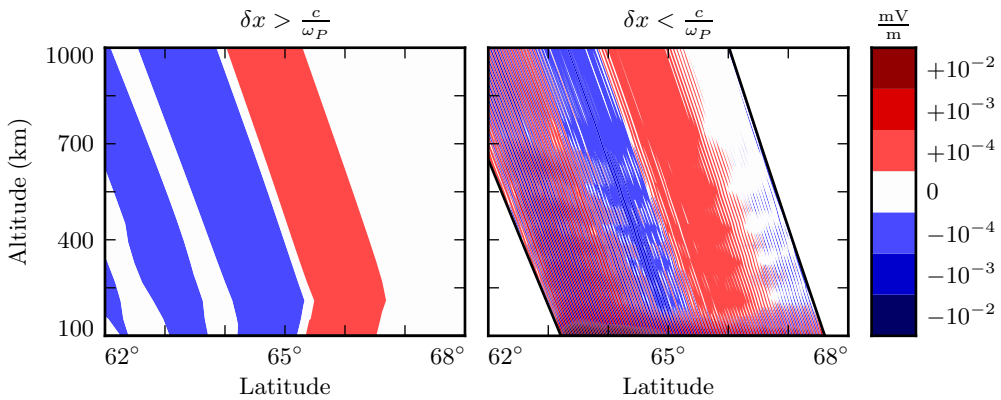


Figure 6.6: The parallel electric field develops significant structure when the perpendicular grid resolution is smaller than the electron inertial length. Unfortunately, such runs are prohibitively expensive. The subplot on the right — which still fails to resolve wave structure properly — represents a 100-fold increase in computational time compared to that on the left.

946 Even so, the run presents a significant computational expense. Spread over 16 cores,  
 947 a 100 s run on Tuna’s usual grid takes well under an hour. The inertial-scale run  
 948 barely finished in 96 hours, the cutoff at the Minnesota Supercomputing Institute. This  
 949 is because runtime goes as the inverse square of grid resolution; not only does finer

resolution require more grid cells, but it also gives rise to proportionally smaller crossing times, imposing a smaller time step.

The snapshot shown in Figure 6.6 uses a perpendicular grid resolution of 0.7 km at the Earthward edge, which just satisfies the Nyquist rate for the minimum inertial length of 1.7 km. It’s still too coarse. There is clearly some small-scale structure developing in the ionosphere, but it’s not well resolved. The large number of “wiggles” portends an imminent crash.

## 6.4 Discussion

The present chapter is a proof of concept: the addition of electron inertial effects to Tuna presents a promising first-principles-based approach to the investigation of parallel currents and electric fields associated with field line resonances. Electric fields arise which are consistent in magnitude with those predicted by the dispersion relation, and parallel currents fall within an order of magnitude or so of observed values, even when inertial length scales are not properly resolved.

Results in Section 6.2 suggest a disparity between low- $m$  poloidal and toroidal FLRs in terms of the parallel current response. At low altitude, where the two modes are directly coupled by the Hall conductivity, both seem to be accompanied by parallel currents. However, in regions of low Hall conductivity, parallel currents appear to preferentially accompany toroidal waves. This is likely a result of the toroidal mode’s sharp gradients across  $L$ -shells.

Future work could consider the relationship between the dynamic height-integrated potentials and the accompanying parallel currents, specifically with respect to the Knight relation[50]. Inertial effects could also be accompanied by test particles, in order to gauge the precipitation that would be expected to accompany global Alfvénic potential structures.

Unfortunately, simulations are prone to instability when inertial length scales are not properly resolved. And, at least at present, resolving those scales poses a prohibitive computational expense. For this reason, the consideration of inertial effects is limited to

978 the present chapter; results in Chapter 7 make use of the core version of Tuna presented  
979 in Chapter 5, which does not include the effects of electron inertia.

980 Notably, the addition or omission of parallel currents and electric fields does not appear  
981 to significantly alter the behavior of perpendicular electric fields or magnetic fields.  
982 Because the parallel electric fields are relatively small,  $\nabla \times \underline{E}$  is essentially unaffected  
983 by their inclusion. Joule dissipation from parallel currents also does not seem to be a  
984 significant in comparison to that from Pedersen and Hall currents.

985 **Chapter 7**

986 **Numerical Results**

987 A primary motivation for the development of Tuna is the fact that FLRs vary in inter-  
988 esting ways as a function of azimuthal modenumber, and that existing numerical models  
989 are limited in their ability to examine such behaviors. The present chapter discusses  
990 the core results that the model has so far produced.

991 **7.1 Modenumber and Compression**

992 It's well known that the poloidal FLR mode is compressional at low modenumber, but  
993 guided at high modenumber. However, the relationship is not well quantified. Theoreti-  
994 cal work has historically been concerned with the limits  $m \rightarrow 0$  and  $m \rightarrow \infty$ [14, 76], and  
995 only a handful of satellite observations have explicitly considered an event's azimuthal  
996 modenumber[17, 68, 88]. Using results from Tuna, the present section examines the  
997 strength of the poloidal wave's compressional component at an ensemble of finite mod-  
998 enumbers.

999 Figures 7.1 and 7.2 show magnetic field snapshots taken from a pair of runs; the first  
1000 uses a small azimuthal modenumber, and the second uses a large one. The runs are  
1001 otherwise identical: both simulations use the quiet dayside ionospheric profile, and both  
1002 are driven at 22 mHz.

1003 The differences between the two runs are striking. At low modenumber, wave activity  
1004 is visible throughout the simulation domain. Structure in the poloidal magnetic field is  
1005 only vaguely governed by the dipole geometry, and the compressional magnetic field is  
1006 comparably strong to the two perpendicular components.

1007 In contrast, at high modenumber, the poloidal magnetic field is localized to  $L \sim 5$ , where  
1008 the driving is delivered. The compressional field is weaker than the poloidal field by  
1009 at least an order of magnitude. A third-harmonic poloidal mode is visible at the outer  
1010 boundary — its magnitude is just barely large enough to be visible on the logarithmic  
1011 scale. The gap between  $L \sim 5$  (where 22 mHz matches a first-harmonic FLR) and  
1012  $L \sim 10$  (where 22 mHz matches a third-harmonic FLR) speaks to the evanescence of  
1013 non-guided waves above the compressional Alfvén cutoff frequency<sup>1</sup>.

1014 In both the low- $m$  and high- $m$  runs, toroidal activity is more or less coincident with  
1015 poloidal activity — as is to be expected, since the driving is purely poloidal, and so  
1016 the poloidal mode must be the source of the toroidal mode. It is further notable that  
1017 the toroidal mode is sharply guided. Particularly in Figure 7.2, strong, narrow, toroidal  
1018 FLRs of opposite phase can be seen oscillating very close to one another. Strong poloidal  
1019 waves, in contrast, are smeared in  $L$ .

1020 Snapshots are not shown for runs carried out using the other ionospheric profiles (active  
1021 day, quiet night, and active night). The morphology of their waves is qualitatively  
1022 similar. The differences between the profiles is considered in Sections 7.2 to 7.4.

1023 Figure 7.3 quantifies the compressional component of the poloidal mode as a function of  
1024 modenumber. Each subplot corresponds to a different run of Tuna; the runs shown in  
1025 Figures 7.1 and 7.2 are in the rightmost column, second from the top and second from the  
1026 bottom respectively. The red line indicates the ratio between the RMS compressional  
1027 magnetic field and the RMS poloidal magnetic field; both averages are taken over the  
1028 entire simulation “volume” each time step. Mean values are shown in black.

1029 At  $m = 1$ , the compressional and poloidal magnetic fields are comparable in magnitude.  
1030 As  $m$  increases, however, the compressional component quickly falls off. The compressional  
1031 component is half the strength of the poloidal component at  $m \sim 5$ , and a quarter

---

<sup>1</sup>See Section 4.4.

1032 by  $m \sim 10$ . Similar behavior is seen using the active dayside and active nightside pro-  
1033 files (not shown). On the quiet nightside (not shown), the compressional component of  
1034 the poloidal mode does not fall off quite as sharply;  $\left| \frac{B_z}{B_x} \right|$  falls to 50 % at  $m \sim 8$  and to  
1035 25 % at  $m \sim 16$ .

1036 A slight frequency dependence is apparent across each row in Figure 7.3. Compressional  
1037 coupling falls off slower for waves at higher frequency. This is because higher-frequency  
1038 waves are that much closer to the cutoff frequency, and so their propagation across  
1039  $L$ -shells is that much less evanescent.

1040 Notably, the waves considered in the present work are fundamental harmonics. The  
1041 compressional behavior of the poloidal mode may vary for the (more-common) second  
1042 harmonic: Radoski suggests that the asymptotic value of  $\left| \frac{B_z}{B_x} \right|$  is inversely proportional  
1043 to the harmonic number[76].

Magnetic Field Snapshots: Quiet Day , 22mHz Current,  $m = 2$

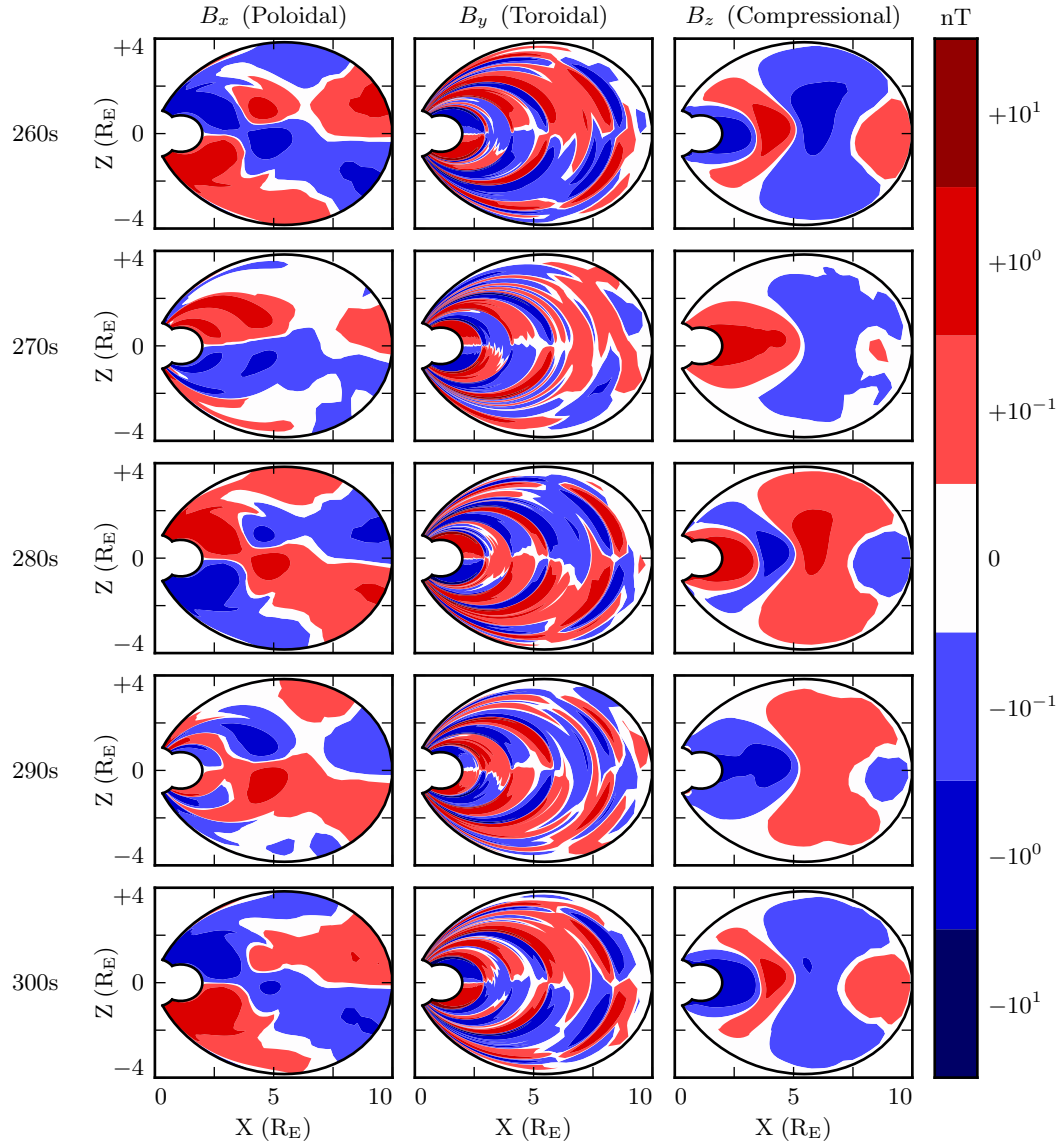


Figure 7.1: Each row in the above figure is a snapshot in time. The three columns show the simulated poloidal, toroidal, and compressional magnetic fields. Due to the run's low azimuthal modenumber, the poloidal mode has a significant compressional component. This is visible both in the fact that  $B_z$  is comparable in size to  $B_x$ , and in that structure in  $B_x$  is only vaguely guided by the geometry of the magnetic field. Toroidal waves, in contrast, are sharply guided.

Magnetic Field Snapshots: Quiet Day , 22mHz Current,  $m = 32$

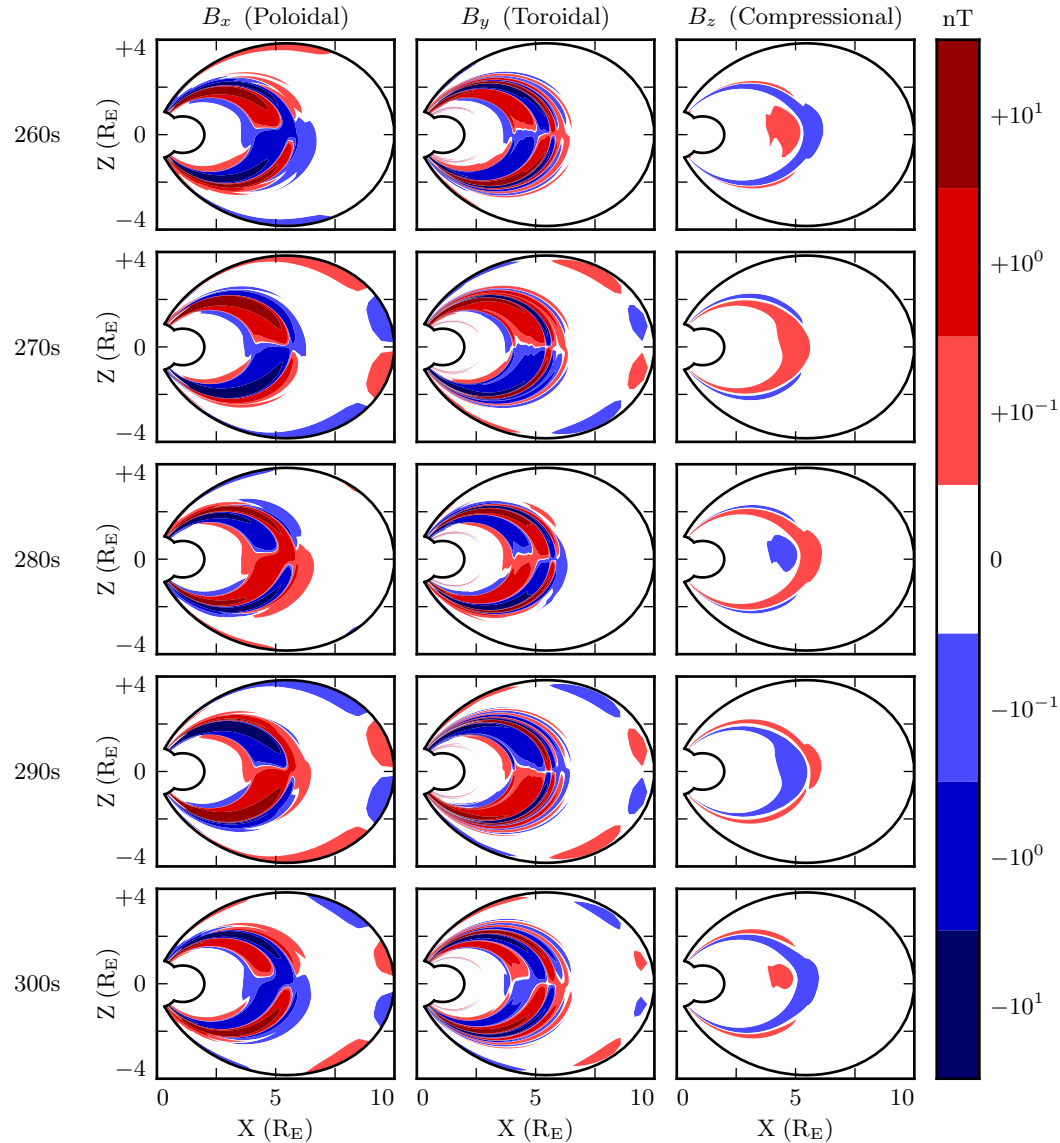


Figure 7.2: The above figure is analogous to Figure 7.1, but the run uses a large azimuthal modenumber. The change has a dramatic effect. The poloidal wave is concentrated much more sharply in  $L$ , and its compressional component is weaker by an order of magnitude. Regardless of modenumber, toroidal waves exist at a range of  $L$  shells similar to poloidal waves, and show sharp definition across  $L$ -shells.

### Compressional Coupling to the Poloidal Mode: Quiet Day

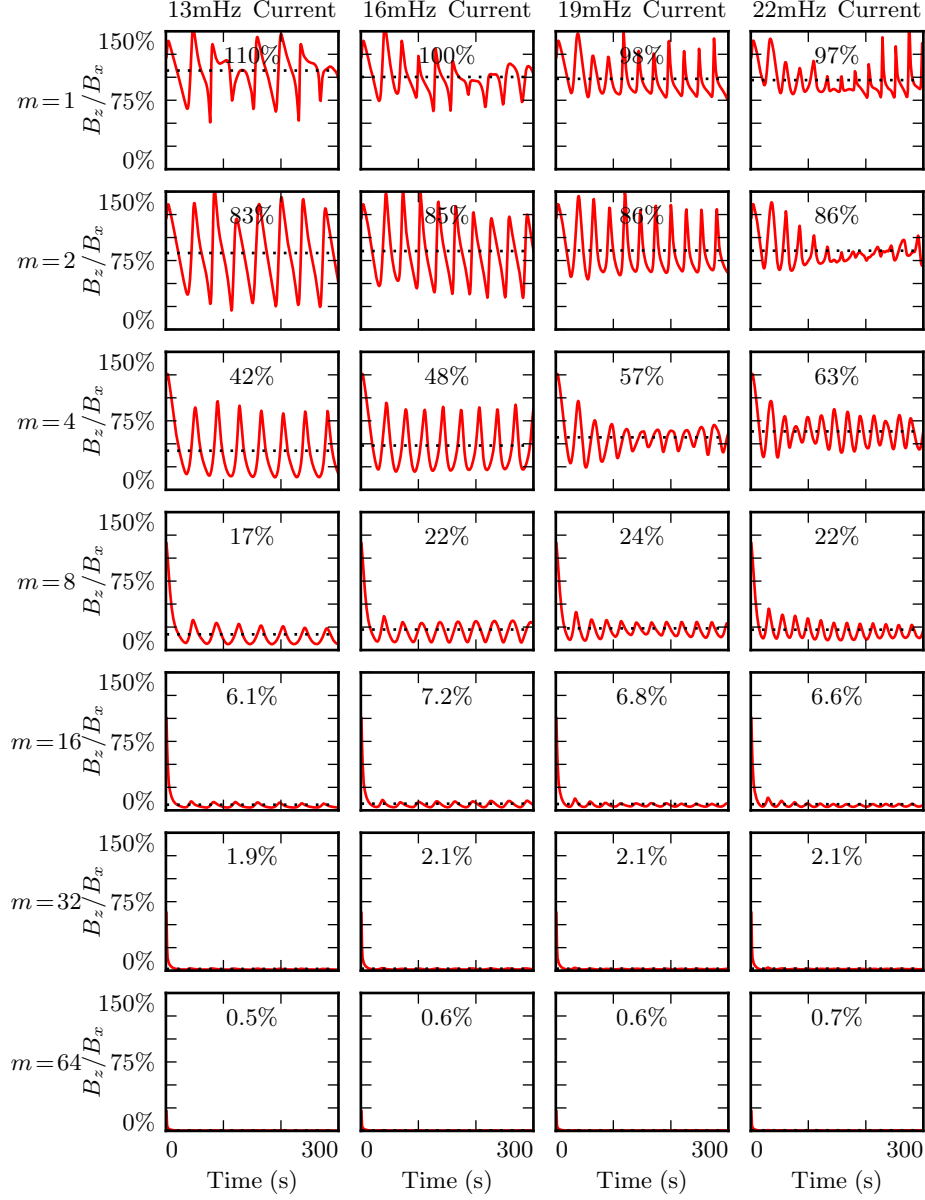


Figure 7.3: Each subplot above corresponds to a different run; the runs shown in Figures 7.1 and 7.2 are in the rightmost column, second from the top and second from the bottom respectively. Red lines indicate the ratio between the RMS compressional and poloidal magnetic fields. Mean values are shown in black. The compressional field is comparable to the poloidal field at  $m = 1$ , but falls quickly.

## 1044 7.2 Resonance and Rotation on the Dayside

1045 In his 1974 paper, Radoski argues that a poloidally-polarized wave should asymptotically  
1046 rotate to the toroidal polarization[76] as a result of the curved derivative in the  
1047 meridional plane. The question of finite poloidal lifetimes is considered further in a  
1048 1995 paper by Mann and Wright[64], using a straightened field line and an Alfvén speed  
1049 gradient in the “radial” direction. They also found a rotation over time from poloidal to  
1050 toroidal polarization, with the characteristic time proportional to the azimuthal mode-  
1051 number.

1052 The present section builds on the aforementioned results by relaxing several of their non-  
1053 physical assumptions. Tuna’s geometry is more realistic than Radoski’s half-cylinder or  
1054 the box model used by Mann and Wright. Previous work has considered the evolution  
1055 of an initial condition, while the simulations shown below include driving delivered  
1056 over time. In addition, Tuna features a finite, height-resolved ionospheric conductivity  
1057 profile, rather than the perfectly-reflecting boundaries used in the past.

Each subplot in Figure 7.4 is analogous to Figure 3 in Mann and Wright’s paper[64]. Blue lines show the total energy in the poloidal mode as a function of time. Red lines show toroidal energy. Runs are organized analogous to those in Figure 7.3: drive frequency is constant down each column, and azimuthal modenum is constant across each row. Axis bounds are held constant across all subplots. The poloidal and toroidal energy are computed by integrating over the electromagnetic energy density, per Poynting’s theorem:

$$U_P = \int \frac{dV}{2\mu_0} \left( B_x^2 + \frac{1}{v_A^2} E_y^2 \right) \quad U_T = \int \frac{dV}{2\mu_0} \left( B_y^2 + \frac{1}{v_A^2} E_x^2 \right) \quad (7.1)$$

1058 Where the differential volume  $dV$  is computed using the Jacobian<sup>2</sup> to account for Tuna’s  
1059 unusual geometry. The integral is evaluated in  $u^1$  and  $u^3$  but not  $u^2$  (Tuna’s missing  
1060 half-dimension), which gives energy in units of gigajoule per radian. More than anything  
1061 else, this serves as a reminder that Pc4 pulsations are localized in MLT.

---

<sup>2</sup>See Section 5.1.

1062 The 28 runs shown in Figure 7.4 use an ionospheric profile corresponding to the dayside  
1063 during times of low solar activity, where the conductivity is relatively high. The active  
1064 and quiet dayside profiles are briefly contrasted in Section 7.4; for the most part, the  
1065 focus of the present work is on the difference between the dayside and the nightside  
1066 (Section 7.3). Differences between the two dayside profiles are small in comparison.

1067 The fact that red (toroidal) lines appear at all in Figure 7.4 speaks to a net rotation  
1068 of energy from the poloidal mode to the toroidal. As discussed in Section 5.3, Tuna's  
1069 driving is delivered purely into the poloidal electric field, reflecting a perturbation in  
1070 the magnitude of the ring current.

1071 As expected, the rotation from poloidal to toroidal is slowest at large azimuthal mode-  
1072 numbers. The toroidal energy overtakes the poloidal energy within a single drive period  
1073 at small  $m$ ; at  $m = 64$ , the most of the energy is in the poloidal mode for  $\sim 10$  peri-  
1074 ods. However, the relationship between azimuthal modenumber and rotation timescale  
1075 is not linear, as was suggested by Mann and Wright. Instead, in a practical setting, the  
1076 rotation is fastest at  $m \sim 4$ .

1077 This is explained by the compressional character of the poloidal mode. At very low  
1078 modenumber, energy in the poloidal mode moves readily across  $L$ -shells. A significant  
1079 fraction of that energy is lost to the outer boundary before rotating to the toroidal  
1080 mode. At high modenumber, compressional propagation is evanescent, so all energy  
1081 in the poloidal mode must ultimately rotate to the toroidal mode or be lost to Joule  
1082 dissipation.

1083 Joule dissipation is a major player in the system's energy economy. However, due to the  
1084 highly conductive dayside ionosphere, dissipation timescales are in the tens of Pc4 wave  
1085 periods. Energy loss through Joule dissipation asymptotically balances energy input  
1086 from driving, but most of that energy is not lost until after it has rotated from the  
1087 poloidal mode to the toroidal. As such, in most runs shown in Figure 7.4, the energy  
1088 content of the toroidal mode asymptotically exceeds that of the poloidal mode.

1089 The asymptotic energy content of the system also depends on how well the drive fre-  
1090 quency matches the local eigenfrequency. If the two do not match, energy is lost to  
1091 destructive interference between the standing wave and the driving.

1092 In principle, energy moves between the poloidal and toroidal modes due to their direct  
1093 coupling through the ionospheric Hall conductivity. In practice, this effect does not  
1094 move large amounts of energy. When the runs shown in Figure 7.4 are repeated with  
1095 the Hall conductivity set to zero, the resulting energy curves are not visibly different  
1096 (not shown).

1097 The low- $m$  runs at 19 mHz merit additional discussion. These runs accumulate energy  
1098 over a large number of wave periods, while the low- $m$  waves at 13 mHz, 16 mHz, and  
1099 22 mHz do not. This effect is likely nonphysical. At 19 mHz, a third-harmonic resonance  
1100 forms very close to the outer boundary, and is likely enhanced by nonphysical reflections  
1101 against the simulation boundary.

1102 The presence of individual harmonics can be seen in the contours shown in Figures 7.5  
1103 and 7.6. These figures show the same runs as Figure 7.4, arranged in the same way on  
1104 the page. However, instead of showing the total energy integrated over the simulation  
1105 domain, the energy densities are averaged over the volume of each flux tube individually.  
1106 Figure 7.5 shows contours of poloidal energy density and Figure 7.6 shows toroidal  
1107 energy density.

1108 The top few rows of Figure 7.5 confirm that the poloidal mode's compressional nature is  
1109 to blame for its failure to accumulate energy at low modenumber. Waves move so readily  
1110 across field lines that no visible amount of energy builds up at  $L \sim 5$ , the location of the  
1111 driving. Some energy moves inward, and is trapped by the peak in Alfvén speed just  
1112 inside the plasmapause, while the rest moves to the outer boundary. The time spent  
1113 moving across field lines counts against the poloidal mode's finite lifetime, inhibiting  
1114 the buildup of poloidal energy density even at  $L$ -shells where the wave matches the local  
1115 eigenfrequency.

1116 As  $m$  increases, the energy distribution becomes more concentrated in  $L$ , though indi-  
1117 vidual features remain fairly broad. At  $m = 8$ , runs at 13 mHz and 16 mHz are inclined  
1118 to build up energy just inside the plasmapause, while those at 19 mHz and 22 mHz res-  
1119 onate just outside the plasmapause; in all four cases, the energy is spread over a range  
1120 of at least 1 in  $L$ .

1121 The peak energy density in the bottom-right run (22 mHz driving,  $m = 64$ ) is by far the  
1122 largest of any run in Figure 7.5. The azimuthal modenumber is large, so the poloidal  
1123 mode is purely guided; energy is not smeared across multiple  $L$ -shells. And, crucially, the  
1124 frequency of the driving matches closely with the Alfvén frequency at  $L \sim 5$ . Other runs  
1125 on the bottom row are also guided, but they reach lower asymptotic energy densities  
1126 because of a mismatch between the drive frequency and the local eigenfrequency —  
1127 resulting in destructive interference between the standing wave and its driver.

1128 Giant pulsations are typically seen at  $\sim 10$  mHz, well below the 22 mHz poloidal peak  
1129 shown in Figure 7.5. Part of the discrepancy is likely due to the position of the driving.  
1130 Pgs are most common at latitudes of  $\sim 66^\circ$ , which maps out to  $L \sim 6$ , whereas these  
1131 runs are driven at  $L \sim 5$ . The size of the plasmapause also has a significant effect.  
1132 When the runs in Figure 7.5 are repeated with the plasmapause at  $L = 5$  instead of  
1133  $L = 4$ , the strongest resonance (driven at  $L \sim 5$ ) drops from 22 mHz to 16 mHz (not  
1134 shown).

1135 Whereas the poloidal contours are smeared over a swath of  $L$ -shells (though the high- $m$   
1136 runs less so), the toroidal contours in Figure 7.6 appear only where the wave frequency  
1137 matches the local eigenfrequency. A horizontal line drawn through the Alfvén speed  
1138 frequency profiles (recall Figure 3.1) intersects the profile up to three times: once as  
1139 the Alfvén frequency drops through the Pc4 range from its low-latitude peak, again as  
1140 the Alfvén frequency rises sharply at the plasmapause, and a third time as the Alfvén  
1141 frequency drops asymptotically. Toroidal waves can be seen resonating at all three of  
1142 these locations in the  $m = 4$ , 22 mHz run in Figure 7.6, along with a third harmonic at  
1143 large  $L$ . This is consistent with observations: toroidal resonances are noted for having  
1144 frequencies which depend strongly on  $L$ , in contrast to the poloidal mode's less-strict  
1145 relationship between frequency and location.

1146 In only one of the runs shown in Figure 7.5 does the poloidal mode attain an energy  
1147 density on the order of  $10^{-1}$  nJ/m<sup>3</sup>. On the other hand, the toroidal mode reaches  
1148  $\sim 10^{-1}$  nJ/m<sup>3</sup> in six of the runs in Figure 7.6. That is, the poloidal mode only exhibits  
1149 a high energy density on the dayside only when conditions are ideal; the toroidal mode  
1150 isn't nearly so particular.

Poloidal (Blue) and Toroidal (Red) Energy: Quiet Day

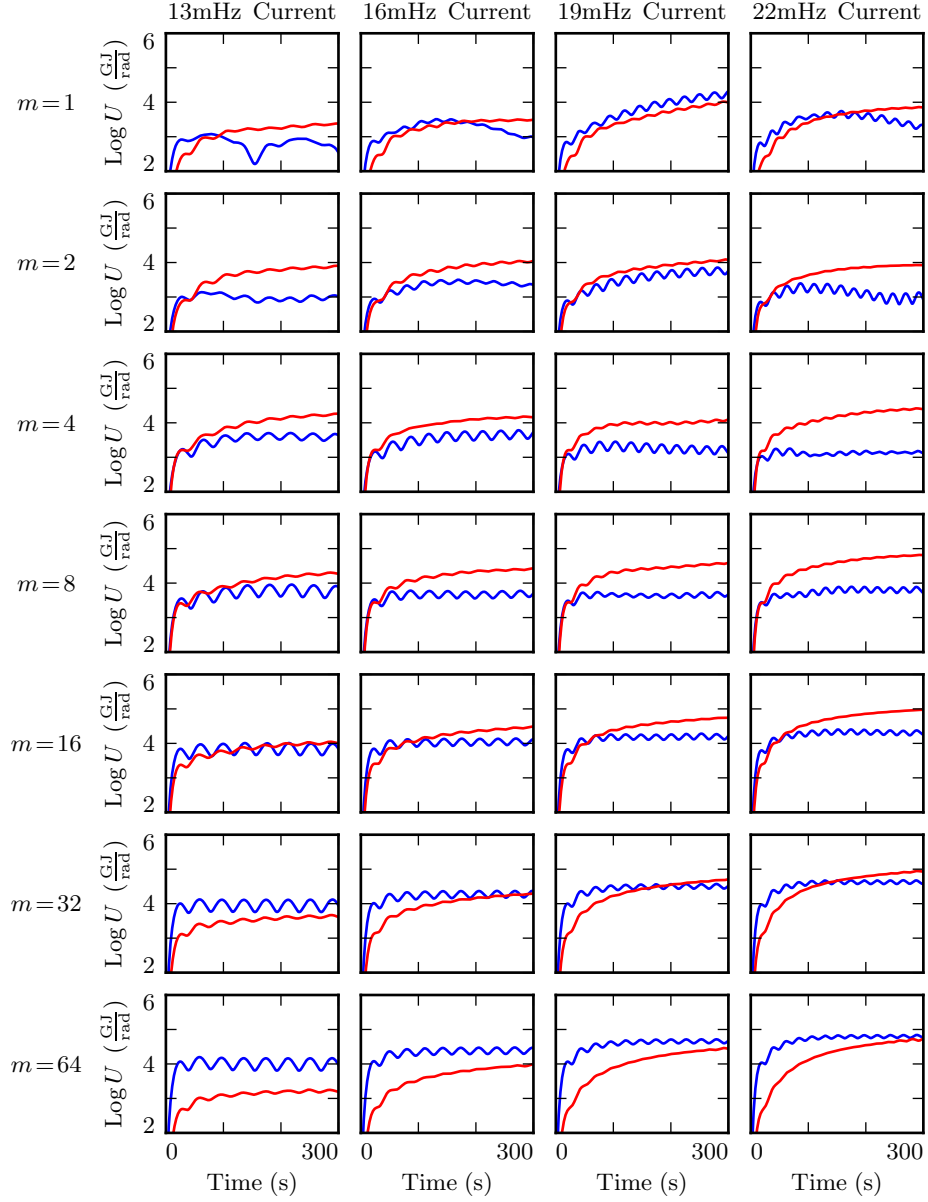


Figure 7.4: Each subplot above shows the poloidal (blue) and toroidal (red) energy for a simulation as a function of time. Each row contains four simulations, each with the same azimuthal modenumber; the seven rows in each column share a drive frequency. Driving is purely poloidal, but energy rotates asymptotically to the toroidal mode, and rotation is slowest at high modenumber.

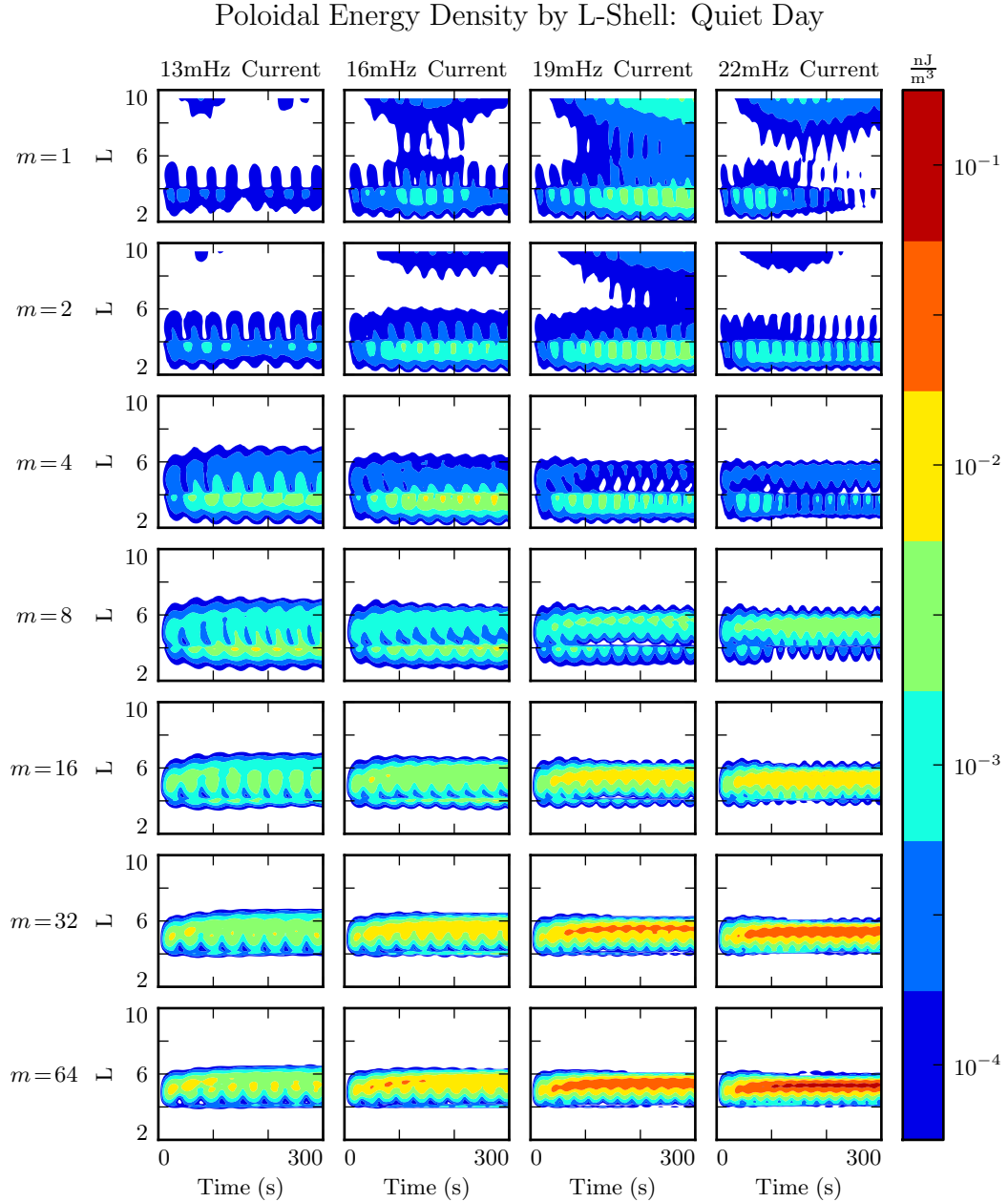


Figure 7.5: At low modenumber (top rows), the compressional nature of the poloidal mode allows energy to escape the simulation. At high modenumber (lower rows), the poloidal mode is guided; energy is trapped at the  $L$ -shell where it's injected, and rotation to the toroidal mode is slow — ideal conditions for resonance. But energy buildup is lackluster except where the drive frequency matches the local eigenfrequency (best in the rightmost row).

### Toroidal Energy Density by L-Shell: Quiet Day

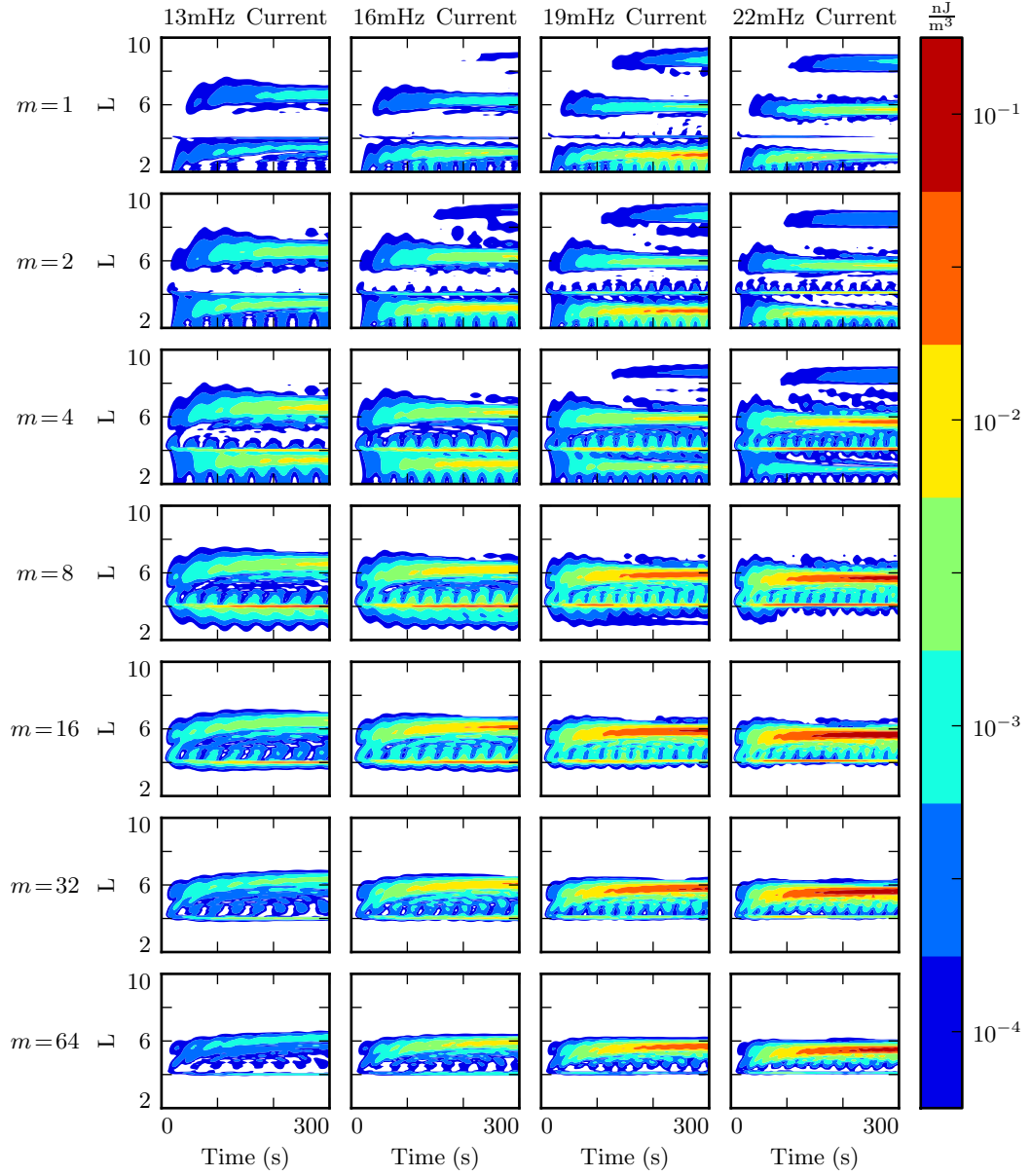


Figure 7.6: Whereas the poloidal mode is smeared in  $L$  due to its compressional nature, the toroidal mode is focused at  $L$  shells where it's resonant. In general, when the conductivity is high, the toroidal mode also exhibits a higher asymptotic energy density than the poloidal mode (Figure 7.5).

## 1151 7.3 Resonance and Rotation on the Nightside

- 1152 Compared to the dayside ionosphere employed in Section 7.2, conductivity on the night-  
1153 side is much lower. Runs in the present section use Tuna’s ionospheric profile corre-  
1154 sponding to the nightside during quiet solar conditions. The two nightside profiles are  
1155 briefly compared in Section 7.4, but for the most part the present work is concerned  
1156 with the behavior of the nightside compared to that on the dayside.
- 1157 Other than the change in ionospheric profile, Figures 7.7 to 7.9 are analogous to Fig-  
1158 ures 7.4 to 7.6. Each subplot corresponds to a different 300s run of Tuna. Drive  
1159 frequency is constant down each column, and azimuthal modenumber is constant across  
1160 each row.
- 1161 The low conductivity on the nightside gives rise to strong Joule dissipation. Waves are  
1162 damped out in just a few bounces, so asymptotic energy values are reached quickly.  
1163 No combination of frequency and modenumber gives rise to the accumulation of energy  
1164 over multiple drive periods.
- 1165 As on the dayside, rotation of energy from the poloidal to toroidal mode is fastest at  
1166  $m \sim 4$ . Unlike the dayside, however, dissipation on the nightside is fast compared to  
1167 the rotation of energy to the toroidal mode. Toroidal energy does not asymptotically  
1168 exceed the poloidal energy by a significant margin in any run shown in Figure 7.7. At  
1169  $m = 64$ , where the rotation timescale is slowest, no more than 10% of the energy in the  
1170 poloidal mode rotates to the toroidal mode before being lost.
- 1171 Also similar to the dayside, low- $m$  runs driven at 19 mHz and 22 mHz resonate very  
1172 close to the outer boundary. As before, the buildup of energy is likely nonphysical.
- 1173 Poloidal contours on the nightside (Figure 7.8) are weaker than those on the dayside,  
1174 and build up energy over less time, but otherwise similar. At low modenumber, poloidal  
1175 energy propagates across  $L$ -shells, preventing the significant accumulation of energy  
1176 anywhere. As the modenumber increases, energy is contained near the driving at  $L \sim 5$ .  
1177 The strongest response is seen at 13 mHz on the bottom row, where the modenumber is  
1178 at its largest and the frequency matches closest with the local eigenfrequency. Even in

1179 that case, dissipation timescales are comparable to the oscillation period, so the wave  
1180 only persists in the presence of continuous driving.

1181 Toroidal energy contours on the nightside exhibit significantly different behavior from  
1182 those on the dayside.

1183 At low modenumber, the nightside toroidal mode (Figure 7.9) contains less energy  
1184 than on the dayside, but it still shows some preference for sharp resonances where the  
1185 drive frequency matches the local Alfvén frequency. At moderate modenumbers, as on  
1186 the dayside, the toroidal mode is more or less comparable in strength to its poloidal  
1187 counterpart. It's only at high modenumber that the difference between the dayside  
1188 and nightside toroidal contours become truly dramatic. Whereas on the dayside, most  
1189 energy is asymptotically deposited in the toroidal mode, on the nightside most poloidal  
1190 energy is dissipated faster than the poloidal-to-toroidal rotation timescale. At  $m = 64$ ,  
1191 where the poloidal mode is at its strongest, the toroidal mode is at its weakest; it barely  
1192 registers, even on Figure 7.9's log scale.

Poloidal (Blue) and Toroidal (Red) Energy: Quiet Night

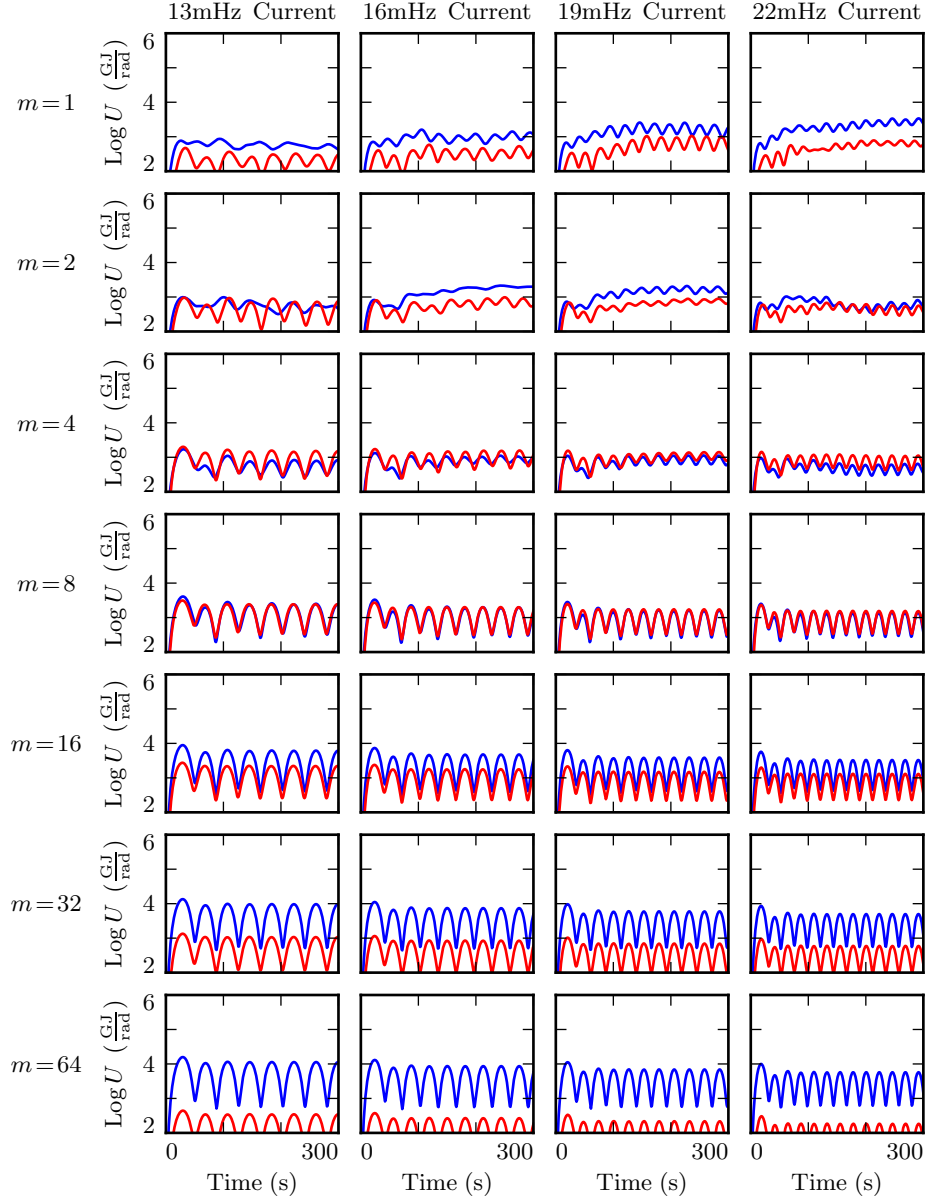


Figure 7.7: The energy content of each FLR on the nightside resembles that of a damped, driven oscillator. Energy is periodically added to the system, but most is lost too fast to rotate to the toroidal mode, particularly at high modenumber. There is no significant buildup of energy over multiple periods. Runs at  $m = 1$  (top row) are an apparent exception, likely due to a nonphysical interaction with the boundary.

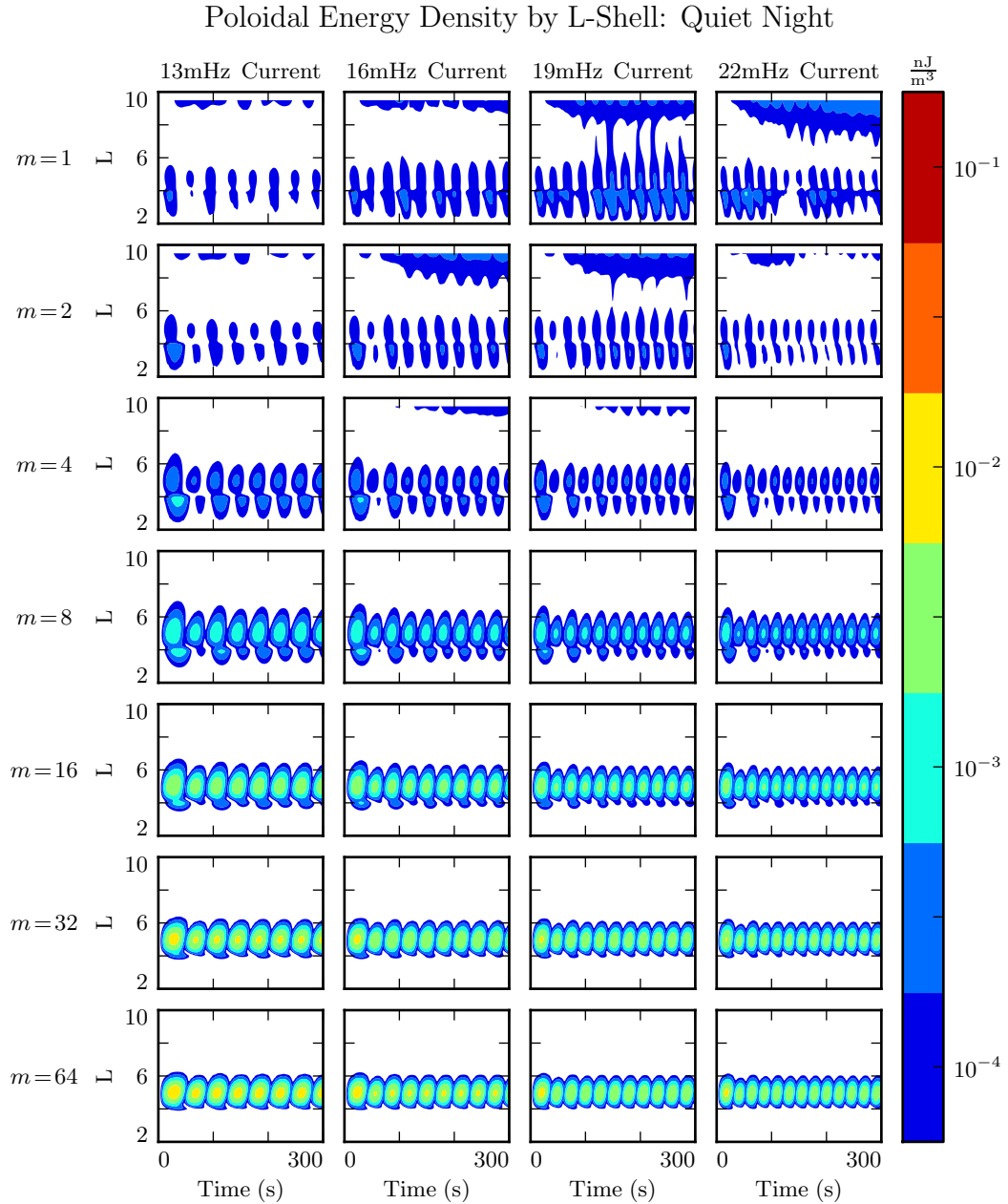


Figure 7.8: As on the dayside (Figure 7.5), low-modenumber poloidal waves (top rows) readily propagate across  $L$ -shells and escape the simulation domain. Energy density builds up most effectively at high modenumbers, where the poloidal mode is guided, and poloidal-to-toroidal rotation is slow. Even in this case, however, dissipation is fast enough to prevent energy from accumulating over multiple drive periods.

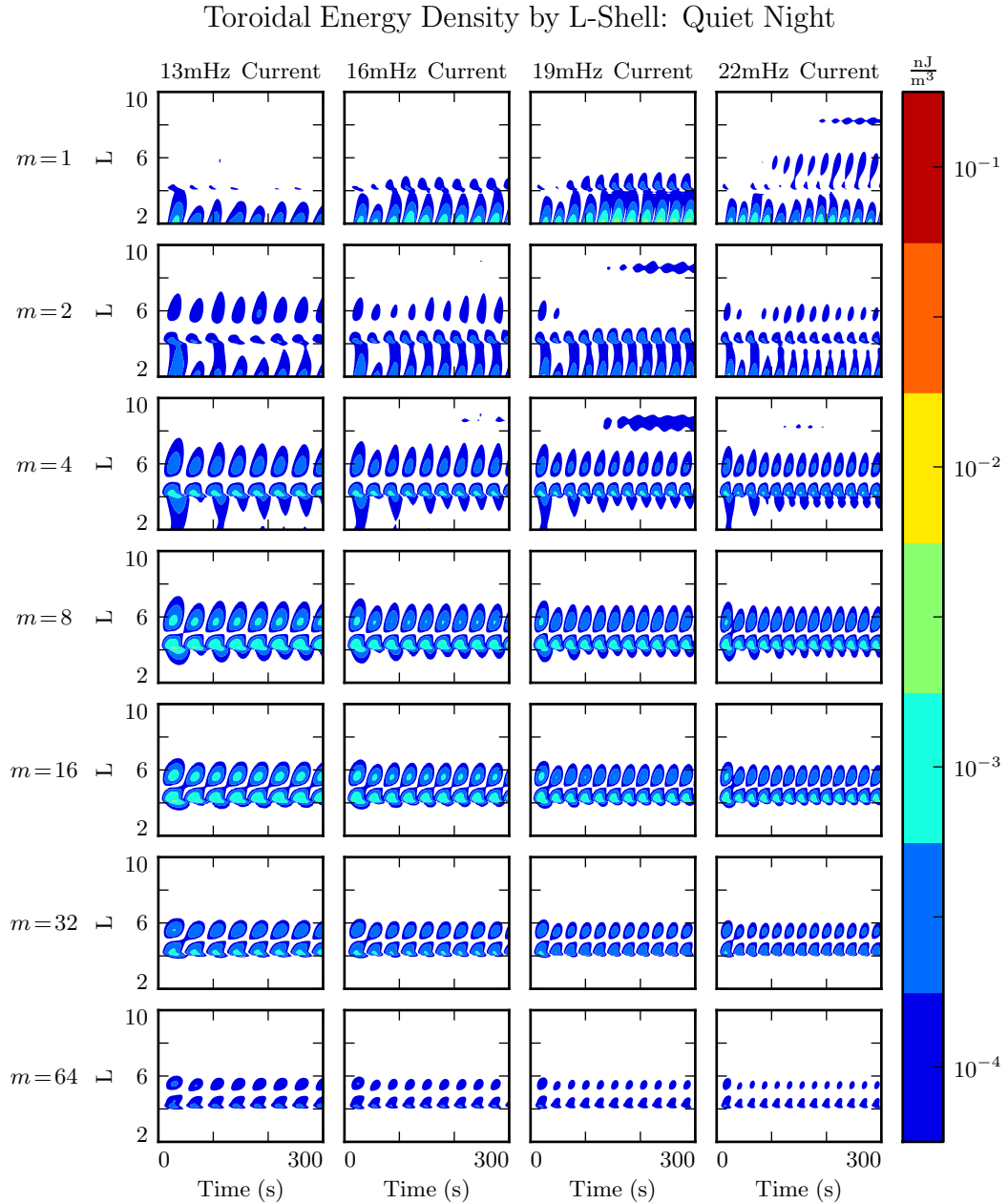


Figure 7.9: On the dayside (Figure 7.6), most energy rotates asymptotically to the toroidal mode. On the night side, the same is not true, since the poloidal mode quickly loses energy to Joule dissipation. At high modenumber, where the poloidal-to-toroidal rotation timescale is in the tens of wave periods, almost all of the energy is dissipated from the poloidal mode rather than rotating to the toroidal mode.

## 1193 7.4 Ground Signatures and Giant Pulsations

1194 While the majority of the action is in space, the majority of FLR observations have  
1195 historically been ground-based. The present section explores simulations (including  
1196 those discussed in Sections 7.2 and 7.3) in terms of their ground signatures rather than  
1197 their integrated energy distributions.

1198 Figures 7.10 and 7.11 show fourteen runs each, two per row. Contours give magnetic  
1199 fields at the ground, plotted against time on the horizontal axis and latitude on the  
1200 vertical axis. Modenumber is held constant across each row, as in the above sections;  
1201 columns show north-south and east-west ground signatures using an ionospheric profile  
1202 for active (first and second columns respectively) and quiet (third and fourth columns).

1203 As noted in Chapter 3, the magnetic polarization of a low frequency Alfvén wave is  
1204 rotated by  $\sim 90^\circ$  as it passes through the ionosphere. The east-west field on the ground  
1205 ( $B_\phi$ ) corresponds to the poloidal polarization in space, and the north-south field on the  
1206 ground ( $B_\theta$ ) corresponds to the toroidal mode.

1207 The most striking feature of Figures 7.10 and 7.11 is the modenumber dependence.  
1208 As modenumber increases, the magnetic field signatures become sharply localized in  
1209 latitude. At high  $m$ , ground signatures are concentrated between  $60^\circ$  and  $70^\circ$ , peaking  
1210 near  $64^\circ$ , roughly coincident with the foot point of the  $L = 5$  field line; ionospheric  
1211 ducting is not significant in the Pc4 regime.

1212 At low modenumber, magnetic signatures are weak on the ground because the waves  
1213 in space are also weak. At high modenumber, waves in space are strong, but so is the  
1214 attenuation of magnetic signatures by the atmosphere<sup>3</sup>. The “sweet spot” at which  
1215 magnetic ground signatures are maximized falls at  $m = 16$  to  $m = 32$ .

1216 Tuna shows stronger ground signatures on the dayside than on the nightside, more or  
1217 less in proportion with the difference in magnitude in space. Energy on the dayside  
1218 (which depends on field magnitude squared) peaks an order of magnitude larger than  
1219 that on the nightside. Peak ground signatures on the dayside are larger by a factor of  
1220 four: 45 nT compared to 11 nT. On both the dayside and the nightside, peak ground

---

<sup>3</sup>See Equation (3.3).

1221 signatures are in  $B_\phi$ , the east-west magnetic field component; both peaks are also at  
1222  $m = 16$ , and both are seen in runs using the ionospheric profile for quiet solar activity.

1223 It's further notable that the ground signatures — particularly those on the nightside  
1224 — exhibit a change in chirality based on latitude. At low latitude,  $B_\theta$  leads  $B_\phi$ , which  
1225 creates a counterclockwise signature on the ground (in the northern hemisphere). At  
1226 high latitude, the phase is reversed, resulting in a clockwise ground signature.

1227 These results match well with the properties associated with Pgs: east-west polarization,  
1228 latitude-dependent chirality, peak latitude of  $\sim 66^\circ$ , and azimuthal modenumber  
1229 of 16 to 35. Just about the only properties missing are the azimuthal drift (which is  
1230 beyond the scope of the present model) and the distribution in MLT. Pgs are most  
1231 commonly observed pre-dawn, but morning and evening ionospheric profiles are not  
1232 presently implemented for Tuna.

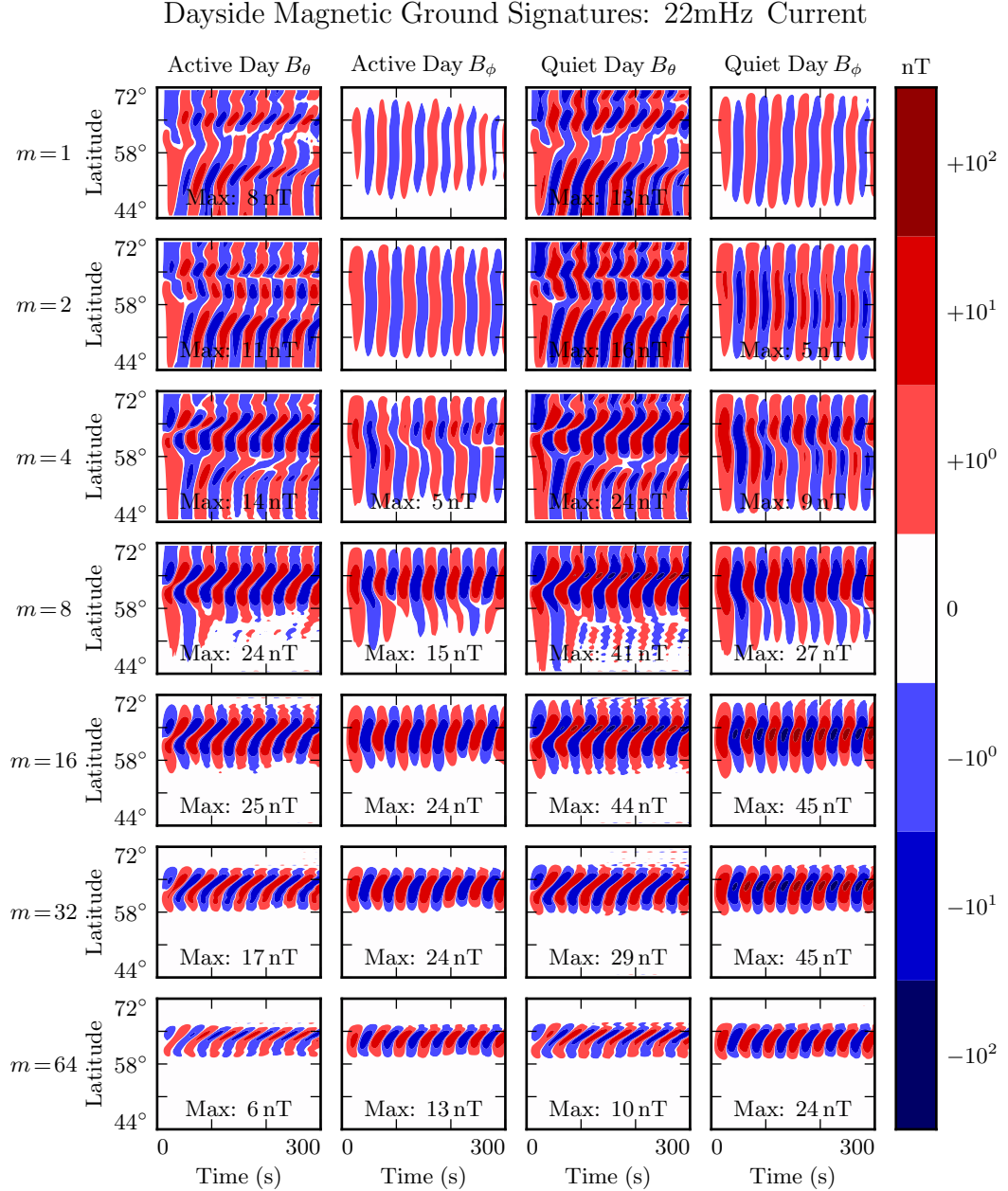


Figure 7.10: The magnetic ground signatures are shown for fourteen runs, two per row. Azimuthal modenumber is constant across each row. Polarization and ionospheric profile vary by column, per the headers. Ground signatures at low modenumber are weak because the waves in space are weak, while those at high modenumber are attenuated by the atmosphere. Considering both effects, ground signatures seem to be maximized at  $m = 16$  to  $m = 32$ . Peak amplitudes above 3 nT are marked.

### Nightside Magnetic Ground Signatures: 13mHz Current

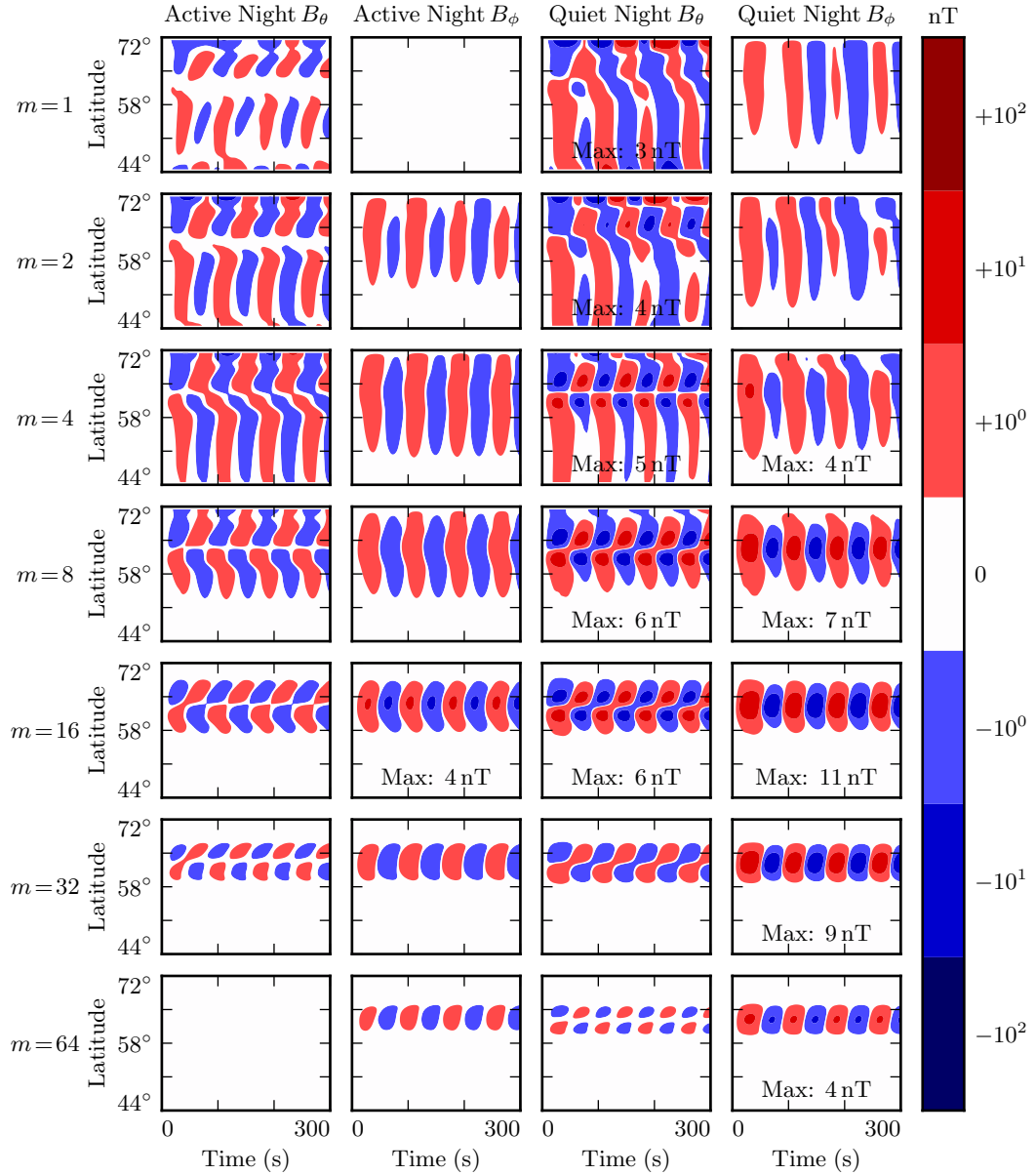


Figure 7.11: Nightside ground signatures are less strongly peaked than those on the dayside, but qualitative features are the same: the strongest signals are in  $B_\phi$ , peaked over just a few degrees in latitude, at a modenumber of 16 or 32, under quiet ionospheric conditions.

1233 **7.5 Discussion**

1234 The above results show agreement with a number of past FLR studies. In addition,  
1235 several novel connections are suggested between known properties of FLRs.

1236 The compressibility of poloidal FLRs at low modenumber, but not high modenumber,  
1237 is reproduced and quantified. At  $m \sim 1$ , the poloidal and compressional components of  
1238 an FLR in the  $Pc4$  range are comparable in magnitude. At  $m \gtrsim 6$ ,  $\left| \frac{B_z}{B_x} \right| \lesssim \frac{1}{2}$ , and at  
1239  $m \gtrsim 12$ ,  $\left| \frac{B_z}{B_x} \right| \lesssim \frac{1}{4}$ .

1240 The present results also suggest that compressional character of poloidal  $Pc4$ s is to blame  
1241 for the weak relationship between  $L$  and frequency, compared to that seen in toroidal  
1242 events. Toroidal resonances are defined sharply in  $L$  regardless of modenumber, while  
1243 poloidal resonances are smeared in  $L$  — particularly at low  $m$ , but to some degree at  
1244 high  $m$  as well.

1245 The asymptotic rotation of energy from the poloidal mode to the toroidal mode is  
1246 reproduced; at small  $m$ , the rotation timescale is comparable to a wave period, while at  
1247 large modenumber it's on the order of 10 periods. On the dayside, little energy is lost  
1248 to Joule dissipation on rotation timescales. In contrast, on the nightside, dissipation  
1249 timescales are comparable to wave periods. In high- $m$  nightside runs, even in the case  
1250 of continuous driving near the local eigenfrequency, the movement of energy from the  
1251 poloidal mode to the toroidal mode is vanishingly small.

1252 Ground signatures at low modenumber are shown to be weak because waves in space are  
1253 weak; this is particularly true for poloidal waves — a non-guided wave can't very well  
1254 resonate along a field line — but also true of toroidal waves insomuch as poloidal waves  
1255 are their source. FLRs resonate most strongly at high  $m$ , but high- $m$  signatures are  
1256 also attenuated by the atmosphere. The balance between the two effects falls around  $m$   
1257 of 16 to 32. It's further suggested that a high- $m$  driver will cause a weak resonance in  
1258 place rather than tunneling across field lines to a matching eigenfrequency, and that the  
1259 same driving should give rise to stronger ground signatures during times of low solar  
1260 activity, on both the dayside and the nightside.

1261 The findings together suggest, awkwardly, that the morphology of giant pulsations re-  
1262 veals relatively little about their origins.

1263 One can consider a hypothetical magnetosphere subject to constant driving: broadband  
1264 in frequency, broadband in modenumber, just outside the plasmapause. Low- $m$  poloidal  
1265 waves will quickly rotate to the toroidal mode (and/or propagate away). High- $m$  waves  
1266 will resonate in place, accumulating energy over time, and giving rise to “multiharmonic  
1267 toroidal waves”[87]; Fourier components that do not match the local eigenfrequency  
1268 will quickly asymptote. Waves with very high modenumbers will be attenuated by  
1269 the ionosphere. The response on the ground will be counterclockwise at low latitude,  
1270 clockwise at high latitude, peaked at  $16 \lesssim m \lesssim 32$ , mostly east-west polarized, and  
1271 notably stronger during quiet solar conditions. In other words, the measurements will  
1272 look very much like a giant pulsation.

1273 The present results offer no explanation as to the tendency of giant pulsations to drift  
1274 azimuthally, or to appear pre-dawn in MLT — though the latter is addressed by the  
1275 observational results in Chapter 8.

<sub>1276</sub> **Chapter 8**

<sub>1277</sub> **Van Allen Probe Observations**

<sub>1278</sub> The results presented in Chapter 7 are interesting on their own, but become particularly  
<sub>1279</sub> valuable when combined with observational data. Unfortunately, only a small number  
<sub>1280</sub> of studies to date have explored how Pc4 observation rate is affected by the harmonic  
<sub>1281</sub> and polarization structure of those waves. While Pc4 pulsations have previously been  
<sub>1282</sub> studied in terms of both harmonic[4, 14, 26, 43, 81, 90] and polarization[2, 16, 17, 52, 56],  
<sub>1283</sub> no past survey has characterized each event in terms of both properties.

<sub>1284</sub> This has largely been due to observational constraints. The classification of a wave's  
<sub>1285</sub> harmonic is best carried out by computing the phase offset of the magnetic and electric  
<sub>1286</sub> field waveforms, simultaneous in situ measurements of which have only recently become  
<sub>1287</sub> available since the launch of THEMIS[3] in 2007 and the Van Allen Probes[84] in 2012.  
<sub>1288</sub> The Van Allen Probes are particularly well-suited to the study of Pc4 pulsations as  
<sub>1289</sub> their apogee of  $L \sim 6$  coincides closely with eigenfrequencies in the Pc4 range.

<sub>1290</sub> The present chapter uses data from the Van Allen Probes mission to survey the oc-  
<sub>1291</sub> currence rate of FLRs in the Pc4 range as a function of parity and polarization, as  
<sub>1292</sub> well as magnitude, frequency, and phase. The tools used to perform the present anal-  
<sub>1293</sub> ysis — SPEDAS and the SPICE kernel — are publicly available. They, along with  
<sub>1294</sub> the Python routines used to download, filter, and plot the data, can be found at  
<sub>1295</sub> <https://github.com/UMN-Space-Physics>.

1296 TODO: Set up Git repo.

## 1297 8.1 Sampling Bias and Event Selection

1298 The present analysis makes use of Van Allen Probe data from October 2012 to August  
1299 2015 — the entire range available at the time of writing. Between the two probes, that's  
1300 just over 2000 days of observation.

1301 For the purposes of Pc4 pulsations, it's reasonable to consider the two probes to be  
1302 independent observers. Nearly all Pc4 events occur near apogee ( $L \gtrsim 5$ ), at which  
1303 point the two probes are several hours apart in MLT. Pc4 events are typically not large  
1304 enough to be seen by both probes simultaneously, and not long enough in duration to  
1305 be seen by two probes passing through the same region of space several hours apart.

1306 Electric and magnetic field waveforms are collected using the probes' EFW[100] and  
1307 EMFISIS instruments respectively. Values are cleaned up by averaging over the ten-  
1308 second spin period. Three-dimensional electric field data is then obtained using the  
1309  $\underline{E} \cdot \underline{B} = 0$  assumption. Notably, this assumption is taken only when the probe's spin  
1310 plane is offset from the magnetic field by at least  $15^\circ$ . The rest of the data — about  
1311 half — is discarded, which introduces a sampling bias against the flanks.

1312 A further bias is introduced by the probes' non-integer number of precessions around  
1313 Earth. As of July 2014, apogee had precessed once around Earth[16]. The present work  
1314 considers roughly one and a half precessions; the nightside has been sampled at apogee  
1315 twice as often as the dayside.

1316 The spatial distribution of usable data — that is, data for which three-dimensional  
1317 electric and magnetic fields are available — is shown in Figure 8.1. Bins are unitary in  
1318  $L$  and in MLT. The distribution of the data in magnetic latitude is not shown; the Van  
1319 Allen Probes are localized to within  $\sim 10^\circ$  of the equatorial plane.

1320 Field measurements are transformed from GSE coordinates into the same dipole coordi-  
1321 nates used in Chapters 5 and 7. The  $z$  axis (parallel to the background magnetic field)  
1322 is estimated using a ten-minute running average of the magnetic field measurements.

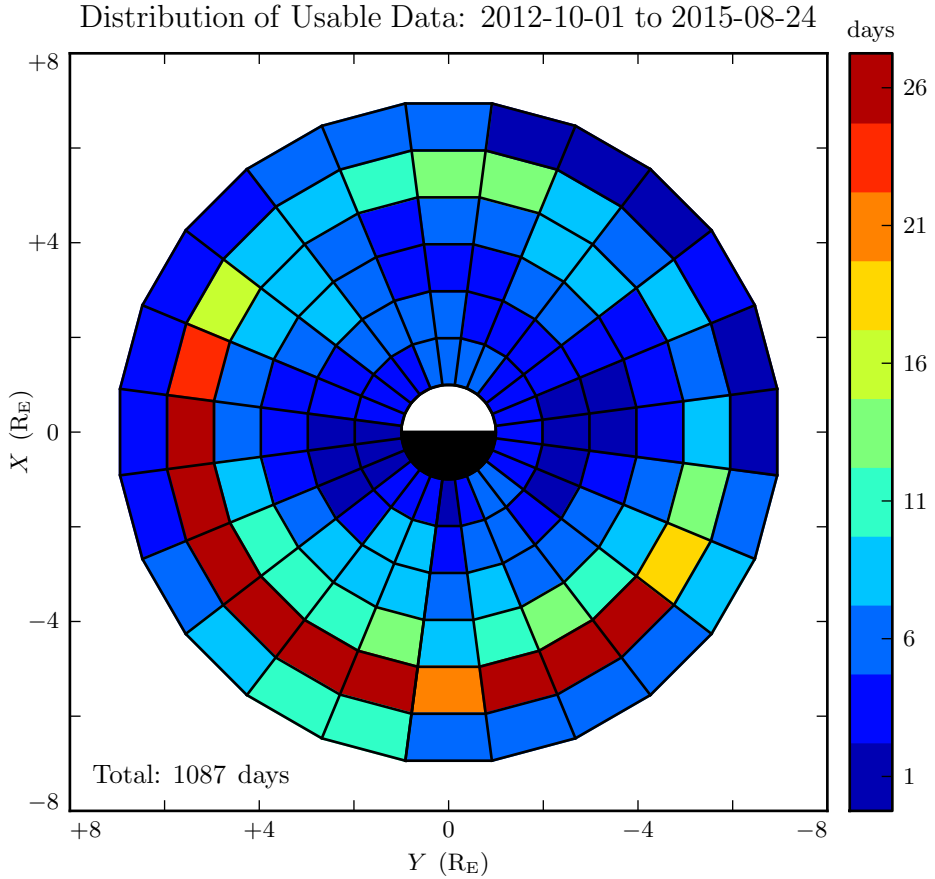


Figure 8.1: Three-dimensional electric field values are computed by assuming  $\underline{E} \cdot \underline{B} = 0$ . Data is discarded whenever the magnetic field falls within  $15^\circ$  of the spin plane, which introduces a bias against the flanks. Furthermore, the probes have completed one and a half precessions around Earth; the dayside has been sampled once at apogee, and the nightside twice.

- 1323 The  $y$  axis is set parallel to  $\hat{z} \times \underline{r}$ , where  $\underline{r}$  is the probe's geocentric position vector.
- 1324 The  $x$  axis is then defined per  $\hat{x} \equiv \hat{y} \times \hat{z}$ . This scheme guarantees that the axes are
- 1325 right-handed and pairwise orthogonal[56].
- 1326 The  $\sim 1000$  days of usable data are considered half an hour at a time, which gives a fre-
- 1327 quency resolution of  $\sim 0.5$  mHz in the discrete Fourier transform. Spectra are computed
- 1328 for all six field components:  $\tilde{B}_x$ ,  $\tilde{B}_y$ ,  $\tilde{B}_z$ ,  $\tilde{E}_x$ ,  $\tilde{E}_y$ , and  $\tilde{E}_z$ . The background magnetic

1329 field is subtracted before transforming the magnetic field components, leaving only the  
1330 perturbation along each axis<sup>1</sup>. Each waveform is also shifted vertically so that its mean  
1331 over the thirty minute event is zero.

Frequency-domain Poynting flux is computed from the electric and magnetic field transforms. A factor of  $L^3$  compensates the compression of the flux tube, so that the resulting values are effective at the ionosphere. Poloidal and toroidal Poynting flux, respectively, are given by:

$$\tilde{S}_P \equiv -\frac{L^3}{\mu_0} \tilde{E}_y \tilde{B}_x^* \quad \tilde{S}_T \equiv \frac{L^3}{\mu_0} \tilde{E}_x \tilde{B}_y^* \quad (8.1)$$

1332 The poloidal and toroidal channels are independently checked for Pc4 waves. For each  
1333 channel, a Gaussian profile is fit to the magnitude of the Poynting flux,  $|\tilde{S}(\omega)|$ . If the  
1334 fit fails to converge, or if the peak of the Gaussian does not fall within 5 mHz of the  
1335 peak value of  $\tilde{S}$ , the event is discarded. Events are also discarded if their frequencies  
1336 fall outside the Pc4 frequency range (7 mHz to 25 mHz) or if their amplitudes fall below  
1337  $10^{-2}$  mW/m<sup>2</sup> (out of consideration for instrument sensitivity).

1338 Events are discarded if their parity is ambiguous. The electric field and the magnetic  
1339 field must be coherent at a level of 0.9 or better (judged at the discrete Fourier transform  
1340 point closest to the peak of the Gaussian fit). Any event within 3° of the magnetic  
1341 equator is also not used; as discussed in Chapter 3, in order to distinguish an odd mode  
1342 from an even mode, it's necessary to know whether the observation is made north or  
1343 south of the equator.

1344 A visual inspection of events shows that those with broad “peaks” in their spectra  
1345 are typically not peaked at all — they are noisy spectra with several spectral features  
1346 grouped just closely enough to trick the fitting routine. A threshold is set at a FWHM  
1347 of 3 mHz (equally, a standard deviation of 1.27 mHz). Any event with a Gaussian fit  
1348 broader than that is discarded.

1349 Notably, events are not filtered on their phase — that is, on the division of their energy  
1350 between standing and traveling waves. This is the topic of Section 8.5.

---

<sup>1</sup>As in Chapters 4 to 7,  $B_x$ , refers not to the full magnetic field in the  $x$  direction, but to the perturbation in the  $x$  direction from the zeroth-order magnetic field. The same is true for  $B_y$  and  $B_z$ .

## 1351 8.2 Events by Mode

1352 The filters described in Section 8.1 yield 762 Pc4 events, the spatial distribution of  
1353 which is shown in Figure 8.2. In each bin, the event count is normalized to the amount  
1354 of usable data (Figure 8.1). Bins shown in white contain zero events. The rate in the  
1355 bottom corner is an overall mean; it's an estimate of how often Pc4 events would be  
1356 observed if the sampling were distributed uniformly in space.

1357 Consistent with previous work, Pc4 events peak on the dayside and are rarely observed  
1358 at  $L < 4$ . Nearly 30 % of the usable data shown in Figure 8.1 is taken at  $L < 4$ , yet  
1359 only 16 of the 762 events (2 %) appear there.

1360 On the other hand, the present work runs contrary to Dai's 2015 result in terms of Pc4  
1361 event rates with respect to the plasmapause (not shown). His analysis found (poloidal)  
1362 Pc4 pulsations to be comparably common inside and outside the plasmapause[16]. In  
1363 the present work, only 40 of the 762 events (5 %) fall inside the plasmasphere, despite  
1364 the fact that 40 % of the available data falls within the plasmasphere. The disparity is  
1365 not likely due to a difference in sampling — Dai's work, like the present work, uses data  
1366 from the Van Allen Probes mission. Rather, the difference is likely due to a difference  
1367 in how the plasmapause is defined. Dai identifies the plasmapause by the maximum  
1368 gradient in electron number density, while the present work takes an electron density of  
1369  $100 \text{ /cm}^3$  to mark the plasmapause<sup>2</sup>.

1370 The same events in Figure 8.2 are shown again in Figure 8.3, partitioned by polarization  
1371 and parity.

1372 The distribution of even poloidal events in Figure 8.3 is consistent with that reported  
1373 by Dai[16]: the observation rate is peaked at noon, and smeared across the dusk side.  
1374 Notably, Dai's work focused on even poloidal waves. While he did not explicitly remove  
1375 odd events from his sample, he did introduce a threshold in the magnetic field. This  
1376 threshold is preferentially satisfied by even waves (which have a magnetic field antinode  
1377 near the equator) compared to odd waves (which have a magnetic field node). Dai

---

<sup>2</sup>Per ongoing work by Thaller.

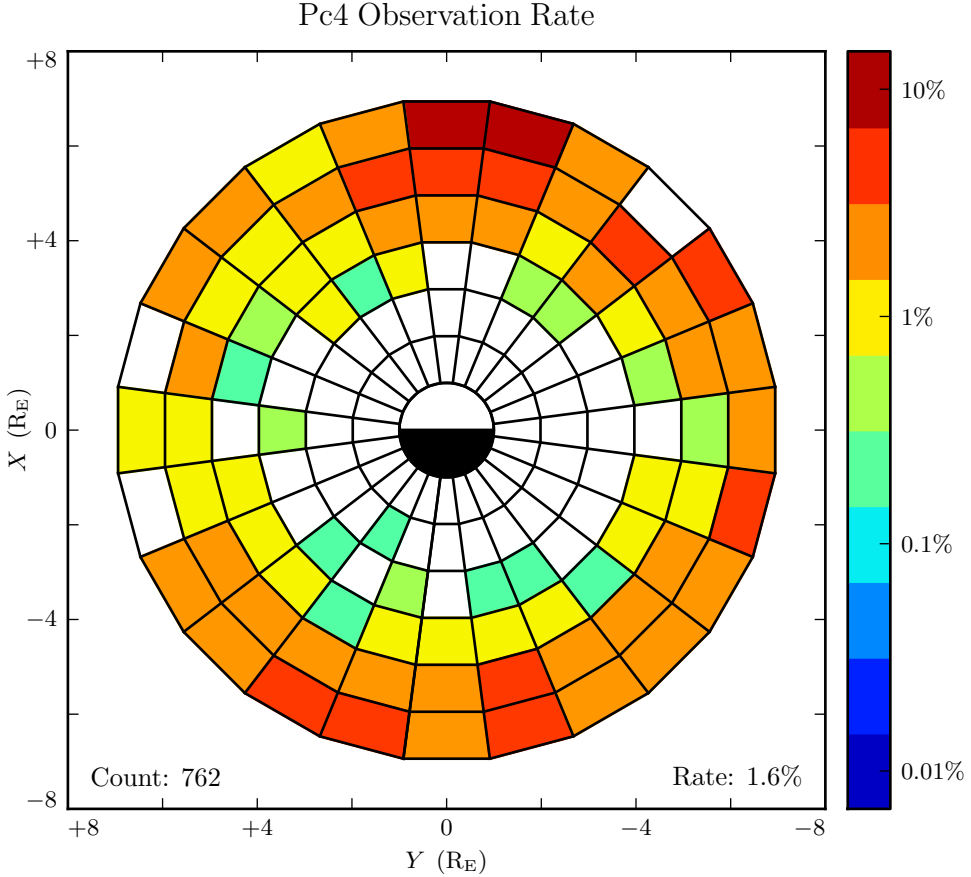


Figure 8.2: The above figure shows the spatial distribution of all 762 observed Pc4 events. Counts are normalized by the amount of usable data in each bin. The value in the bottom-right corner is the mean of the rate in each bin, with the rate in each bin weighed by the area of that bin. Events where the poloidal and toroidal channel both trigger ( $\sim 10\%$  of events) are counted as only a single event. Bins shown in white contain zero events.

1378 characterized the parity of only a quarter of his events; among those, he found even  
 1379 harmonics to outnumber odd harmonics ten-to-one.

1380 In fact — to the degree that they can be straightforwardly compared — the distributions  
 1381 in Figure 8.3 also show agreement with work by Anderson[2] (using AMPTE/CCE),  
 1382 Kokubun[52] (using ATS6), Liu[56] (using THEMIS), and Motoba[68] (using GOES).  
 1383 Toroidal events dominate overall, and are primarily seen on the morning side. Poloidal

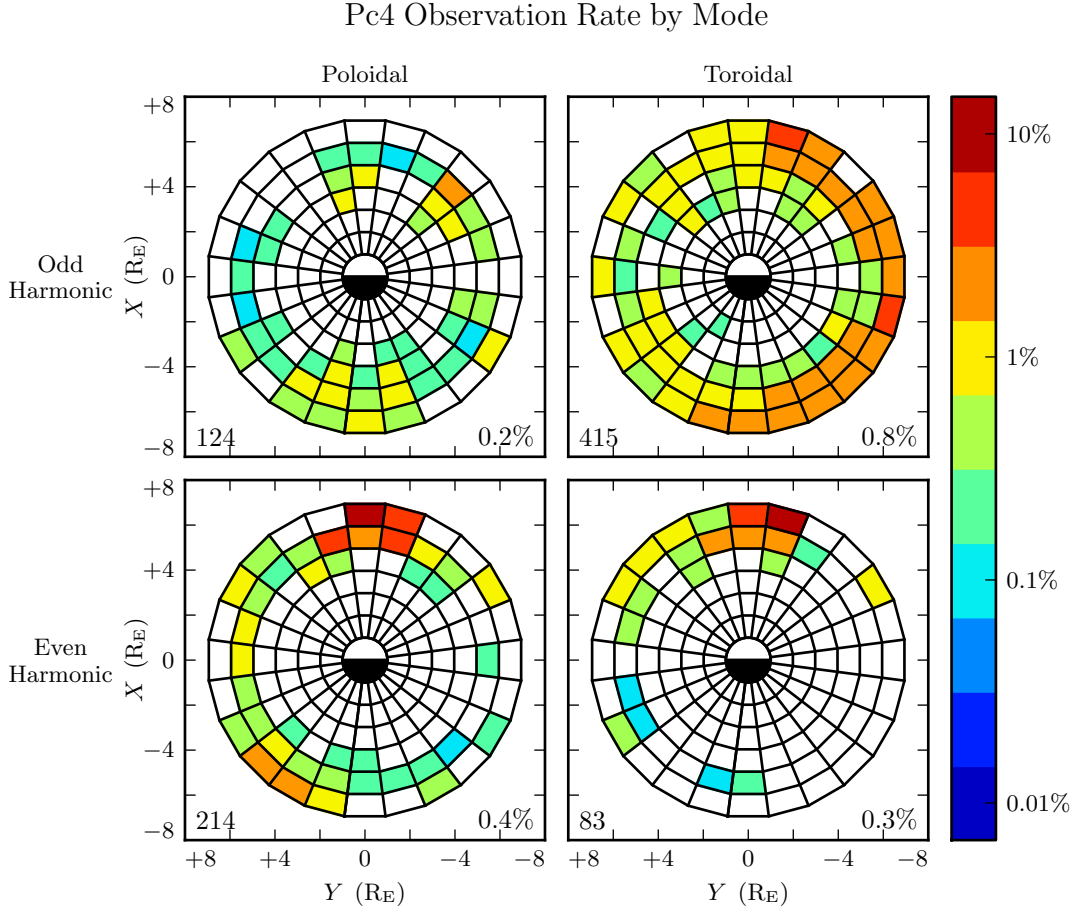


Figure 8.3: The above figure shows the spatial distribution for the same 762 events shown in Figure 8.2, partitioned by polarization and parity. The selection criteria described in Section 8.1 ensure that both properties are known for all events. Event counts are normalized by the time spent by the amount of usable data in each bin. Counts shown in the bottom-left corners do not sum to 762 because some events trigger on both the poloidal channel and the toroidal channel.

- <sup>1384</sup> events are spread broadly in MLT, with a peak near noon and odd harmonics in the
- <sup>1385</sup> early morning.
- <sup>1386</sup> Crucially, the present work can offer insight into how previous results fit together. Unlike
- <sup>1387</sup> events considered in previous works, those shown in Figure 8.3 have all been categorized

1388 in terms of both polarization and parity. And, crucially, the selection process has not  
1389 introduced a bias with respect to polarization or parity (at least not an obvious one).

1390 The even events shown in Figure 8.3 show good agreement with the numerical results in  
1391 Chapter 7. The even poloidal and even toroidal distributions are qualitatively similar,  
1392 as might be expected if even poloidal waves served as a source for even toroidal waves.  
1393 Even poloidal waves are more prevalent, suggesting a typical event duration comparable  
1394 to the poloidal-to-toroidal rotation timescale. And even toroidal events are skewed  
1395 dayward compared to even poloidal events, suggesting that poloidal-to-toroidal rotation  
1396 is inhibited by increased Joule dissipation on the nightside.

1397 The same can be said to some extent for the odd events in Figure 8.3, though the trends  
1398 are less strong. Odd poloidal and odd toroidal events are both scarce on the dusk flank.  
1399 On the dawn flank, poloidal events skew nightward, while toroidal events are spread  
1400 broadly — that is, they are skewed dayward compared to the poloidal events. However,  
1401 it's unclear why odd toroidal events outnumber odd poloidal events to such a degree.

1402 When the 762 events are broken down by mode in Figure 8.3, the result is 124 odd  
1403 poloidal events, 214 even poloidal events, 415 odd toroidal events, and 83 even toroidal  
1404 events — a total of 836 events. The total is greater than 762 because in  $\sim 10\%$  of  
1405 events, the poloidal and toroidal channels trigger independently. Such cases are marked  
1406 as a single event in Figure 8.2, but the toroidal and poloidal events are both shown in  
1407 Figure 8.3.

1408 Double-triggering can be taken as a vague proxy for event quality. When the channels  
1409 both trigger independently, the two events almost always (71 of 74 events) exhibit the  
1410 same parity. This suggests a poloidal wave with sufficient power, and a sufficient narrow  
1411 spectral peak, that it can still be seen after much of its energy has rotated to the toroidal  
1412 mode.

1413 The spatial distribution of double events is shown in Figure 8.4. The left column shows  
1414 events observed with  $DST \geq -30$  nT, normalized by the amount of usable data at  
1415  $DST \geq -30$  nT. The right column shows events at  $DST < -30$  nT, normalized by the  
1416 amount of data with  $DST < -30$  nT.

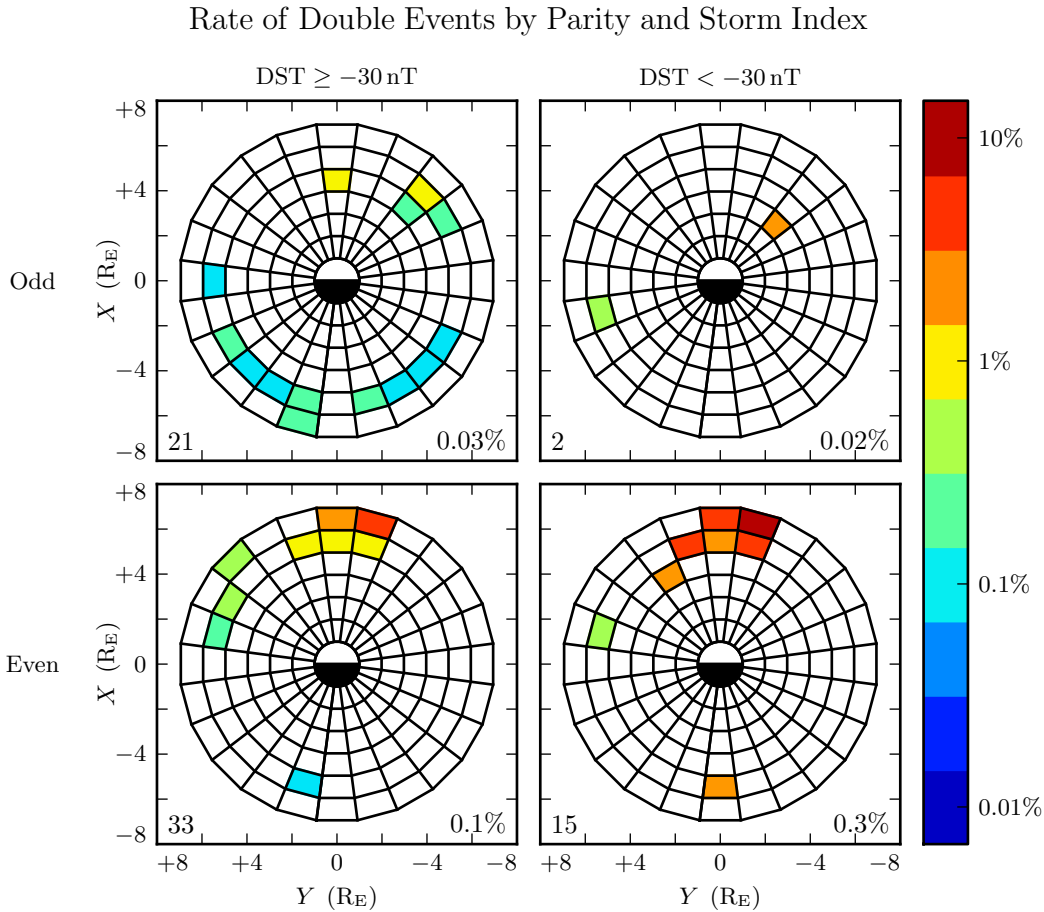


Figure 8.4: A double event is a simultaneous triggering of the poloidal and toroidal channels on the same probe. In such cases, the two channels almost always exhibit the same parity. Double events serve as a vague proxy for event quality — a poloidal event with sufficient strength and clarity to be seen even after much of its energy has rotated to the toroidal mode. Odd double events are spread broadly; even events are concentrated near noon, and become more common during geomagnetically active times.

<sup>1417</sup> Odd double-triggering events are spread broadly in MLT. They rarely occur twice on  
<sup>1418</sup> the same day; the 23 events shown take place over 20 different dates. Odd double events  
<sup>1419</sup> occur at similar rates regardless of DST.

<sup>1420</sup> Even-harmonic double-triggering events, on the other hand, are mostly seen near noon,  
<sup>1421</sup> and are significantly more common during geomagnetically active times. Even events

1422 are also more concentrated than odd ones. The 48 even-harmonic double-events shown  
1423 in the bottom row of Figure 8.4 are spread over 20 days, and 35 of them are spread over  
1424 just 7 days. This clustering — where the poloidal and toroidal channel both trigger for  
1425 five to ten half-hour events in the same day — is prevalent regardless of DST.

### 1426 8.3 Events by Amplitude

1427 One might reasonable be concerned that the spatial distributions presented in Figure 8.3  
1428 are dominated by these small events, while Pc4 events large enough to be noteworthy  
1429 follow a different distribution entirely.

1430 The distribution of event magnitudes is presented in Figure 8.5, graded based on the  
1431 peak of the Gaussian fit of each event’s Poynting flux,  $|\tilde{S}(\omega)|$ . Mean and median  
1432 values are listed for each mode. Most events are small, with Poynting flux well below  
1433  $0.1 \text{ mW/m}^2$  when mapped to the ionosphere. Only a handful of events — 3 out of 762  
1434 — exceed  $1 \text{ mW/m}^2$ , typically taken to be the threshold at which visible auroral arcs  
1435 form.

1436 Perhaps the most notable feature of Figure 8.5 is the relative uniformity of the distri-  
1437 bution of even poloidal events. If a higher magnitude threshold is imposed, as shown in  
1438 Figure 8.6, the proportion of even poloidal events rises.

1439 The spatial bins in Figure 8.6 are larger than those in Section 8.2; this change reflects  
1440 an effort to keep the number of events large compared to the number of bins, even when  
1441 considering relatively small subsets of the data. The larger bins — two hours wide in  
1442 MLT and divided at  $L = 5$  radially — are also used in Sections 8.4 and 8.5. All of the  
1443 large-binned bullseye plots also share a common logarithmic color bar.

1444 All else being equal, one might expect the amplitude distribution of even toroidal events  
1445 to mimic that of even poloidal events, since poloidal waves asymptotically rotate to  
1446 toroidal waves. However, this does not seem to be the case. The mean and median  
1447 magnitudes are more or less consistent for even toroidal events, odd toroidal events,  
1448 and odd poloidal events, while even poloidal events are twice as large by those metrics.  
1449 This would seem to imply that large even poloidal modes have disproportionately high

### Amplitude Distribution of Pc4 Events by Mode

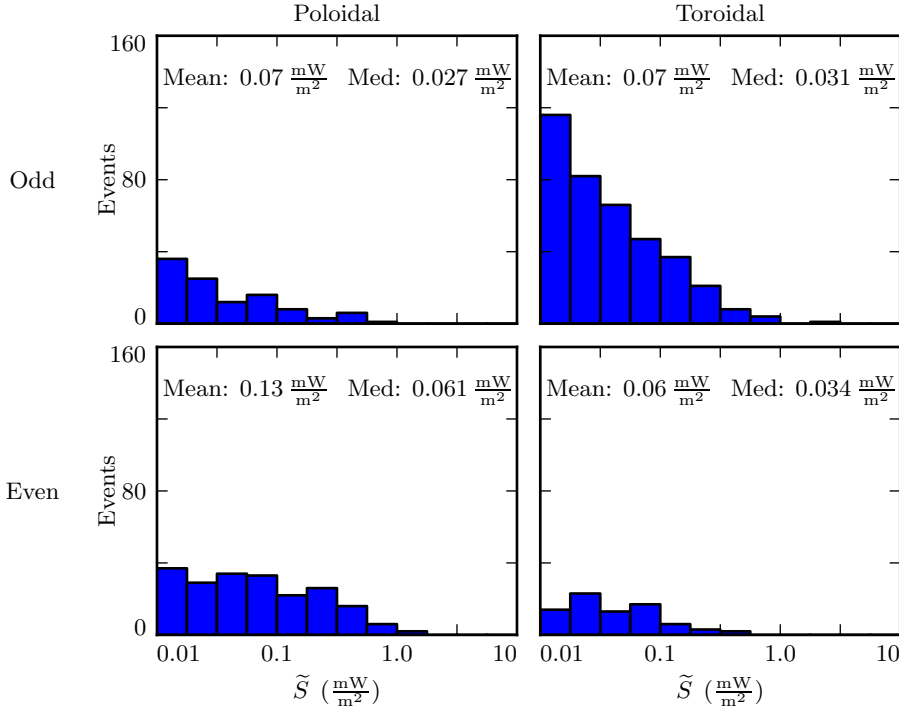


Figure 8.5: Amplitude distribution is shown for Pc4 events by parity and polarization, based on the peak of the spectrum's Gaussian fit. Odd poloidal events, odd toroidal events, and even toroidal events fall off sharply with increasing amplitude, while the even poloidal events are distributed more broadly — the mean and median of the even poloidal distribution are twice as large as those of the others.

modenumbers, and thus deliver energy to the toroidal mode less efficiently. This explanation is unsatisfying, however; Figure 8.6 shows that even poloidal and toroidal modes both become more concentrated near noon at high amplitude, suggesting a common origin.

### Distribution of Pc4 Events by Mode and Amplitude

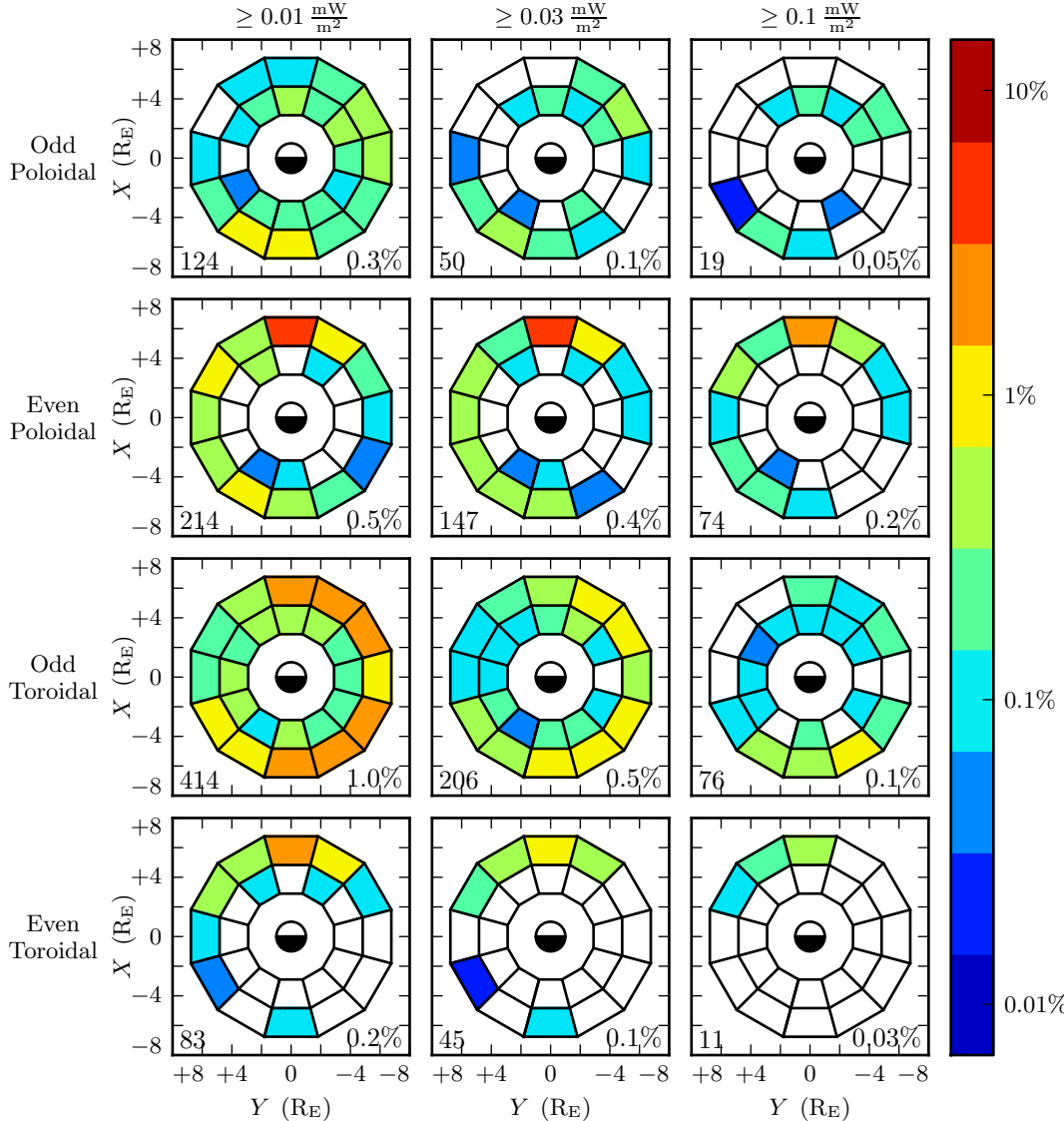


Figure 8.6: The above figure shows the distribution of Pc4 event observations by mode. Event magnitude cutoff is constant down each column, and increases from left to right. Stronger even events appear to become more concentrated on the dayside as the amplitude increases. Even poloidal events also become significantly more numerous relative to the other three modes, from 26 % at a cutoff of  $0.01 \text{ mW/m}^2$  to 41 % above  $0.1 \text{ mW/m}^2$ .

1454 **8.4 Events by Frequency**

1455 The difference in magnetospheric conditions between the dayside and the nightside  
1456 suggest that different eigenfrequencies should arise between dayside and nightside res-  
1457 onances at the same  $L$ -shell. In fact, this phenomenon has been observed directly;  
1458 the frequencies of azimuthally-drifting FLRs have been shown to change over time[68].

1459 The effect is attributed to the difference in mass loading (and thus Alfvén speed) as a  
1460 function of MLT.

1461 This effect was furthermore apparent in the numerical results shown in Chapter 7, where  
1462 Alfvén speeds on the dayside (based on empirical profiles) gave rise to significantly higher  
1463 eigenfrequencies than those on the nightside.

1464 In Figure 8.7, events at 11 mHz to 17 mHz (center column) do seem to be shifted night-  
1465 ward compared to those at 7 mHz to 11 mHz (left column), but the effect is far less  
1466 pronounced than what is suggested by Sections 7.2 and 7.3.

1467 As might be expected, even events are more prevalent than (mostly fundamental) odd  
1468 events higher in the Pc4 range. Events at 7 mHz to 11 mHz (left column) outnumber  
1469 those at 17 mHz to 25 mHz (right column) ten-to-one or more for odd events. Among  
1470 even events, the comparison is more like three-to-one.

1471 The spatial distribution of odd toroidal events above 17 mHz warrants specific consid-  
1472 eration. Whereas odd toroidal events overall show an overwhelming preference for the  
1473 morning side, those at the top of the Pc4 frequency band instead appear from noon  
1474 to dusk. It's possible that this distribution is a consequence of the small number of  
1475 events (25). More likely, however, is that these are third-harmonic events, and that  
1476 their source more closely resembles the source for second-harmonic waves than it does  
1477 first harmonics.

1478 The frequency distribution for each mode is shown in Figure 8.8. The most distinctive  
1479 feature, certainly, is the frequency peak in the odd toroidal mode near 9 mHz. This is  
1480 in line with the idea that toroidal waves exhibit frequencies that depend sharply on  $L$ ,  
1481 as discussed in Chapter 7. While the Van Allen Probes' orbits do cover a large range of

<sup>1482</sup>  $L$ -shells, their observations (and thus the selected events) are concentrated near apogee  
<sup>1483</sup> at  $L \sim 6$ .

### Distribution of Pc4 Events by Mode and Frequency

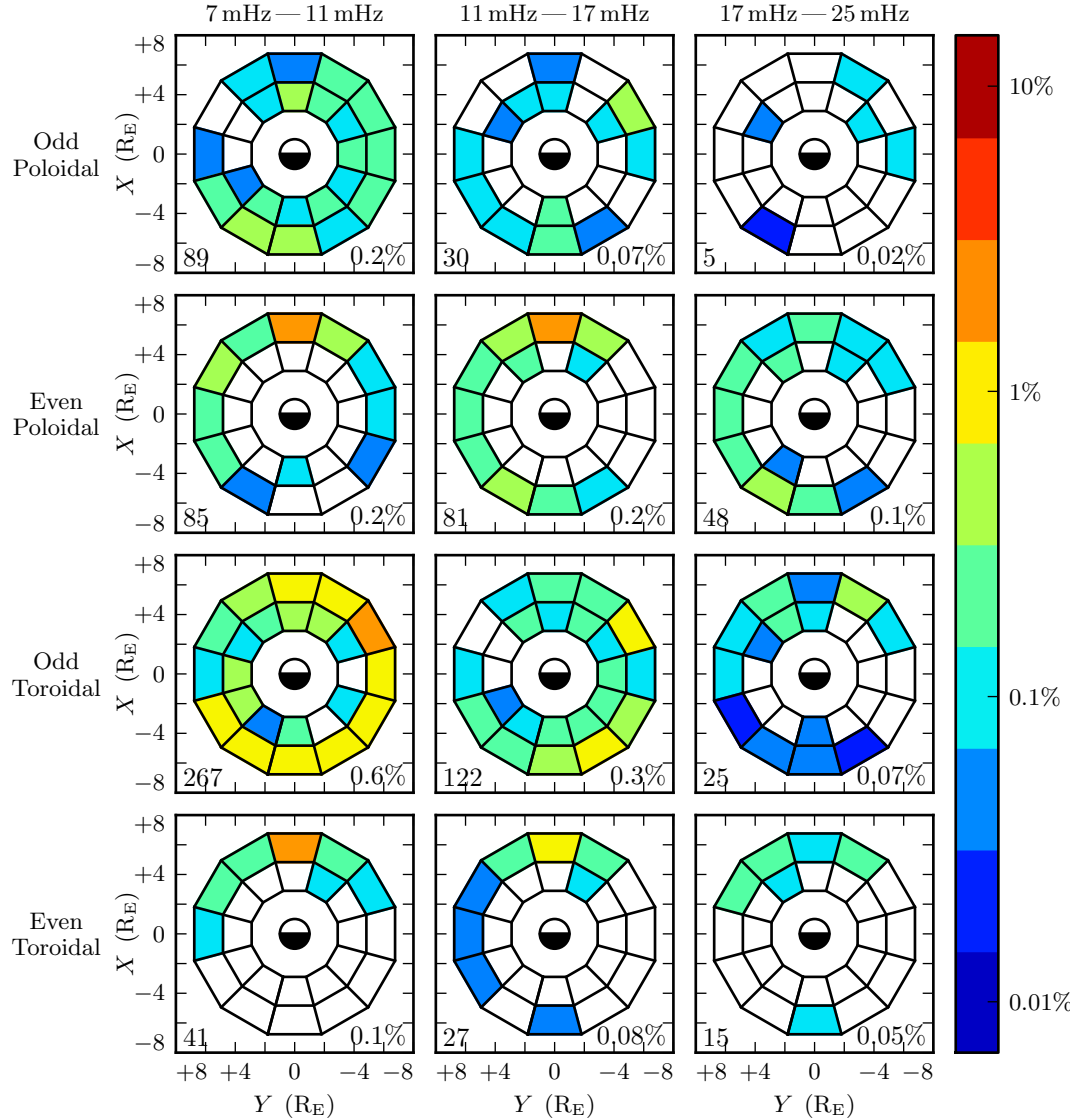


Figure 8.7: Event distributions above are shown in terms of mode (row) as well as event frequency (column). Mid-frequency Pc4 events are shifted somewhat nightward compared to low-frequency Pc4 events, as might be expected from the dayside's faster Alfvén speed. At the top of the Pc4 band, the distribution of odd toroidal events takes on a decidedly different character; this is likely because these events are third harmonics rather than first harmonics.

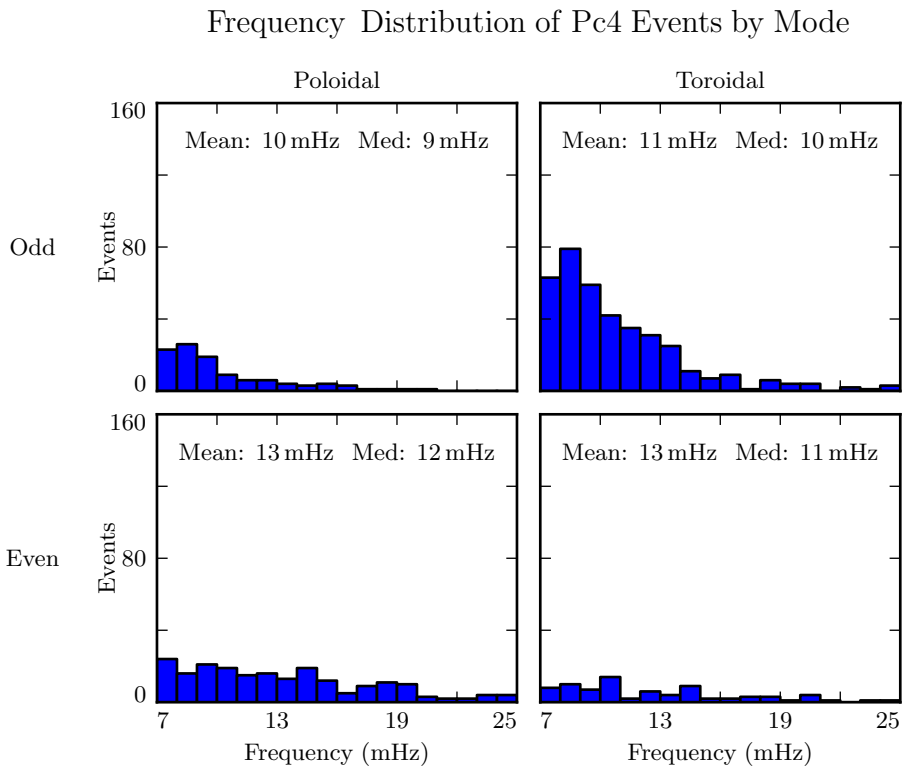


Figure 8.8: Frequency distributions are shown for all events, divided by harmonic and polarization. Odd toroidal events exhibit a particularly sharp peak in frequency, which is consistent with the toroidal mode's strong correlation with the local eigenfrequency. Poloidal modes appear more spread out in frequency, which is also consistent with past observations and with the numerical results in Chapter 7.

1484 **8.5 Events by Phase**

1485 The phase of a wave — that is, the phase offset between a wave's electric and magnetic  
1486 fields — indicates how its energy is partitioned between the standing and traveling  
1487 wave modes. An ideal standing wave has a phase of  $\pm 90^\circ$ , and thus its Poynting flux is  
1488 completely imaginary. A traveling wave, on the other hand, has electric and magnetic  
1489 fields in phase (or in antiphase), and is associated with a net movement of energy,  
1490 usually toward the ionosphere.

1491 Wave phase is a topic of significant interest, since it allows an estimate to be made of  
1492 the wave's lifetime. And, because phase can only be determined using simultaneous  
1493 electric and magnetic field measurements, it has only recently become observable.

The energy per unit volume, and the rate at which energy is carried out of that volume by Poynting flux, are respectively given by:

$$U = \frac{R^3}{2\mu_0} B^2 \quad \frac{\partial}{\partial t} U = \frac{R^2}{\mu_0} EB \cos \varphi \quad (8.2)$$

1494 Where  $B$ ,  $E$ , and  $R$  are the characteristic magnetic field magnitude, electric field mag-  
1495 nitude, and length scale. The phase,  $\varphi \equiv \arctan \frac{\text{Im} \tilde{S}}{\text{Re} \tilde{S}}$ , enters because only real Poynting  
1496 flux carries energy.

The ratio of the two quantities in Equation (8.2) gives a characteristic timescale over which energy leaves the system

$$\tau \equiv \frac{BR}{2E \cos \varphi} \quad (8.3)$$

1497 In the present case, magnetic fields are on the order of 1 nT and electric fields are on  
1498 the order of 1 mV/m. A reasonable scale length might be  $10^4$  km, the distance traversed  
1499 by the probe over the course of a half-hour event near apogee (notably, back-to-back  
1500 events are unusual).

1501 At a phase of  $80^\circ$ , this timescale is comparable to a Pc4 wave period. At  $135^\circ$ , where  
1502 energy is divided evenly between the standing and traveling wave, the timescale is just

1503 7 seconds. A wave with a phase so far from  $90^\circ$  would quickly vanish unless it were  
1504 constantly being replenished.

1505 An example of just such an event is shown in Figure 8.9. The left column shows  
1506 electric and magnetic field waveforms in blue and red respectively. The right shows  
1507 the corresponding spectra: imaginary Poynting flux in magenta (corresponding to the  
1508 strength of the standing wave) and real Poynting flux in green (for the traveling wave).  
1509 The black line is a Gaussian fit to the magnitude of the Poynting flux.

1510 The poloidal channel shows a mostly-standing wave, with a phase of  $79^\circ$ . The coherent  
1511 activity in the compressional magnetic field implies a low azimuthal modenumber, and  
1512 thus a fast rotation of energy from the poloidal mode to the toroidal mode. It's likely  
1513 the rotation of energy from the poloidal mode contributes significantly to the toroidal  
1514 mode's lifetime; the toroidal wave's phase is  $130^\circ$ , so its energy should be carried away  
1515 quickly by Poynting flux.

1516 The selection process described in Section 8.1 does not explicitly consider phase. How-  
1517 ever, the discrete Fourier transform is performed over a half-hour time span. An event  
1518 with a comparatively short lifetime would be unlikely to register. It's unsurprising to  
1519 see the events in Figure 8.10 are tightly clustered near  $90^\circ$ .

1520 It's further notable in Figure 8.10 that the odd events are more spread out in phase  
1521 than the even events. Near the equator, odd modes have an electric field antinode and  
1522 a magnetic field node; per Equation (8.3), an odd mode's lifetime should be longer than  
1523 that of an even mode with the same phase.

1524 Unlike amplitude (Section 8.3) and frequency (Section 8.4), events of different phase do  
1525 not seem to exhibit different spatial distributions, as shown in Figure 8.11. Comparisons  
1526 are limited by the small event counts in several of the subplots; however, coarsely  
1527 speaking, events with phases of  $75^\circ$  and worse (left column) show spatial distributions  
1528 more or less in proportion with events phased  $85^\circ$  or better (right column). Figure 8.10  
1529 uses the absolute value of each event's phase, as does Figure 8.11.

### Waveforms and Spectra: Odd Poloidal Wave and Odd Toroidal Wave

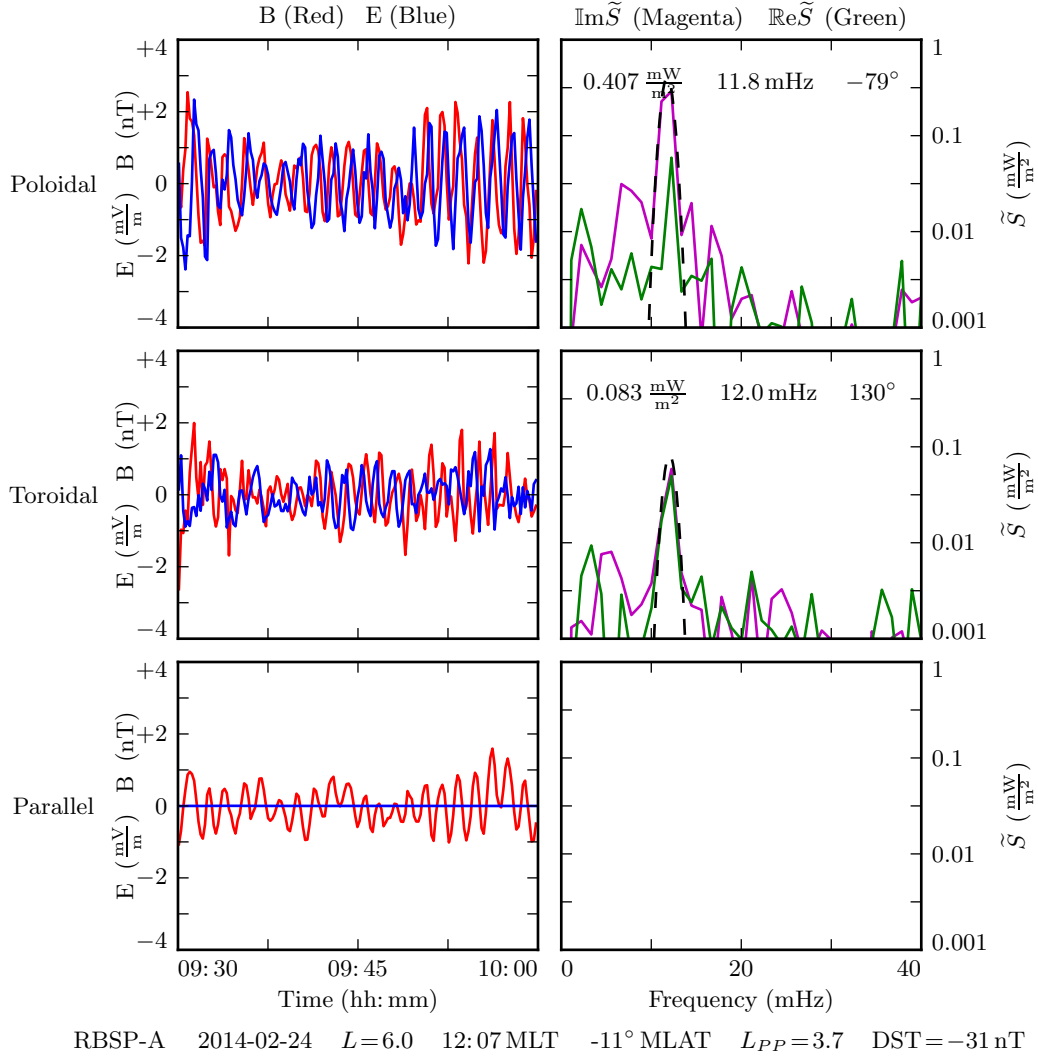


Figure 8.9: The above is a double event, where the poloidal and toroidal channels have been independently selected as events. The poloidal channel shows a wave with most of its energy in the standing wave (phase of  $79^\circ$ ). The toroidal mode has a significant traveling component (phase of  $130^\circ$ ). The compressional activity implies a low modenumber, which would cause energy to rotate quickly from the poloidal mode to the toroidal mode — evidently at a sufficient rate to replenish the losses due to the traveling mode's real Poynting flux.

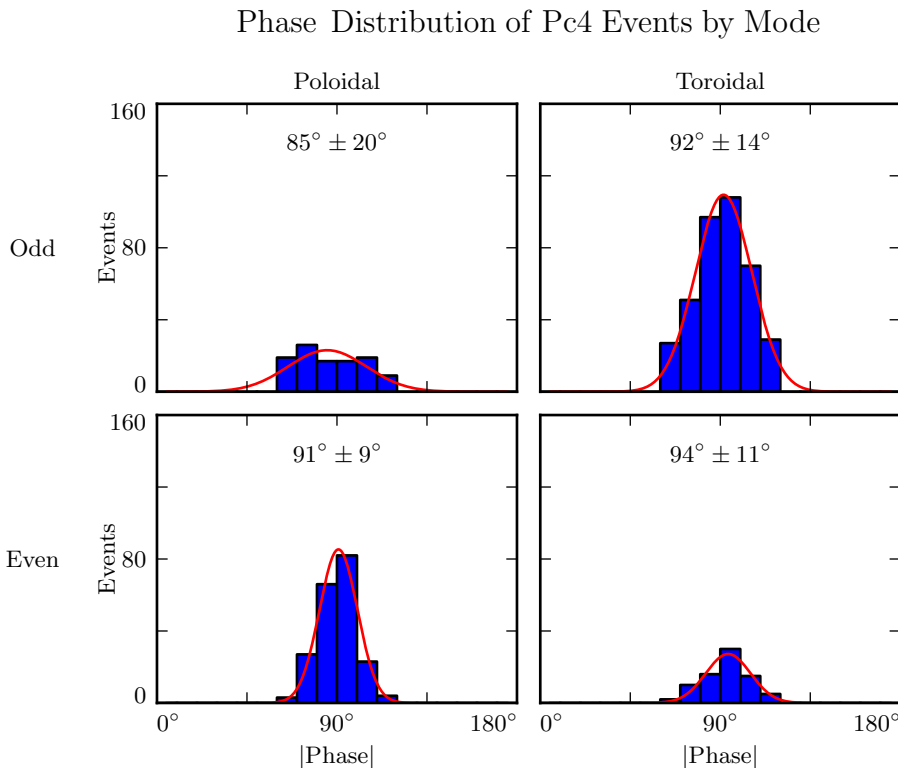


Figure 8.10: The (absolute) phase of the selected Pc4 events is shown above. All modes show phase distributions peaked around  $90^\circ$ . This reflects the fact that a significant traveling wave component quickly carries energy away from an FLR. Odd events are spread more broadly in phase than even events. This is consistent with the odd modes' electric field antinode near the equator, where events are observed; the characteristic loss timescale depends on  $\frac{B}{E}$  per Equation (8.3).

### Distribution of Pc4 Events by Mode and Phase

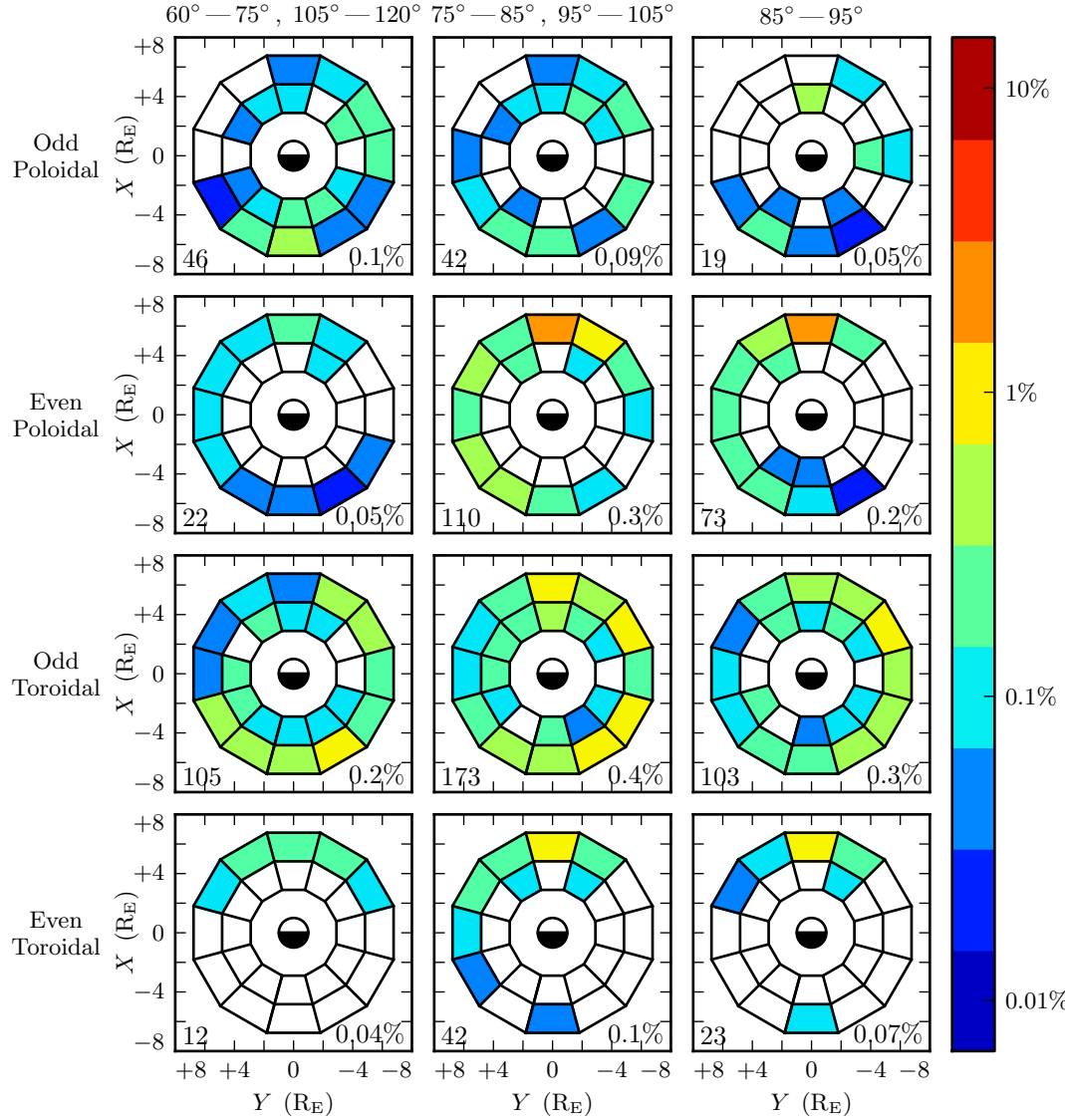


Figure 8.11: The observation rate of events is shown above, divided by (absolute) phase as well as mode. The closer a phase to  $90^\circ$ , the more of an event's energy is in the standing wave, rather than the traveling wave. The spatial distribution of events is more or less consistent between waves with phases very close to  $90^\circ$  and those with a significant traveling wave component.

1530 **8.6 Discussion**

1531 The present chapter gives a survey of  $\sim 800$  thirty-minute Pc4 events, each characterized  
1532 in terms of both parity and polarization, and selected in a way that does not introduce  
1533 an apparent bias in either property. No past study has so thoroughly disentangled the  
1534 parity and polarization of these waves.

1535 Coarsely speaking, event distributions are found to be consistent with past surveys.  
1536 Toroidal events dominate overall, and are primarily seen on the morning side. Poloidal  
1537 events are spread broadly in MLT, with a peak near noon and distinctive odd harmonics  
1538 in the early morning. From there, the simultaneous consideration of harmonic and  
1539 polarization, combined with the numerical results from Chapter 7, offers significant  
1540 insight.

1541 The near-noon peak of poloidal Pc4 events is shown to be due to even events (a majority  
1542 subset). Odd poloidal events occur preferentially near midnight and across the morning  
1543 side. Similarly, toroidal events are mostly odd, and it is specifically the odd toroidal  
1544 events which occur on the morningside, while even toroidal events peak near noon.

1545 The spatial distribution of even poloidal events looks much like the spatial distribution of  
1546 even toroidal events, except that the toroidal distribution is skewed dayward compared  
1547 to the poloidal. The same can be said of the odd events. This is consistent (per  
1548 Chapter 7) with poloidal events as an effective source for (same-parity) toroidal events  
1549 on the dayside, and a less-effective source on the nightside.

1550 Curiously, only a small minority (17 %) of toroidal events are found to be odd, while a  
1551 majority (63 %) of poloidal events are even. This disparity may offer clues to the source  
1552 of these waves.

1553 All events are found to follow a similar amplitude distribution, except for even poloidal  
1554 events, which are notably larger. The cause is unclear.

1555 The  $\sim 6\%$  of odd toroidal Pc4s at the top of the frequency range (17 mHz to 25 mHz)  
1556 are found to exhibit a qualitatively different spatial distribution from the rest. It's likely  
1557 that these waves are third harmonics, and that their excitation mechanism more closely  
1558 resembles that of second harmonics than it does first harmonics.

1559 Event phase is also considered. Most events of both polarizations are shown to have  
1560 absolute phase in the range  $80^\circ$  to  $100^\circ$ , indicating that the traveling component of  
1561  $\text{Pc}4$  pulsations is small compared to the standing component. Odd events are found to  
1562 be spread more broadly in phase; this is likely a consequence of being measured near  
1563 the equator, where (due to the electric field antinode) the lifetime of an odd event is  
1564 significantly larger than that of an even event with the same phase.

1565 **Chapter 9**

1566 **Conclusion**

1567 **TODO:** ...

1568 **9.1 Code Development**

1569 **9.2 Numerical Work**

1570 **9.3 Van Allen Probe Pc4 Survey**

# <sup>1571</sup> References

- <sup>1572</sup> [1] H. Alfvén. On the cosmogony of the solar system III. *Stockholms Observatoriums Annaler*, 14:9.1–9.29, 1946.
- <sup>1573</sup>
- <sup>1574</sup> [2] B. J. Anderson, M. J. Engebretson, S. P. Rounds, L. J. Zanetti, and T. A. Potemra. A statistical study of Pc 3-5 pulsations observed by the AMPTE/CCE magnetic fields experiment, 1. occurrence distributions. *J. Geophys. Res.*, 95(A7):10495, 1990.
- <sup>1575</sup>
- <sup>1576</sup>
- <sup>1577</sup>
- <sup>1578</sup> [3] V. Angelopoulos. The THEMIS mission. *Space Science Reviews*, 141(1-4):5–34, 2008.
- <sup>1579</sup>
- <sup>1580</sup> [4] C. W. Arthur and R. L. McPherron. The statistical character of Pc 4 magnetic pulsations at synchronous orbit. *J. Geophys. Res.*, 86(A3):1325, 1981.
- <sup>1581</sup>
- <sup>1582</sup> [5] K. Birkeland. Expédition norvégienne de 1899-1900 pour l'étude des aurores boréales. *Mat. Naturvidensk. Kl.*, KI(I), 1901.
- <sup>1583</sup>
- <sup>1584</sup> [6] J. P. Boris. A physically motivated solution of the Alfvén problem. *NRL Memorandum Report*, 2167, 1970.
- <sup>1585</sup>
- <sup>1586</sup> [7] A. Brekke, T. Feder, and S. Berger. Pc4 giant pulsations recorded in Tromsø, 1929-1985. *Journal of Atmospheric and Terrestrial Physics*, 49(10):1027–1032, 1987.
- <sup>1587</sup>
- <sup>1588</sup>
- <sup>1589</sup> [8] C. W. Carlson, R. F. Pfaff, and J. G. Watzin. The fast auroral Snapshot (FAST) mission. *Geophys. Res. Lett.*, 25(12):2013–2016, 1998.
- <sup>1590</sup>

- 1591 [9] A. A. Chan, M. Xia, and L. Chen. Anisotropic alfvén-balloon modes in Earth's  
1592 magnetosphere. *J. Geophys. Res. Space Physics*, 99(A9):17351–17366, 1994.
- 1593 [10] L. Chen and A. Hasegawa. A theory of long-period magnetic pulsations: 1. steady  
1594 state excitation of field line resonance. *J. Geophys. Res.*, 79(7):1024–1032, 1974.
- 1595 [11] L. Chen and A. Hasegawa. Kinetic theory of geomagnetic pulsations: 1. internal  
1596 excitations by energetic particles. *J. Geophys. Res.*, 96(A2):1503, 1991.
- 1597 [12] C. Z. Cheng and Q. Qian. Theory of ballooning-mirror instabilities for anisotropic  
1598 pressure plasmas in the magnetosphere. *J. Geophys. Res.*, 99(A6):11193, 1994.
- 1599 [13] G. Chisham and D. Orr. Statistical studies of giant pulsations (pgs): Harmonic  
1600 mode. *Planetary and Space Science*, 39(7):999–1006, 1991.
- 1601 [14] W. D. Cummings, R. J. O'Sullivan, and P. J. Coleman. Standing Alfvén waves in  
1602 the magnetosphere. *J. Geophys. Res.*, 74(3):778–793, 1969.
- 1603 [15] L. Dai. Collisionless magnetic reconnection via Alfvén eigenmodes. *Phys. Rev.*  
1604 *Lett.*, 102(24), 2009.
- 1605 [16] L. Dai, K. Takahashi, R. Lysak, C. Wang, J. R. Wygant, C. Kletzing, J. Bonnell,  
1606 C. A. Cattell, C. W. Smith, R. J. MacDowall, S. Thaller, A. Breneman, X. Tang,  
1607 X. Tao, and L. Chen. Storm time occurrence and spatial distribution of Pc4  
1608 poloidal ULF waves in the inner magnetosphere: A Van Allen Probes statistical  
1609 study. *J. Geophys. Res. Space Physics*, 120:4748–4762, 2015.
- 1610 [17] L. Dai, K. Takahashi, J. R. Wygant, L. Chen, J. Bonnell, C. A. Cattell, S. Thaller,  
1611 C. Kletzing, C. W. Smith, R. J. MacDowall, D. N. Baker, J. B. Blake, J. Fennell,  
1612 S. Claudepierre, H. O. Funsten, G. D. Reeves, and H. E. Spence. Excitation of  
1613 poloidal standing Alfvén waves through drift resonance wave-particle interaction.  
1614 *Geophys. Res. Lett.*, 40:4127–4132, 2013.
- 1615 [18] A. W. Degeling, R. Rankin, and Q.-G. Zong. Modeling radiation belt electron  
1616 acceleration by ULF fast mode waves, launched by solar wind dynamic pressure  
1617 fluctuations. *J. Geophys. Res. Space Physics*, 119(11):8916–8928, 2014.

- 1618 [19] W. D. D'haeseleer, W. N. G. H. J. D. Callen, and J. L. Shohet. *Flux Coordinates*  
1619 *and Magnetic Field Structure*. Springer-Verlag, New York, 1991.
- 1620 [20] J. W. Dungey. The attenuation of Alfvén waves. *J. Geophys. Res.*, 59(3):323–328,  
1621 1954.
- 1622 [21] J. W. Dungey. Interplanetary magnetic field and the auroral zones. *Phys. Rev.*  
1623 *Lett.*, 6(2):47–48, 1961.
- 1624 [22] A. Einstein. Die grundlage der allgemeinen relativitätstheorie. *Ann. Phys.*,  
1625 354:769–822, 1916.
- 1626 [23] S. R. Elkington, M. K. Hudson, and A. A. Chan. Acceleration of relativistic  
1627 electrons via drift-resonant interaction with toroidal-mode Pc-5 ULF oscillations.  
1628 *Geophys. Res. Lett.*, 26(21):3273–3276, 1999.
- 1629 [24] M. J. Engebretson, D. L. Murr, K. N. Erickson, R. J. Strangeway, D. M. Klumpar,  
1630 S. A. Fuselier, L. J. Zanetti, and T. A. Potemra. The spatial extent of radial  
1631 magnetic pulsation events observed in the dayside near synchronous orbit. *J.*  
1632 *Geophys. Res.*, 97(A9):13741, 1992.
- 1633 [25] M. J. Engebretson, L. J. Zanetti, T. A. Potemra, and M. H. Acuna. Harmonically  
1634 structured ulf pulsations observed by the ampte cce magnetic field experiment.  
1635 *Geophysical Research Letters*, 13(9):905–908, 1986.
- 1636 [26] M. J. Engebretson, L. J. Zanetti, T. A. Potemra, D. M. Klumpar, R. J. Strange-  
1637 way, and M. H. Acuña. Observations of intense ULF pulsation activity near the  
1638 geomagnetic equator during quiet times. *J. Geophys. Res.*, 93(A11):12795, 1988.
- 1639 [27] S. Fujita and T. Tamao. Duct propagation of hydromagnetic waves in the upper  
1640 ionosphere, 1, electromagnetic field disturbances in high latitudes associated with  
1641 localized incidence of a shear Alfvén wave. *J. Geophys. Res.*, 93(A12):14665, 1988.
- 1642 [28] K.-H. Glassmeier. Magnetometer array observations of a giant pulsation event. *J.*  
1643 *Geophys.*, 48:127–138, 1980.
- 1644 [29] K.-H. Glassmeier. On the influence of ionospheres with non-uniform conductivity  
1645 distribution on hydromagnetic waves. *J. Geophys.*, 54(2):125–137, 1984.

- 1646 [30] K.-H. Glassmeier, S. Buchert, U. Motschmann, A. Korth, and A. Pedersen. Con-  
1647 cerning the generation of geomagnetic giant pulsations by drift-bounce resonance  
1648 ring current instabilities. *Ann. Geophysicae*, 17:338–350, 1999.
- 1649 [31] C. Goertz. Kinetic alfvén waves on auroral field lines. *Planetary and Space Science*,  
1650 32(11):1387–1392, 1984.
- 1651 [32] C. K. Goertz and R. W. Boswell. Magnetosphere-ionosphere coupling. *J. Geophys.*  
1652 *Res.*, 84(A12):7239, 1979.
- 1653 [33] J. Goldstein. Plasmasphere response: Tutorial and review of recent imaging re-  
1654 sults. *Space Science Reviews*, 124(1-4):203–216, 2006.
- 1655 [34] C. A. Green. Giant pulsations in the plasmasphere. *Planetary and Space Science*,  
1656 33(10):1155–1168, 1985.
- 1657 [35] J. L. Green and S. Boardsen. Duration and extent of the great auroral storm of  
1658 1859. *Advances in Space Research*, 38(2):130–135, 2006.
- 1659 [36] C. Greifinger and P. S. Greifinger. Theory of hydromagnetic propagation in the  
1660 ionospheric waveguide. *J. Geophys. Res.*, 73(23):7473–7490, 1968.
- 1661 [37] B. C. Hall. *Lie Groups, Lie Algebras, and Representations*. Graduate Texts in  
1662 Mathematics. Springer, New York, second edition, 2015.
- 1663 [38] Y. X. Hao, Q.-G. Zong, Y. F. Wang, X.-Z. Zhou, H. Zhang, S. Y. Fu, Z. Y.  
1664 Pu, H. E. Spence, J. B. Blake, J. Bonnell, J. R. Wygant, and C. A. Kletzing.  
1665 Interactions of energetic electrons with ULF waves triggered by interplanetary  
1666 shock: Van allen probes observations in the magnetotail. *J. Geophys. Res. Space*  
1667 *Physics*, 119(10):8262–8273, 2014.
- 1668 [39] L. Harang. *Pulsations in the terrestrial magnetic records at high latitude stations*.  
1669 Grondahl, 1942.
- 1670 [40] O. Hillebrand, J. Muench, and R. L. McPherron. Ground-satellite correlative  
1671 study of a giant pulsation event. *Journal of Geophysics Zeitschrift Geophysik*,  
1672 51:129–140, 1982.

- 1673 [41] W. J. Hughes. Magnetospheric ULF waves: A tutorial with a historical perspec-  
1674 tive. In M. J. Engebretson, K. Takahashi, and M. Scholer, editors, *Solar Wind*  
1675 *Sources of Magnetospheric Ultra-Low-Frequency Waves*, volume 81 of *Geophys.*  
1676 *Monogr.*, pages 1–12. American Geophysical Union, Washington, DC, 1994.
- 1677 [42] W. J. Hughes and D. J. Southwood. The screening of micropulsation signals by  
1678 the atmosphere and ionosphere. *J. Geophys. Res.*, 81(19):3234–3240, 1976.
- 1679 [43] W. J. Hughes, D. J. Southwood, B. Mauk, R. L. McPherron, and J. N. Barfield.  
1680 Alfvén waves generated by an inverted plasma energy distribution. *Nature*,  
1681 275(5675):43–45, 1978.
- 1682 [44] J. A. Jacobs, Y. Kato, S. Matsushita, and V. A. Troitskaya. Classification of  
1683 geomagnetic micropulsations. *J. Geophys. Res.*, 69(1):180–181, 1964.
- 1684 [45] T. Karlsson and G. T. Marklund. A statistical study of intense low-altitude electric  
1685 fields observed by freja. *Geophys. Res. Lett.*, 23(9):1005–1008, 1996.
- 1686 [46] Y. Kato and T. Tsutomu. Hydromagnetic oscillations in a conducting medium  
1687 with hall couduct-ivity under the uniform magnetic field. *Science reports of the*  
1688 *Tohoku University. Ser. 5, Geophysics*, 7(3):147–164, 1956.
- 1689 [47] M. C. Kelley. *The Earth’s Ionosphere*. Academic Press, San Diego, second edition,  
1690 1989.
- 1691 [48] R. L. Kessel. Solar wind excitation of pc5 fluctuations in the magnetosphere and  
1692 on the ground. *J. Geophys. Res.*, 113(A4), 2008.
- 1693 [49] D. Y. Klimushkin, P. N. Mager, and K.-H. Glassmeier. Toroidal and poloidal  
1694 Alfvén waves with arbitrary azimuthal wavenumbers in a finite pressure plasma  
1695 in the earth’s magnetosphere. *Annales Geophysicae*, 22(1):267–287, 2004.
- 1696 [50] S. Knight. Parallel electric fields. *Planetary and Space Science*, 21:741–750, 1973.
- 1697 [51] S. Kokubun. Observations of Pc pulsations in the magnetosphere: Satellite-ground  
1698 correlation. *J. Geomagn. Geoelec*, 32(Supplement2):SII17–SII39, 1980.

- 1699 [52] S. Kokubun, K. N. Erickson, T. A. Fritz, and R. L. McPherron. Local time asymmetry of Pc 4-5 pulsations and associated particle modulations at synchronous  
1700 orbit. *J. Geophys. Res.*, 94(A6):6607–6625, 1989.
- 1701
- 1702 [53] D.-H. Lee and K. Kim. Compressional MHD waves in the magnetosphere: A new  
1703 approach. *J. Geophys. Res.*, 104(A6):12379–12385, 1999.
- 1704 [54] A. S. Leonovich and V. A. Mazur. Structure of magnetosonic eigenoscillations of  
1705 an axisymmetric magnetosphere. *J. Geophys. Res.*, 105(A12):27707–27715, 2000.
- 1706 [55] W. Liu, J. B. Cao, X. Li, T. E. Sarris, Q.-G. Zong, M. Hartinger, K. Takahashi,  
1707 H. Zhang, Q. Q. Shi, and V. Angelopoulos. Poloidal ULF wave observed in the  
1708 plasmasphere boundary layer. *J. Geophys. Res. Space Physics*, 118(7):4298–4307,  
1709 2013.
- 1710 [56] W. Liu, T. E. Sarris, X. Li, S. R. Elkington, R. Ergun, V. Angelopoulos, J. Bonnell,  
1711 and K. H. Glassmeier. Electric and magnetic field observations of Pc4 and Pc5  
1712 pulsations in the inner magnetosphere: A statistical study. *J. Geophys. Res.*,  
1713 114(A12), 2009.
- 1714 [57] W. Liu, T. E. Sarris, X. Li, Q.-G. Zong, R. Ergun, V. Angelopoulos, and K. H.  
1715 Glassmeier. Spatial structure and temporal evolution of a dayside poloidal ULF  
1716 wave event. *Geophys. Res. Lett.*, 38(19), 2011.
- 1717 [58] R. L. Lysak. Magnetosphere-ionosphere coupling by Alfvén waves at midlatitudes.  
1718 *J. Geophys. Res.*, 109, 2004.
- 1719 [59] R. L. Lysak and D. hun Lee. Response of the dipole magnetosphere to pressure  
1720 pulses. *Geophys. Res. Lett.*, 19(9):937–940, 1992.
- 1721 [60] R. L. Lysak and Y. Song. A three-dimensional model of the propagation of Alfvén  
1722 waves through the auroral ionosphere: first results. *Adv. Space Res.*, 28:813–822,  
1723 2001.
- 1724 [61] R. L. Lysak, C. L. Waters, and M. D. Sciffer. Modeling of the ionospheric Alfvén  
1725 resonator in dipolar geometry. *J. Geophys. Res. Space Physics*, 118, 2013.

- 1726 [62] P. N. Mager and D. Y. Klimushkin. Giant pulsations as modes of a transverse  
1727 Alfvénic resonator on the plasmapause. *Earth, Planets and Space*, 65(5):397–409,  
1728 2013.
- 1729 [63] I. R. Mann, E. A. Lee, S. G. Claudepierre, J. F. Fennell, A. Degeling, I. J. Rae,  
1730 D. N. Baker, G. D. Reeves, H. E. Spence, L. G. Ozeke, R. Rankin, D. K. Milling,  
1731 A. Kale, R. H. W. Friedel, and F. Honary. Discovery of the action of a geophysical  
1732 synchrotron in the Earth’s Van Allen radiation belts. *Nature Communications*, 4,  
1733 2013.
- 1734 [64] I. R. Mann and A. N. Wright. Finite lifetimes of ideal poloidal Alfvén waves. *J.  
1735 Geophys. Res.*, 100:23677–23686, 1995.
- 1736 [65] I. R. Mann, A. N. Wright, and A. W. Hood. Multiple-timescales analysis of ideal  
1737 poloidal Alfvén waves. *J. Geophys. Res.*, 102(A2):2381–2390, 1997.
- 1738 [66] T. Maynard, N. Smith, S. Gonzalez, et al. Solar storm risk to the North American  
1739 electric grid. 2013.
- 1740 [67] R. L. McPherron. The role of substorms in the generation of magnetic storms.  
1741 *Washington DC American Geophysical Union Geophysical Monograph Series*,  
1742 98:131–147, 1997.
- 1743 [68] T. Motoba, K. Takahashi, J. V. Rodriguez, and C. T. Russell. Giant pulsations on  
1744 the afternoonside: Geostationary satellite and ground observations. *J. Geophys.  
1745 Res. Space Physics*, 120:8350–8367, 2015.
- 1746 [69] NASA. Coordinated data analysis (workshop) web.
- 1747 [70] NASA. Near miss: The solar superstorm of july 2012.
- 1748 [71] M. Nicolet. The collision frequency of electrons in the ionosphere. *Journal of  
1749 Atmospheric and Terrestrial Physics*, 3(4):200–211, 1953.
- 1750 [72] L. G. Ozeke and I. R. Mann. Energization of radiation belt electrons by ring  
1751 current ion driven ULF waves. *J. Geophys. Res.*, 113(A2), 2008.
- 1752 [73] E. M. Poulter, W. Allan, E. Nielsen, and K.-H. Glassmeier. Stare radar observa-  
1753 tions of a PG pulsation. *J. Geophys. Res.*, 88(A7):5668, 1983.

- 1754 [74] J. A. Proehl, W. Lotko, I. Kouznetsov, and S. D. Geimer. Ultralow-frequency  
1755 magnetohydrodynamics in boundary-constrained geomagnetic flux coordinates.  
1756 *J. Geophys. Res.*, 107(A9):1225, 2002.
- 1757 [75] H. R. Radoski. A note on oscillating field lines. *J. Geophys. Res.*, 72(1), 1967.
- 1758 [76] H. R. Radoski. A theory of latitude dependent geomagnetic micropulsations: The  
1759 asymptotic fields. *J. Geophys. Res.*, 79, 1974.
- 1760 [77] R. Rankin, J. C. Samson, and V. T. Tikhonchuk. Parallel electric fields in dis-  
1761 persive shear alfvén waves in the dipolar magnetosphere. *Geophys. Res. Lett.*,  
1762 26(24):3601–3604, 1999.
- 1763 [78] B. Rolf. Giant micropulsations at abisko. *J. Geophys. Res.*, 36(1):9, 1931.
- 1764 [79] G. Rostoker, H.-L. Lam, and J. V. Olson. PC 4 giant pulsations in the morning  
1765 sector. *J. Geophys. Res.*, 84(A9):5153, 1979.
- 1766 [80] J. C. Samson, L. L. Cogger, and Q. Pao. Observations of field line resonances,  
1767 auroral arcs, and auroral vortex structures. *J. Geophys. Res.*, 101(A8):17373–  
1768 17383, 1996.
- 1769 [81] H. J. Singer, W. J. Hughes, and C. T. Russell. Standing hydromagnetic waves  
1770 observed by ISEE 1 and 2: Radial extent and harmonic. *J. Geophys. Res.*,  
1771 87(A5):3519, 1982.
- 1772 [82] D. J. Southwood. Some features of field line resonances in the magnetosphere.  
1773 *Planetary and Space Science*, 22(3):483–491, 1974.
- 1774 [83] D. J. Southwood. A general approach to low-frequency instability in the ring  
1775 current plasma. *J. Geophys. Res.*, 81(19):3340–3348, 1976.
- 1776 [84] J. Stratton and N. J. Fox. Radiation belt storm probes (RBSP) mission overview.  
1777 In *2012 IEEE Aerospace Conference*. Institute of Electrical & Electronics Engi-  
1778 neers (IEEE), 2012.
- 1779 [85] E. Sucksdorff. Giant pulsations recorded at sodankyl during 19141938. *Terrestrial  
1780 Magnetism and Atmospheric Electricity*, 44(2):157–170, 1939.

- 1781 [86] K. Takahashi, J. Bonnell, K.-H. Glassmeier, V. Angelopoulos, H. J. Singer, P. J.  
1782 Chi, R. E. Denton, Y. Nishimura, D.-H. Lee, M. Nosé, and W. Liu. Multipoint  
1783 observation of fast mode waves trapped in the dayside plasmasphere. *J. Geophys.*  
1784 *Res.*, 115(A12), 2010.
- 1785 [87] K. Takahashi, K.-H. Glassmeier, V. Angelopoulos, J. Bonnell, Y. Nishimura, H. J.  
1786 Singer, and C. T. Russell. Multisatellite observations of a giant pulsation event.  
1787 *J. Geophys. Res.*, 116:A11223, 2011.
- 1788 [88] K. Takahashi, M. D. Hartinger, V. Angelopoulos, K.-H. Glassmeier, and H. J.  
1789 Singer. Multispacecraft observations of fundamental poloidal waves without  
1790 ground magnetic signatures. *J. Geophys. Res. Space Physics*, 118:4319–4334, 2013.
- 1791 [89] K. Takahashi, R. W. McEntire, A. T. Y. Lui, and T. A. Potemra. Ion flux oscillations  
1792 associated with a radially polarized transverse Pc 5 magnetic pulsation. *J.*  
1793 *Geophys. Res.*, 95(A4):3717, 1990.
- 1794 [90] K. Takahashi and R. L. McPherron. Standing hydromagnetic oscillations in the  
1795 magnetosphere. *Planetary and Space Science*, 32:1343–1359, 1984.
- 1796 [91] K. Takahashi, N. Sato, J. Warnecke, H. Lühr, H. E. Spence, and Y. Tonegawa.  
1797 On the standing wave mode of giant pulsations. *J. Geophys. Res. Space Physics*,  
1798 97(A7):10717–10732, 1992.
- 1799 [92] B. J. Thompson and R. L. Lysak. Electron acceleration by inertial alfvén waves.  
1800 *J. Geophys. Res.*, 101(A3):5359–5369, 1996.
- 1801 [93] V. T. Tikhonchuk and R. Rankin. Electron kinetic effects in standing shear alfvén  
1802 waves in the dipolar magnetosphere. *Physics of Plasmas*, 7(6):2630, 2000.
- 1803 [94] B. T. Tsurutani, W. D. Gonzalez, G. S. Lakhina, and S. Alex. The extreme  
1804 magnetic storm of 12 september 1859. *Journal of Geophysical Research: Space*  
1805 *Physics*, 108(A7), 2003. 1268.
- 1806 [95] A. Y. Ukhorskiy. Impact of toroidal ULF waves on the outer radiation belt elec-  
1807 trons. *J. Geophys. Res.*, 110(A10), 2005.

- 1808 [96] J. A. Wanliss and K. M. Showalter. High-resolution global storm index: Dst versus  
1809 sym-h. *Journal of Geophysical Research: Space Physics*, 111(A2):n/a–n/a, 2006.  
1810 A02202.
- 1811 [97] C. L. Waters, R. L. Lysak, and M. D. Sciffer. On the coupling of fast and shear  
1812 Alfvén wave modes by the ionospheric Hall conductance. *Earth Planets Space*,  
1813 65:385–396, 2013.
- 1814 [98] C. L. Waters and M. D. Sciffer. Field line resonant frequencies and ionospheric  
1815 conductance: Results from a 2-d MHD model. *J. Geophys. Res.*, 113(A5), 2008.
- 1816 [99] D. M. Wright and T. K. Yeoman. High-latitude HF doppler observations of ULF  
1817 waves: 2. waves with small spatial scale sizes. *Ann. Geophys.*, 17(7):868–876,  
1818 1999.
- 1819 [100] J. R. Wygant, J. W. Bonnell, K. Goetz, R. E. Ergun, F. S. Mozer, S. D. Bale,  
1820 M. Ludlam, P. Turin, P. R. Harvey, R. Hochmann, K. Harps, G. Dalton, J. Mc-  
1821 Cauley, W. Rachelson, D. Gordon, B. Donakowski, C. Shultz, C. Smith, M. Diaz-  
1822 Aguado, J. Fischer, S. Heavner, P. Berg, D. M. Malsapina, M. K. Bolton, M. Hud-  
1823 son, R. J. Strangeway, D. N. Baker, X. Li, J. Albert, J. C. Foster, C. C. Chaston,  
1824 I. Mann, E. Donovan, C. M. Cully, C. A. Cattell, V. Krasnoselskikh, K. Kersten,  
1825 A. Brenneman, and J. B. Tao. The electric field and waves instruments on the  
1826 radiation belt storm probes mission. *Space Science Reviews*, 179(1):183–220, 2013.
- 1827 [101] J. R. Wygant, A. Keiling, C. A. Cattell, R. L. Lysak, M. Temerin, F. S. Mozer,  
1828 C. A. Kletzing, J. D. Scudder, V. Streltsov, W. Lotko, and C. T. Russell. Evidence  
1829 for kinetic alfvn waves and parallel electron energization at 46 re altitudes in the  
1830 plasma sheet boundary layer. *Journal of Geophysical Research: Space Physics*,  
1831 107(A8):SMP 24–1–SMP 24–15, 2002.
- 1832 [102] K. Yee. Numerical solution of initial boundary value problems involving maxwell's  
1833 equations in isotropic media. *IEEE Trans. Antennas Propagat.*, 14(3), 1966.
- 1834 [103] T. K. Yeoman and D. M. Wright. ULF waves with drift resonance and drift-bounce  
1835 resonance energy sources as observed in artificially-induced HF radar backscatter.  
1836 *Ann. Geophys.*, 19(2):159–170, 2001.

- 1837 [104] Q.-G. Zong, X.-Z. Zhou, X. Li, P. Song, S. Y. Fu, D. N. Baker, Z. Y. Pu, T. A.  
1838 Fritz, P. Daly, A. Balogh, and H. Réme. Ultralow frequency modulation of ener-  
1839 getic particles in the dayside magnetosphere. *Geophys. Res. Lett.*, 34(12), 2007.
- 1840 [105] Q.-G. Zong, X.-Z. Zhou, Y. F. Wang, X. Li, P. Song, D. N. Baker, T. A. Fritz,  
1841 P. W. Daly, M. Dunlop, and A. Pedersen. Energetic electron response to ULF  
1842 waves induced by interplanetary shocks in the outer radiation belt. *J. Geophys.  
1843 Res.*, 114(A10), 2009.